Stimuli-responsive polymer brushes for on-chip cell adhesion control

Siddhartha Varma

Communauté
UNIVERSITÉ Grenoble Alpes

THÈSE

Pour obtenir le grade de

DOCTEUR DE LA COMMUNAUTÉ UNIVERSITÉ GRENOBLE ALPES

Spécialité : **Physique pour le vivant**

Arrêté ministériel : 7 août 2006

Présentée par

Siddhartha VARMA

Thèse dirigée par **Lionel BUREAU** et
codirigée par **Delphine DEBARRE**

préparée au sein du **Laboratoire Interdisciplinaire de Physique**
dans **l'École Doctorale de Physique**

Brosses de polymères stimuli-sensibles pour le contrôle de l'adhésion cellulaire

Thèse soutenue publiquement le **10 octobre 2016**,
devant le jury composé de :

Mme Elisabeth CHARLAIX
Professeur Université Grenoble Alpes, LIPhy Grenoble, présidente
Mme Marie-Pierre VALIGNAT
Maître de conférence Université Aix-Marseille, LAI Marseille, rapporteur
M Jean DAILLANT
Directeur général Synchrotron Soleil, Gif-sur-Yvette, rapporteur
M Thierry CHARITAT
Professeur Université de Strasbourg, ICS, examinateur
M Laurent HEUX
Directeur de recherche CNRS, CERMAV Grenoble, examinateur

"If you want to shine like a sun, first burn like a sun" - A.P.J abdul Kalam

Chapter 1

Acknowledgements

First and foremost, I would like to express my deepest gratitude to my supervisors Dr. Lionel Bureau and Dr. Delphine Debarre for their continuous support during my Ph.D. study. Their valuable time, constructive advice, and willingness to share their knowledge have been stimulating in all the time of my research and writing of the thesis. The enthusiasm they had for research was always mitivational for me, even during tough times during my Ph.D. I thank them for welcoming me in the lab as an intern, and providing me a chance to learn and contribute towards the development of the project. Without their precious support, it would not have been possible to conduct this research.

I would like to thank my thesis committee members starting from Dr. Marie-Pierre Valignat and Dr. Jean Daillant for evaluating my thesis and providing their insightful comments. I would like to thank the other jury members Professor Elizabeth Charlaix, Dr. Thierry Charitat, and Dr. Laurent Heux for accepting to judge my Ph.D. Thesis.

I would like to thank all the faculties at my masters level in India, as well a France for providing me with the rich scientific background. A word of special thanks goes to Professor S. Annapoorni and Professor Jean Claude Moutet for exposing me with the research opportunities in France. I would like to thank Dr. Dinesh Rangappa for constantly supporting me uptil now in my research endeavours. I will always be indebted to your valuable inputs. I would like to thank Dr Jrme Fortage and Dr. Marie-Nolle Collomb for their contribution towards the experimental characterization and analytical discussions. Thank you to Dr. Claire Boisset and her group for their help with the GPC analyses.

I thank the Agence Nationale de la Recherche (ANR) for their financial support during this work. I would like to thank the administrative department for their assistence throughout my stay at LIPhy. My time in Grenoble and LIPhy was made enjoyable in large part due to the many colleagues and friends I had. I am grateful to all my collegues for all the fun we had, for backing me up whenever I felt low, and for their love and support towards the fulfillment of my thesis. Thank you very much for your support and friendship.

Lastly, I would like to thank my family for all their love and encoragement. For my parents and grandparents who raised me with the ability to pursue what I wanted and their constant support in my life. Thank you for always believing in me. Thank you

Siddhartha Varma
Laboratoire Interdisciplinaire De Physique (LIPhy)
10^thOctober 2016.

Abstract - Résumé en français

The aim of the current Ph.D thesis was to successfully design stimuli responsive polymer brushes in order to allow dynamic cell-substrate adhesive interactions.

For this purpose, Atom Transfer Radical Polymerization (ATRP) and Activators Regenerated by electron Transfer (ARGET)-ATRP were used in order to prepare thermo responsive Poly(N-isopropylacrylamide) (PNIPAM) brushes. Both the methods were applied under varying surface densities and polymerization times, and the kinetics of the brush growth using both the protocols was investigated. A well controlled chain growth was reported under ARGET-ATRP protocol, in contrast to the ATRP method. The above tested protocol was used to grow PNIPAM brushes that were patterned via deep UV photoablation strategy to design thermoresponsive patterned substrates for protein adsorption studies. The substrates showed excellent adhesive properties and reusability with long term storage capacity.

The conformational changes of PNIPAM brushes, grown via the ARGET-ATRP protocol, were probed by an originally built set-up based on Reflection Interference Contrast Microscopy (RICM). RICM allowed to estimate the optical response of the brushes as a function of their height profile making it an interesting tool for brush characterization. The response of the brush was studied as a function of brush grafting density and chain length. The results provided a unique evidence of non-monotonic structural changes in the brushes, across the Local Critical Solution Tempearature (LCST) of the polymer. RICM was employed to achieve the challenging task of estimating the molecular parameters of the brush and understanding the physical origin of the phenomenon of thermal hysteresis in a polymer brush.

Stimuli Responsive Polymers, sensitive to non-invasive stimuli, were synthesized with an aim to address dynamic single cell adhesion studies at their physiological conditions. Free Radical Polymerization and ARGET-ATRP protocol were used to design two photo-thermo-responsive poly(DMA-AZAA) and poly(DMA-NIPAM-AZAA) polymers. The conformational changes of the designed polymers were investigated at length by varying the overall composition of monomers in the system. Both the polymers were water soluble that enabled an easy characterization. The DMA-NIPAM-AZAA terpolymer solution showed a sharp phase separation at 37°C that could be reversibly switched under light irradiation, making it compatoble for cell adhesion studies.

Le but de cette thèse de doctorat était de concevoir des brosses de polymères stimuli-sensibles afin de contrôler dynamiquement les interactions adhésives entre une cellule et son substrat.

Pour cela, nous avons utilisé la polymérisation radicalaire par transfert d'atomes

(ATRP) initiée en surface, et sa variante permettant de régénérer in situ le catalyseur de polymérisation (ARGET-ATRP), pour préparer des brosses thermo-sensibles de poly(N-isopropylacrylamide) (PNIPAM). Les deux méthodes ont été appliquées pour différentes densités surfaciques et temps de polymérisation, et les cinétiques de croissance de la brosse à l'aide des deux protocoles ont été étudiés. Une croissance de chaîne bien contrôlée a été observée avec le protocole ARGET-ATRP, mais pas avec la méthode ATRP. Le protocole testé ci-dessus a été utilisé pour fabriquer des brosses de PNIPAM qui ont été patternées par l'intermédiaire d'une stratégie d'ablation aux UV profonds, afin de concevoir des substrats permettant de contrôler spatialement l'adsorption de protéines. Ces substrats ont montré d'excellentes propriétés adhésives, sont réutilisables et peuvent se stocker sur de longues périodes.

Les changements conformationnels de brosses PNIPAM ont été sondés grâce à un dispositif original mis en place sur la base d'un microscope en réflexion à contraste d'interférences (RICM). La technique RICM a permis d'estimer la réponse optique des brosses en fonction de leur profil de hauteur, ce qui en fait un outil intéressant pour leur caractérisation. La réponse de la brosse a été étudiée en fonction de sa densité de greffage et de la longueur de chaîne. Les résultats ont fourni une preuve unique de l'existence d'un phénomène de séparation de phase verticale, donnant lieu à des changements structurels non-uniformes dans les brosses lors du passage de la température inférieure de solubilité du PNIPAM dans l'eau. Le RICM a été utilisé pour réaliser la tâche complexe d'estimer les paramètres moléculaires de la brosse et la compréhension de l'origine physique du phénomène d'hysteresis thermique dans une brosse de polymère.

De nouveaux polymères stimuli-sensibles ont été synthétisés dans le but d'obtenir des systèmes d'intérêt pour les études biologiques en conditions physiologiques. Nous avons conçus différents co-polymères photo-thermo-sensibles à base d'acrylamides et d'acrylates. Les changements de conformation des polymères conçus ont été étudiés en détail en faisant varier la composition globale des monomères dans le système. Nous avons identifié une composition de ter-polymères dont les solutions aqueuses ont montré une séparation de phase à 37 °C qui peut être réversible sous irradiation lumineuse, ce qui la rend compatible pour les études d'adhésion cellulaire.

Contents

Chapter 2

Introduction

2.1 Abstract

Cells regulate their internal organization with respect to changes in their external environment. This governs essential biological functions and is of major importance in a large number of applications. A fundamental goal in cell biology is to understand how these complex behaviours arise from the different environmental cues to which the cell is exposed. One way to unravel some of the mechanisms at play is through studying the adhesion of cells onto substrates. Controlling and understanding the cell-substrate adhesive interactions is both a fundamental and technological challenge. Striking advancements have been made in designing substrates for *in vitro* cell culturing and investigating the cell adhesion mechanisms. However, questions regarding the dynamics and robustness of cell-surface interactions remain largely open.

This chapter introduces cell adhesion phenomena and reviews strategies to control and study cell adhesion. The interactions of cells with engineered substrates provide answers to fundamental questions related to adhesion. Responsive substrates are introduced as potential tools in this context that allow immobilizing proteins and studying specific cell adsorption. Cell patterning methods impose surface restrictions to cells, thereby creating a defined cell adhesive environment. This allows to investigate the sensitivity and response of the cells to external cues. "Smart materials" are employed to design responsive substrates that exhibit tunable adhesive properties that can be altered reversibly on demand. Different types of materials, from self assembled monolayers (SAMs) to polymeric films used to design smart substrates have been discussed at length. The vast literature related to the use of such candidates for bio-interfacial studies shows tremendous potential in designing smart functional substrates to address dynamic cellular phenomenon. The material systems employed till now present limitations in terms of reversibility and spatial control of cell adhesion. This raises a set of questions that define the scope of the present thesis, focussing on the design of polymer layers allowing for spatial and temporal control of surface attachment for single cells studies.

2.2 Cells and their environment

Cells are the building units of life. They survive by maintaining, as well as regulating their internal processes in response to changes in their external environment. Cells adapt towards rapidly changing stimuli by evolving their internal biochemistry through chemical and mechanical signals. These adjustments take several forms, including changes in structure as well as functions of the cells [1]. The response of a cell is governed by its activities and actions. Errors in the ability of cells to perceive and correctly integrate the information from their micro-environment form the basis of diseases such as cancer, or diabetes.

2.2.1 Cell signalling

The changes that originate at the borders of the cells are sensed and processed by them through a unified action plan. Cell signalling calls for communication and coordination between cells and allows specialization of groups of cells to form tissues such as muscle, blood and brain tissues. Cells typically receive signals in chemical or mechanical form via various signaling molecules which have local or long range effects. Cell response is controlled by the interactions of signalling molecules and appropriate receptors which are mainly transmembrane proteins. This binding triggers the signalling pathways that help the cell in constantly adjusting to the variations occurring outside and hence maintaining a state of internal equilibrium called homeostasis.

The interactions of cells with their surrounding are evident not only in the context of physical activities such as breathing, blood flow and heart pumping, but also underly essential events such as cell migration, cell differentiation and cell survival [2]. This has led to questions regarding how individual components of the cell are able to execute such complex behaviours. Adhesion guides the transmission of responses to outside, and therefore takes part in regulating the biochemical signalling pathways.

2.2.2 Cell adhesion in biology

Cell adhesion is at the heart of complex cellular phenomena and has been a topic of immense scientific research across the globe. Cell adhesion involves the interaction of a cell with a surface, substrate or another cell. Such interactions are mediated by surface molecules of the cells and play a key role in the development and maintenance of tissues [3].

A variety of cell adhesion mechanisms are responsible for assembling cells together, onto substrates and for determining the overall architecture and proper function of tissues and organs [5, 6]. *In vivo*, tissue cells adhere to and spread on a biological matrix called the Extra Cellular Matrix (ECM), which is a meshwork composed of proteins and other biological macromolecules. The ECM, which changes its structure and composition with time, is a highly hydrated network hosting three major components: fibrous elements (e.g. collagen, elastin and reticulin), space filling molecules (glycosaminoglycans) and adhesion proteins such as fibronectin, vitronectin and laminin. The ECM provides struc-

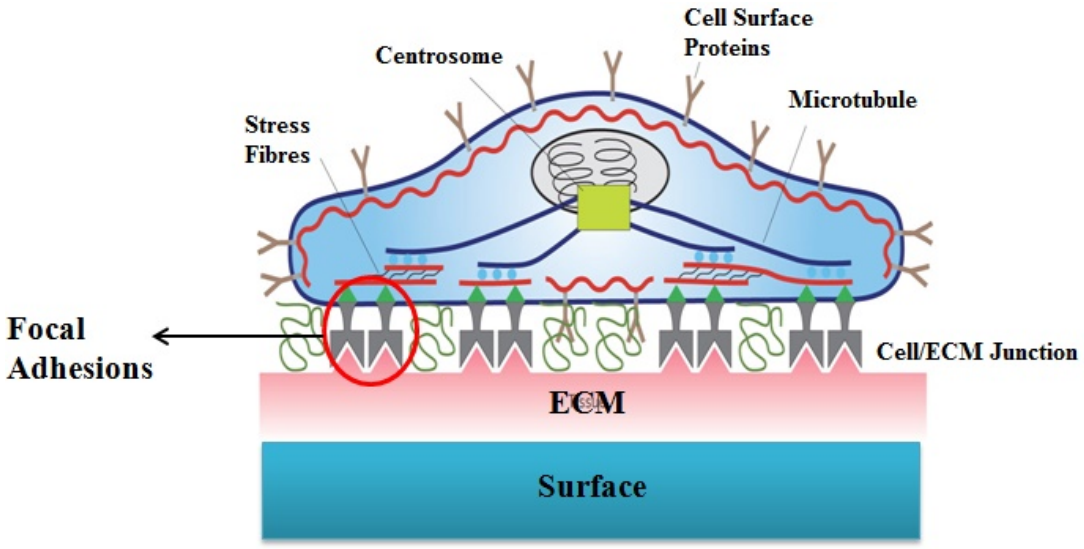

Figure 2.1: cell adhesion involves transmembrane proteins, integrins, connecting to the ECM on the substrate and cytoskeleton inside the cell [4]

tural support and also acts as a medium controlling signal transfer to the cells, thereby regulating their adhesion, growth, migration, differentiation and death. The cell/ECM junction is made through transmembrane proteins called integrins that bind the cell to the ECM constituents and are linked to the internal cellular structure (the cytoskeleton) (figure 2.1). These integrins are further organized to form micron sized clusters called focal adhesions (FAs), which are the region of intimate adhesive contact between cell membrane and the substrate. These focal adhesions ensure the mechanical connection and force transmission between the cell interior and the external matrix, allowing cells to react and adapt to their environment through a complex mechano-transduction process. focal adhesions form the most well-described cellular sites for sensing mechanical forces [7].

Just as integrins, cells have transmembrane proteins to establish connnections with other cells as well. These are a family of molecules such as cadherins, immunoglobins, selectins which have a higher degree of specificity in their function that enable cells to sense their environment. Cell-cell junctions permit to transmit signals from one cell to its neighbours and also regulate the extent of cell shape and rigidity, thereby controlling its adhesion and spreading.

In the biological context, cell adhesion to the ECM is critical to embryonic development, wound healing [8], [9] and enables cohesion, organization, and repair of numerous tissues [10]. Changes in cell adhesion are involved in a wide range of diseases such as arthritis, osteoporosis, and atherosclerosis [11–13]. Reduced adhesiveness is also generally seen in human cancer cells.

2.2.3 Cell adhesion and spreading

Cellular adhesion and spreading is a primary mechanism through which the development, maintenance and functioning of normal tissue structure is regulated. The establishment

of these connections, or lack thereof dictates the behaviour of cells to respond to their external environment. Cellular adhesion and spreading rely primarily on cytoskeleton dynamics and matrix adhesions as a mechanism to sense and respond to external inputs [14]. Multiple groups of proteins regulate the passive deformation and active reorganization of the cytoskeleton and thereby directly control the cell morphology, adhesion and migration. Cell spreading studies are useful model approaches for studying the factors regulating the cytoskeleton organization.

Although different types of cells have different modes of spreading, most generally, such process is characterized by the following stages (figure 2.2).

- Early phase initial attachment: The contact of the cell and its substrate calls for connections between cellular adhesion receptors (integrins) and the substrate bound ECM. Anchoring of cells onto substrates starts with the binding of ligand receptor pairs. This facilitates adhesion and forms the nexus to transmit informations. The strength of adhesion becomes larger with the time a cell adheres onto a substrate.

- Intermediate phase: Cells continue to flatten and spread onto the substrate, resulting in an increase in the number of integrin mediated adhesions, decrease of cell height, and subsequent increase of contact area. Matured adhesion sites begin to disassemble due to prolonged integrin binding activity. Protrusive forces are generated at the cell periphery resulting in generation of new adhesion sites.

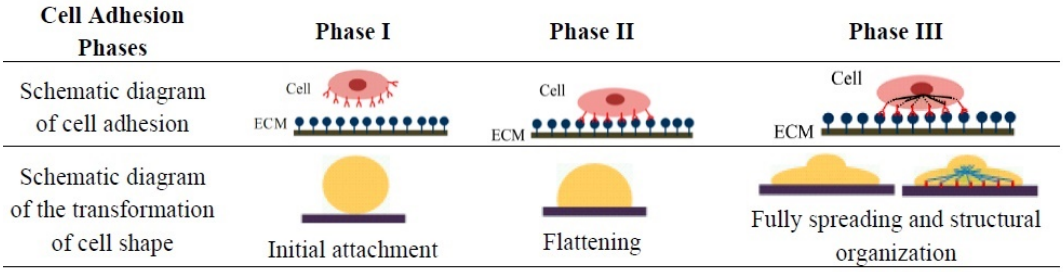

Figure 2.2: Schematic showing cell adhesion and spreading [15]

- Late phase: Once the spreading achieves its critical spread area, the cytoskeleton contracts and exerts forces onto the substrate. The cell contraction promotes reorganization of adhesion molecules and reinforces adhesion sites. Integrin clustering is promoted, thereby leading to maturation of focal adhesion.

2.2.4 Cellular forces

Cellular contact takes place primarily with other cells (cell-cell adhesion) or with the extra cellular matrix (ECM) through cell matrix adhesion. These contacts give rise to forces exerted on the interface between the cell and its point of contact. These forces in turn directly feed the cellular regulation. As an example, bone cells that become inactive in the absence of any mechanical input [16], and fibroblasts need mechanical stress during tissue maintenance and wound contraction [17].

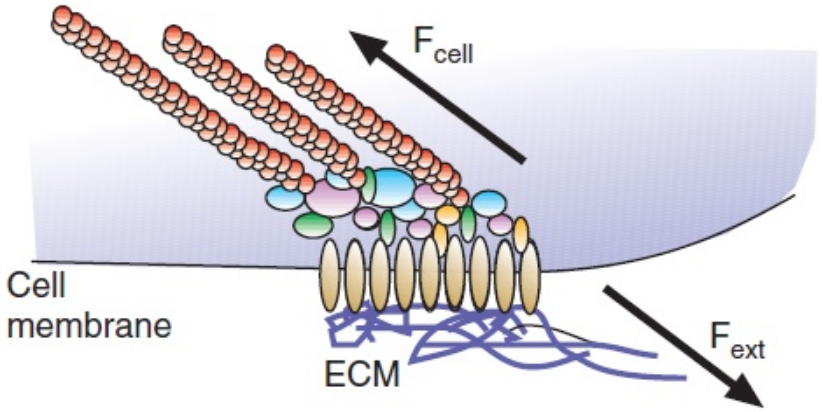

Figure 2.3: Schematic showing the balance of external and internal forces (F_{ext} and F_{cell}). These two forces define the proper functioning of the cells. Image taken from [18]

Cells govern tissue shape by exerting highly regulated forces at the site of matrix adhesion [19]. Focal adhesions form the central point at which forces are generated onto the substrates. The adhesive strength of focal adhesions affects the forces that a cell can exert on its surroundings and is involved in a variety of processes controlling cell growth, differentiation or migration. A cell, while probing its environment (figure 2.3), initiates adhesion through actin dependent (red) protrusions that bring integrins (brown) at the leading edge in contact with the matrix (blue) where they can bind. The binding of integrins to the ECM is rapidly followed by integrin binding to the actin cytoskeleton resulting in an inward force generated towards the cell centre (F_{cell}). A cytoskeletally generated force leads to stress in the focal adhesion because an equal and opposite reactive force arises in the ECM (F_{ext}). Conversely, an externally applied force through the ECM results in stress at the focal adhesions when the actin cytoskeleton provides an opposite, reactive force that balances the applied force. A balance of intracellular forces with the exogenous forces is required for the maintenance of basic cellular functions.

2.3 Cell-substrate interactions

The possibility of *in vitro* cell studies allows gaining deep insights into the dynamics of cellular processes. Building a consistent and reliable extrapolation of *in vivo* cell microenvironment however presents several challenges in order to increase the understanding of cellular complexities.

- Forces: *In vitro*, most cells are anchorage dependent and attach firmly onto the substrates through adhesion domains. Although the attachment of focal adhesions have been studied for decades, much less is known about the source and coordination of mechanical effects on cell behaviour. The measurement and mapping of transmission forces through the adhesion sites is not a simple task. The small dimensions of individual adhesion sites, their spatial proximity, and the small magnitude of forces involved make it challenging to accurately measure and map these sites.

- Surface properties: Although culturing cells *in vitro* is convenient, it is difficult to reproduce the organization and function of the ECM [20]. Cell adhesion studies frequently involve substrates made of glass or polystyrene coated with ECM proteins [21]. However their usefulness is limited owing to the complexity of these interactions. Conventional substrates have a certain degree of surface quality and there are several parameters which can influence the cellular response. Cells can also remodel the surface by secreting their own ECM which complicates the adhesion studies.

One important factor, in these cases, are the mechanical properties of the underlying substrate. Cells have the ability to discriminate a substrate in terms of its rigidity to allow them to differentiate and perform their tasks efficiently. Regenerative medicine [22, 23], or drug screening techniques employing cell-based assays [24,25] require the control of adhesive interactions of cells on man-made substates. Moreover, the regulation of adhesion feedback is also important for tumorigenesis [26]. Hence, controlling and understanding the adhesive interactions between cells and a substrate are both a fundamental and technological challenge.

Owing to this, requirements range from designing of substrates that can closely mimic the cell environment [27] to the control of cell adhesion in space and time in order to create well defined mono or multi-cellular arrangements [28].

2.4 Tissue engineering and material science

Tissue engineering combines cellular biology, engineering and materials science, along with suitable biochemical and physicochemical factors to create tissue-like structures. It aims at developing bio-compatible scaffolds that reconstitute the cell-adhesive responses central to numerous applications. Cellular systems are robust and dynamic, thus able to adapt to environmental changes. Learning from nature, tissue engineering has demonstrated its potential in helping to understand such non-trivial processes by building adaptive materials to study cellular mechanisms [29] .

The key need of tissue engineering is to provide a cellular environment for cells to function as they do in tissues. Often, the environment mimics the essential aspects of *in vivo* cellular organization by proper control of mechanical and chemical settings. Cell scaffolds often serve one of the following functions:

- Cell attachment and migration
- Retention of biochemical factors
- Adequate diffusion of nutrients and waste
- Mechanical rigidity or flexibility

While the study of cell-substrate adhesion has gradually matured in cell biology, a quantitative understanding of how the interactions of individual components gives rise to rich cellular behaviors has emerged over the years. Current challenges for engineering and material science in cell biology are therefore manyfold: they range from the design

of biomimetic scaffolds to investigation tools required for understanding the complexity of cell-surface interactions. Several directions are thus explored in the elaboration of cell culture substrates, based on strategies that depend on the goal to be reached.

2.5 Scaffolds mimicking the extra cellular matrix

Scaffolds are 3-dimensional matrices that essentially act as templates onto which cells are seeded. They provide the appropriate environment for cells to grow, replicate and allow tissue formation [30]. The cell-seeded scaffolds can either be cultured *in vitro* to synthesize tissues that can be transplanted to injured sites, or can be directly transplanted onto the target sites thereby inducing *in vivo* regeneration of tissue cells. In addition to providing a proper geometry for tissues to grow, the scaffolds can be used as drug carriers to activate specific cellular functions [31].

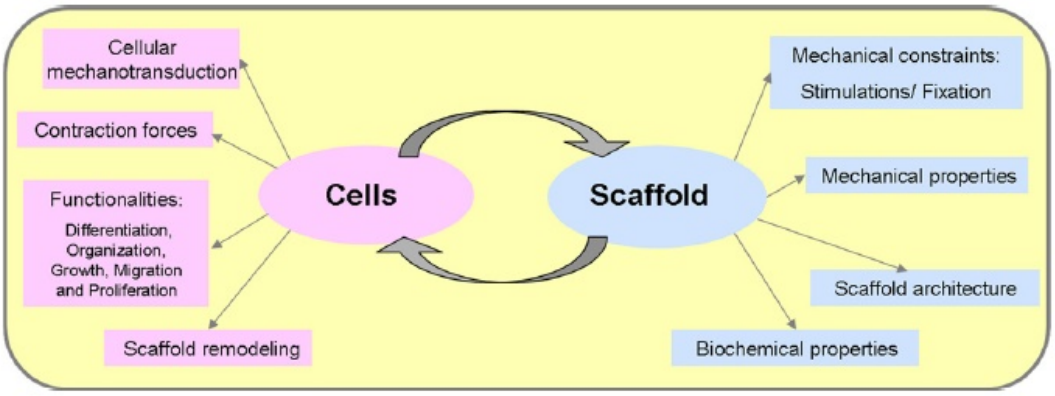

Figure 2.4: Schematic showing the key elements in the interplay between cells and scaffolds. The scaffold affects the cell through its architecture and overall properties [32]

De novo tissue genesis is not exactly similar to a developmental or a wound healing program as tissue engineering aims for an accelerated cell growth protocol as compared to the natural cellular regeneration. In addition, there are always concerns over immune rejection and pathogen transmission when using a natural ECM. This calls for artificial scaffolds having features as close as possible to that of real tissues [33]. Scaffolds produced from a variety of sources have been used so far in tissue engineering. However, regardless of the tissue type, a number of key considerations are important when determining the suitability of a scaffold (figure 2.4).

- Biocompatibility: Since cells cultured on such substrates have to be transplanted *in vivo*, these scaffolds have to be biocompatible and biodegradable.

- Mechanical Properties: scaffolds with cell adhesive mechanical and growth kinetics are required [34] to optimize the growth of tissues.

- Surface properties: Modifying the surface density and spatial distribution of surface attachment sites allows defined modulation of specific cellular functions [35].

Biomolecular recognition of a scaffold is achieved by incorporating a bioactive molecule in it through physical or chemical means. Modified scaffolds can be used as a tool to elucidate a cellular behaviour in a defined manner. Works using long/short protein chains and peptides such as RGD(Arg-Gly-Asp) for surface modifications of a number of materials such as glass [36], quartz [37], and metal oxides [38] have elaborated cell proliferation [39]. Attempts have been made to engineer *in vitro* many organs and tissue of the body. To date the most successful attempts have been made in skin [40], bladder [41] and bones [42]. Ongoing research focuses on developing sophisticated 3D biomimetic scaffolds to incorporate functional properties.

Engineering of surfaces that either prevent or enhance cell adhesion or protein adsorption represent an extremely active area of biomaterial research. Although a number of goals have been achieved using 3D cell culturing, efforts are required to design micro and nanoscale 2D scaffolds. Modelling 2-D surface based cultures allows manipulation of the cell-surface interactions at single cell level. This allows to address fundamental questions regarding complex mechanisms of cell adhesion, proliferation and migration and lifts some of the design constraints of 3-D scaffolds, such as nutrient supply.

2.6 Cell patterning

The *in situ* micro-environment of cells provides a variety of cues that influence the architecture, mechanics, polarity and functioning of the cell. It imposes specific boundary conditions which influence the spatial distribution of cell adhesion sites. However, these important properties are generally lost during *in vitro* cell culturing.

Cell patterning allows fabrication and use of a culture substrate with microscopic features that impose a defined adhesion pattern. Constraining the shape and location of specific cell surface areas has a dramatic effect on cellular development. Spatial control of adhesion between cells and synthetic substrates is a major key to many biotechnological and biomedical applications [23]. Tailoring the two dimensional organization of single or multiple cells onto the cultured surfaces allows for instance:

- To provide complex microenvironment for individual or multi-cellular arrangements and thereby reconstitute the physiological *in situ* conditions for controlled *in vitro* culture.
- To control the geometry, and hence the internal organization and polarity, of single cells adhered on a regular 2D network.
- To design tissues of well-defined architectures mimicking the complex *in vivo* arrangement and functioning of cells [28].
- To achieve a high throughput and reproducible regulation of embryonic stem cell differentiation for cell transplanting protocols [43, 44].

This not only provides a means to perform reliable statistical analysis of cellular response to environmental cues [45, 46], but also to investigate the relation between cell shape and function [47, 48].

2.6.1 Imposing geometric restrictions to study cellular behaviour

Modulation of the pattern geometry allows, for example, the analysis of the mechanisms governing the determination of cell shape in response to external adhesive conditions. Cell acquires a shape in two stages. Initially, the cell forms contact with the designed pattern where the cellular contact define the apices of the cell shape. Later on, the cell borders that link the apices move so as to minimize the distance between them.

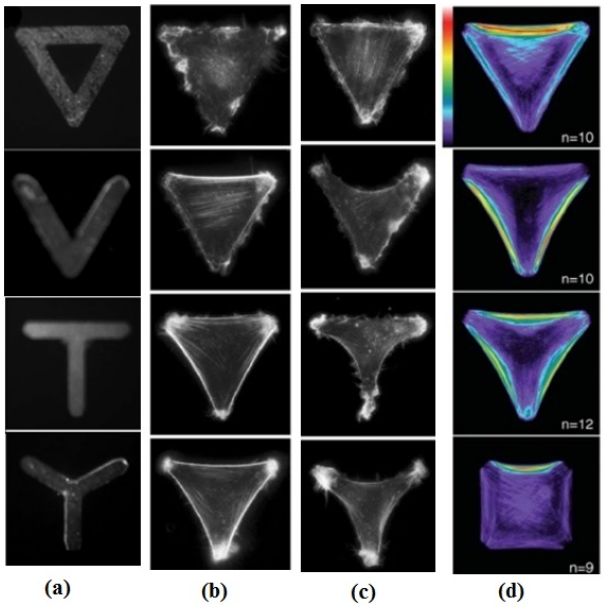

Figure 2.5: Effect of geometrical constraints on cell response. (a) fibronectin micropatterns onto which the RPE1 cells are constrained on. (b) actin cytoskeleton revealed by phalloidin staining in control conditions. (c) staining in the absence of cytoskeleton contractility. As compared to the topmost frame, cells on the V, T, Y frames lost their contractility. (d) average distribution of actin in cells placed on [V], [T] or [Y]. Higher intensity distributions highlighted that stress fibers appeared stronger upon non adhesive edges. [49]

Experimental works [49] have shown the manipulation of the location of adhesive and non adhesive zones within a given convex cell envelope. Retinal Pigment Epithelium 1 (RPE) cells were plated on fully adhesive and patterned non-adhesive triangular, [V], [T], or [tripod] shaped micropatterns (figure 2.5(a)). Different combinations of areas provided stringent boundary conditions to cell anchoring machinery. The cell contractility was probed by maintaining the cell for a long time in a fixed geometry (figure 2.5(b)) and then treating with an inhibitor to disrupt the acto-myosin contractility. After treatment with the inhibitor, cells plated on the triangular frame did not show any significant shape change. In contrast to that, On [V], [T], or [tripod] shaped non-adhesive patterns, the membrane border sagged on the non-adhesive edges but remained anchored on adhesive edges (figure 2.5(c)). This revealed that tension was not identical in all edges in spite of shape symmetries. Instead, it was highly localised towards non-adhesive edges as suggested by F-actin staining (figure 2.5(d)). The focal adhesions (and the actin cables revealed by phalloidin staining), were distinctively distributed along the non adhesive edges of the patterns. This allowed analyzing the impact of cell adhesion pattern onto

cell shape and cytoskeleton architecture.

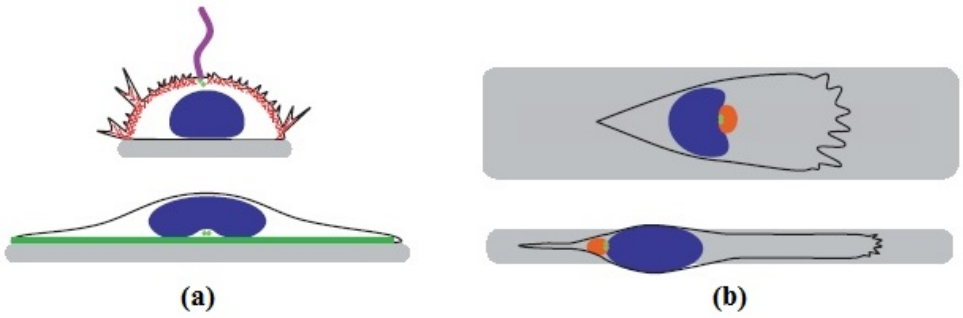

Figure 2.6: When confined to a small micropattern, a cell grows primary cilia on its dorsal surface (with actin(green) and tubulin (magenta) as a marker for primary cilium). By contrast in a cell grown on a large micropattern, the centrosome is close to the ventral surface without the primary celium. (b) on wide tracks (top), a cell migrates with its centrosome (green dot) in the front preceded by golgi complex (orange), whereas on thin tracks (bottom) it migrates with its centrosome in the back. the shaded blue area is the nucleus. [47]

Cell adhesion further guides the actin assembly and orients the establishment of cell polarity. For example, cells spread on an enlarged micro-contact area spread fully through the stress fibers, whose contractility perturbs the growth of primary cilia from the cell, which is not seen for the case of a small micropatterned area (figure 2.6(a)). The orientation of the actin cytoskeleton and its polarity in response to geometrical cues governs cell migration as well. Cells grown on thin lined substrates migrate faster than those grown on a homogenous wide substrate surface and display most of the characteristics of cell front and cell body(figure 2.6(b)). [47]

2.6.2 Suppressing non-specific cell substrate interactions

Suppression of interactions between a surface and the ECM proteins contained in the culture media are of crucial importance for successful cell patterning. A number of surfaces have been developed so far to resist adsorption, and also facilitate specific binding of bio-molecules. This requires understanding the relationship between the structure of the surface and its properties [50].

Self Assembled Monolayers The most widely used surfaces are based on Self assembled monolayers (SAMs). These are molecular assemblies formed spontaneously on surfaces by adsorption and organized into more or less large ordered domains [51, 52]. Typically a SAM is composed of a head group, tail and a functional end group. Two types of SAMs, alkanethiolates on gold and alkylsiloxanes on hydroxylated surfaces have been used to study the interactions between a man-made surface and a biological medium (figure 2.7) [53]. The silane based SAMs are thermally more stable, but are limited in the range of functional groups that can be displayed at the surface.

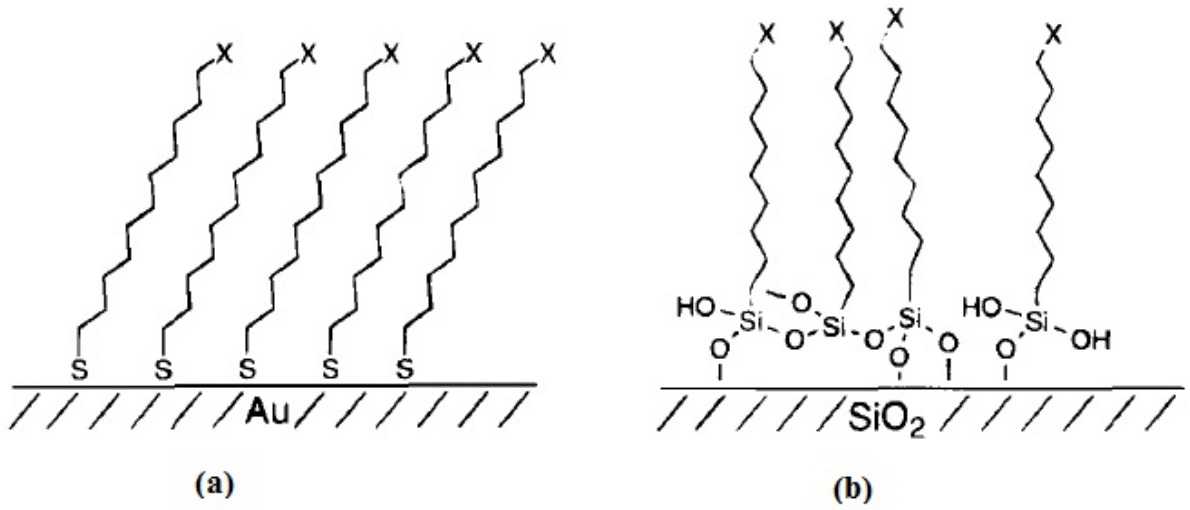

Figure 2.7: Different types of SAMs based on (a) alkanethiolates on gold and (b) alkylsiloxanes on hydroxylated surfaces. [53]

The most successful method to confer resistance to non-specific adsorption of proteins has been to coat the surface with poly(ethylene glycol) (PEG) [54, 55]. The effectiveness of oligo(ethylene glycol) (OEG) groups, combined with the ability of SAMs to present a range of groups in controlled environment, makes this system well suited for studies of biospecific adsorption.

2.6.3 Patterning cell adsorption and adhesion

Protein adsorption using SAMs Patterned SAMs have been extensively used to control the adsorption of proteins onto surfaces. Microcontact printing was used to pattern a SAM into regions terminated with methyl and oligo(ethylene glycol) groups. Immersion of these SAMs in aqueous solutions containing proteins resulted in adsorption of monolayer of protein only on the methyl-terminated regions which could be further imaged by scanning electron microscopy (figure 2.8). SAM patterned regions terminated with methyl and OEG groups permit spatial control over the attachment of cells [56, 57]. The same protocol was used to direct the attachment of cells onto surfaces.

A number of techniques have been used so far for cell patterning. Some are still at an early stage of development (e.g. laser guided cell deposition), whereas others benefit from several years of applications (e.g. microcontact printing, UV patterning, inkjet printing, patterning by lift-off etc). Cell patterning methods have until now provided evidence for the intricate coupling between the geometrical constrains imposed to a cell and its growth, division, proliferation and death [47, 48]. However, well-established micropatterning methods used so far yield essentially static arrays of cells adhered in a fixed geometry, while cell adaptation to a given spatial confinement is a dynamic process involving cell re-arrangements in response to the sensed adhesive environment. This has been a major limitation for statistically sound studies of adhesion dynamics at the single cell level. Also, the design of systems allowing for dynamic patterns is still a new field which requires in-depth study.

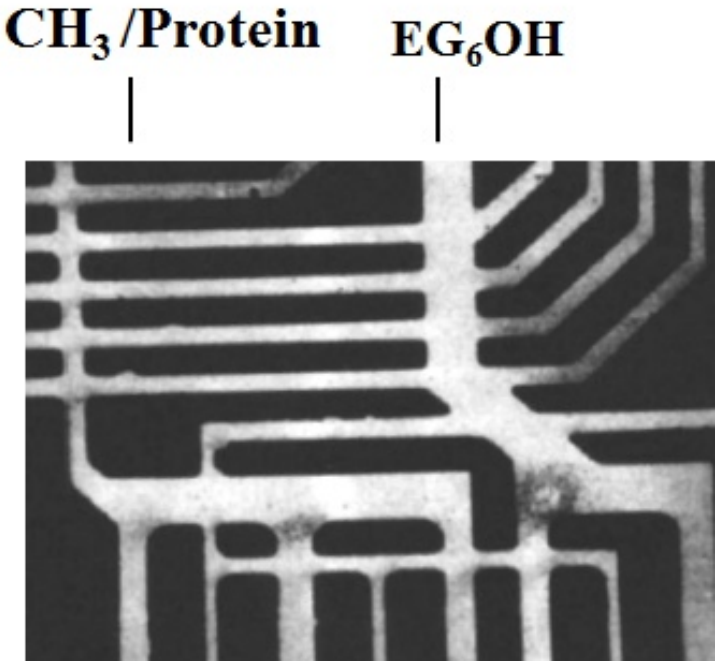

Figure 2.8: Scanning electron micrograph of fibrinogen adsorbed on a patterned SAM. A patterned hexadecanethiolate SAM on gold was formed by microcontact printing, and the remainder of the surface was derivatized by immersion in a solution containing a hexa(ethyleneglycol)-terminated alkanethiol. The patterned substrate was immersed in a solution of fibrinogen (1 mg/mL) in phosphate-buffered saline. Fibrinogen adsorbed only to the methyl-terminated regions of the SAM, as illustrated by the dark regions in the micrograph. [57]

Proteins have been immobilized onto SAM surfaces by either adsorption [58], or covalent bonding to the SAM surface [59]. Different classes of SAMs of thiol based molecules removed [60] or degraded electrochemically [61], SAMs containing photo-cleavable groups [62, 63], or Poly(Ethylene-Glycol) based coatings selectively oxidized under focused UV light [64] have been developed so far. Such systems have been used to control, at the micron scale, cell migration [62], or shape [64]. Novel and simple methods for surface patterning in live cell cultures offer precise control in real time of cell shape modifications and of intracellular architectures [64] (figure 2.9).

The working principle involved creating and altering cell patterns from a deposited thin film upon application of a local stimulus that induced desorption of the anti-adhesive molecules and exposed the underlying surface. When this was done at the periphery of an adhered cell, it triggered cell motion/spreading towards the freshly de-protected regions. Cell shape variations were studied via desorption of the PEG regions. It was possible to remove PEG from a region defined by a horizontal bar next to an apex of a triangularly-shaped cell constrained on a V-shaped (figure 2.9(a)). After ablating the region with a laser source, the cell also adhered to this region and adopted a square shape (figure 2.9(b)). Actin network reorganized during this cellular transformation. As the cell spread on the new bar, it formed new actin cables, which connected the original and the new micropatterns. This allowed cells to spread on the designed regions and also

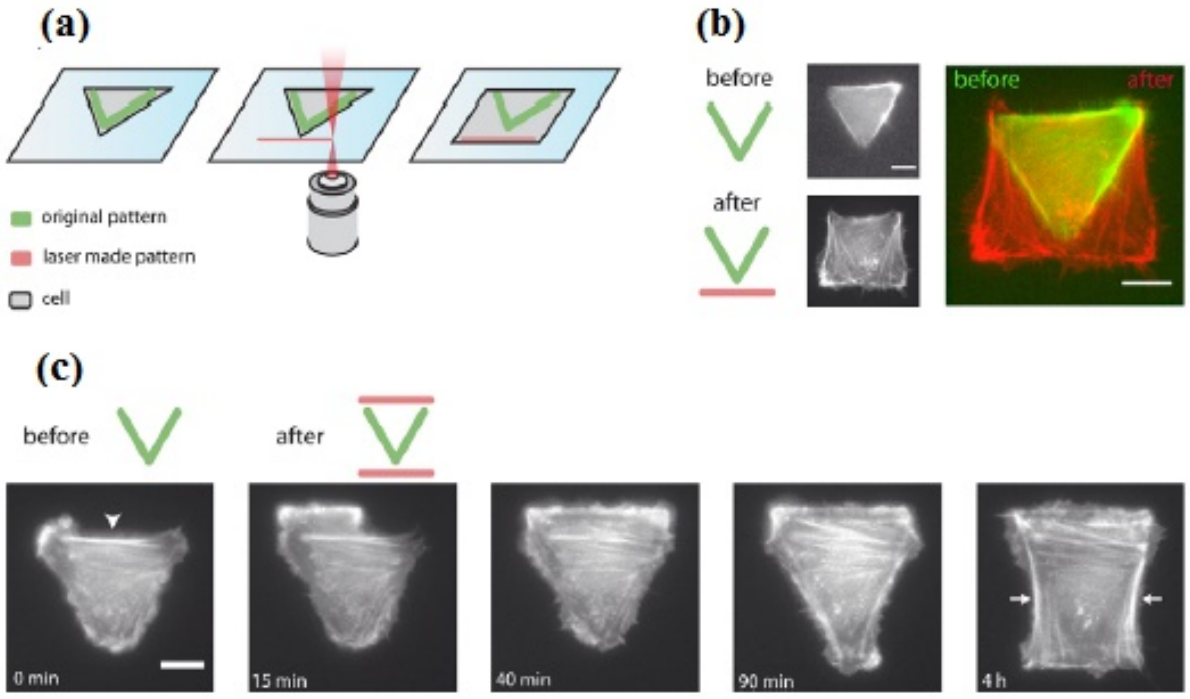

Figure 2.9: (a) cell shape constrained on a classical micropattern (green). A pulsed laser is used to create new adhesive regions (red) to reprogram cell shape. (b) The cell is constrained to have a V-shaped micropattern (top green in overlay) and then reprogrammed to become square (bottom red in the overlay) by drawing a bar below the V shape with the laser. (c) Monitoring the cell shape change: A cell is first constrained on V shaped micropattern and reprogrammed to become rectangular by adding two horizontal bars above and below the original micropattern. Cell shape changes were monitored by microscopy. images adapted from [64].

to develop new internal cables ensuring cell shape deformation from triangle to square (figure 2.9(b)). Cell shape changes were further investigated by adding two bars. As the cell shape changed, some peripheral actin cables disappeared whereas others were assembled (figure 2.9(c)). This suggested that cell shape reprogramming is supported by complex remodeling of intracellular structures.

2.7 Smart materials for cell adhesion control

Surfaces with stimuli responsive properties, also known as smart surfaces, have attracted substantial research interest in the past few years. Such advanced surfaces are designed with specific properties that can be significantly altered in a controlled fashion by an external stimulus. Advantages that are expected from such switchable interfaces include ease, speed, reversibility, temporal and spatial control over bio-interfacial interactions. A major motivation in designing such systems is the possibility they open to study cell adhesion dynamics, and to guide cell migration in order to dynamically build tissues. A wide range of stimuli are available for applications involving switching. Out of the numerous parameters, light, temperature, pH, electric field and ionic strength are most

commonly used [65–68].

Such systems can be tuned in a predictable manner and have a wide spectrum of applications. For instance, surfaces with changes in properties such as wettability have been employed in the development of microfluidic devices [69], actuators and sensors [70]. With the development of micro and nanotechnologies, controlled switchable surfaces have been employed for bioanalysis, protein immobilization and so on [71, 72].

An important research area focuses on developing substrates that can dynamically regulate various cellular phenomenon in response to an applied stimuli. Cellular responses such as attachment to material surfaces, changes in morphology, proliferation, and phenotypic changes have been shown to be linked to the concentration, composition and conformation of the layer of proteins that adsorb rapidly on the synthetic materials. Despite several years of studies involving cell adhesion onto surfaces, achieving proper control and understanding of cell substrate interactions is still difficult. To overcome this limitation, rationally designed stimuli responsive surfaces that can switch their properties from cell adhesive to repulsive state on demand have developed over the years [73]. There has been considerable progress in the design of materials and interfaces that can be used to reversibly switch between adsorbent and adsorption-resistant properties.

Switchable surfaces fall into several categories

- Self assembled mono and multi-layered thin films
- thin films of polymer networks
- grafted polymer thin films

2.7.1 Self assembled monolayers (SAMs)

Dynamic SAM substrates for controlling cell adhesion on demand present new possibilities for studying the responses to alternations in cells' immediate environments. SAMs based dynamic substrates involve switching the composition of cell binding ligands on a substrate surface between an active and an inactive state. Adhesion control using responsive SAM-based surfaces has been achieved using electrochemical, temperature, light, ionic field strength or the presence of small molecules or biomolecules [74].

Electrochemical adhesion/release control Revzin and co-workers [75] reported the release of captured T-lymphocytes on antibody-presenting SAMs of alkanethiols on gold electrodes. T-cells were immobilized on SAM having anti-CD4 antibodies on the surface. Non-specific adhesion was prevented by coating with a PEG-terminated silane layer. Application of a reductive potential to the gold electrode resulted in desorption of the antibody functionalized alkanethiols and subsequent release of the T-cells from the surface.

Chan and Yousaf [76] provided a switch-on adhesive system using swiss 3T3 fibroblast cells on a surface using mixed SAMs of hydroquinone and tetra(ethylene glycol) alkanethiols. Cell immobilization was only observed on the regions patterned with hydroquinone

terminated SAM. The application of a positive potential oxidized only the hydroquinone to reactive quinone resulting in a patterned immobilized surface.

Mrksich et al [77] combined the electroactive immobilization and release of peptide ligands using SAMs creating adhesive substrates that could be switched on-off-on. They used two different electrochemically active SAMs, each having affinity for peptide ligands, and showed the adhesion modulation of swiss 3T3 fibroblast cell. The dynamic interface was based on SAMs that incorporated an O-silyl hydroquinone functionality presenting an RGD ligand (figure 2.10).

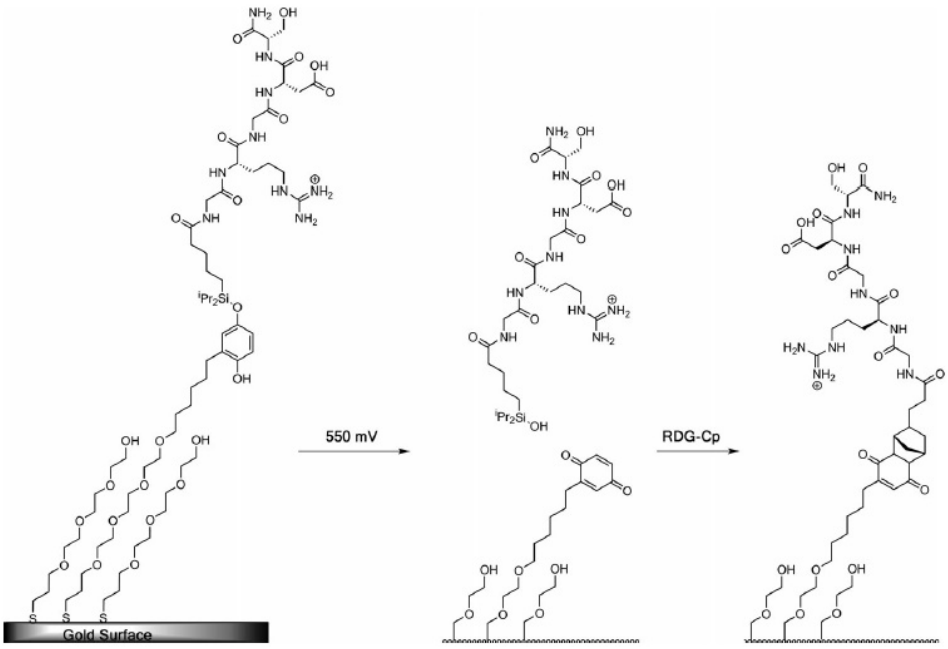

Figure 2.10: A circularly patterned hexadecane thiol SAM on a gold substrate. The remaining substrate was functionalized with a mixed SAM of RGD aklanethiols and tri(ethylene glycol)-terminated alkanethiolate. O-silyl hydroquinone is oxidized to benzoquinone with resulting hydrolysis of the silyl ether and selective release of the RGD ligand by application of a potential. The resulting benzoquinone reacts with a cyclo-pentadiene-tagged peptide (RGD-cp), via a Diels-Alder reaction, which selectively immobilizes the second ligand [77]

The electrochemical desorption often results in adherent cells to reunite the surface. This results in reduced control over cell-surface interactions in terms of unwanted spreading of the adherent cells. Desorption of the bioinert SAMs from a surface allows cells to roam, impeding efforts to determine the interactions that are essential to a cell's vitality.

Oxidative Release Wittstock and co-workers [78] reported an in situ based method for switching of bioinert OEG-terminated SAMs to cell-adhesive SAMs by exposure of oxidizing agents such as Br_2. The bromine was generated electrochemically in aqueous media. The limitation of reversibility however remained.

Thermally controlled switching Temperature stimulation is a convenient method widely used for controlling the biological properties of surfaces. Mixed SAMs of OEG-terminated alkanethiolates and methyl(CH_3) terminated alkanethiols have been demonstrated to exhibit different tendencies for protein adsorption and bacteria attachment at room temperature and at 37°C [79]. For the case of such SAM based surfaces, the reversible switching between non-adhesive (room temperature) and adhesive (37°C) state has not been observed. Such systems lacked describing the exact mechanism by which protein adhesion is modulated.

Light controlled reversible switching Using light to alter cell adhesiveness of a substrate surface allows for increased spatial control of patterning of cell cultures in various shapes and sizes with minimal perturbations of the established cultures of cells. Additionally, this permits the alterations of cell adhesive regions at will.

A method for dynamic control of cell adhesion to predetermined regions on a substrate was reported by photoactivation [80]. The strategy relied on SAM containing photocleavable 2-nitrobenzyl group (figure 2.11). Subsequently, the substrate was coated with bovine serum albumin (BSA), to render the surface inert to cell adhesion. Irradiation changed the hydrophilicity of the substrate by changing the nitrobenzyl group to a carboxylic acid terminated group. This diminished the affinity for BSA to adhere on the surface resulting in dissociation of protein from the surface. The addition of fibronectin led to its adsorption to the carboxylic group. Subsequently, cell lines could be adhered.

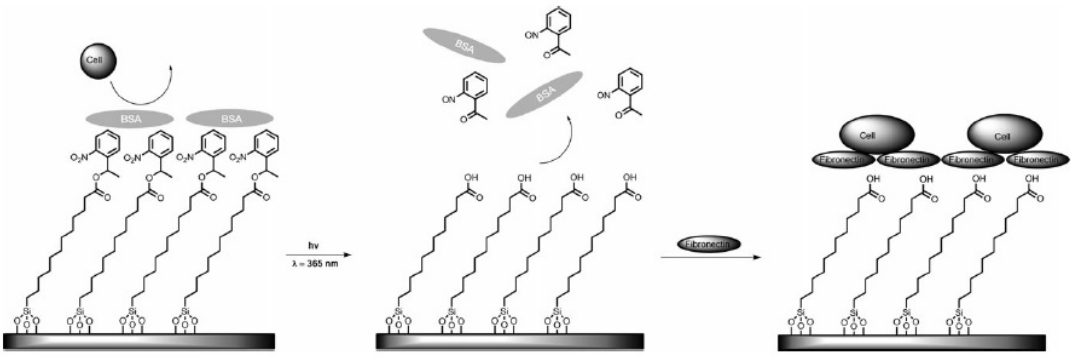

Figure 2.11: UV directed elimination of BSA and subsequent adhesion of fibronectin changes surface adhesiveness from a state that prevents cell adhesion to a state that promotes cell adhesion [80].

A spectacular approach to switching SAM properties involved reversible conformational transitions of the assembled molecules in the SAMs. Taking advantage of photosensitive molecules, Liu et al [81] reported on the design of dynamic photo-responsive SAMs made of molecules bearing the cell binding RGD peptide (Arg-Gly-Asp). The coupling of RGD was done via a photosensitive azobenzene group. The reversible change in conformation of the azobenzene group upon irradiation with UV or visible light was used to expose or hide the RGD site at the cell/surface interface, thus successfully changing the cell affinity for the substrate (figure 2.12).

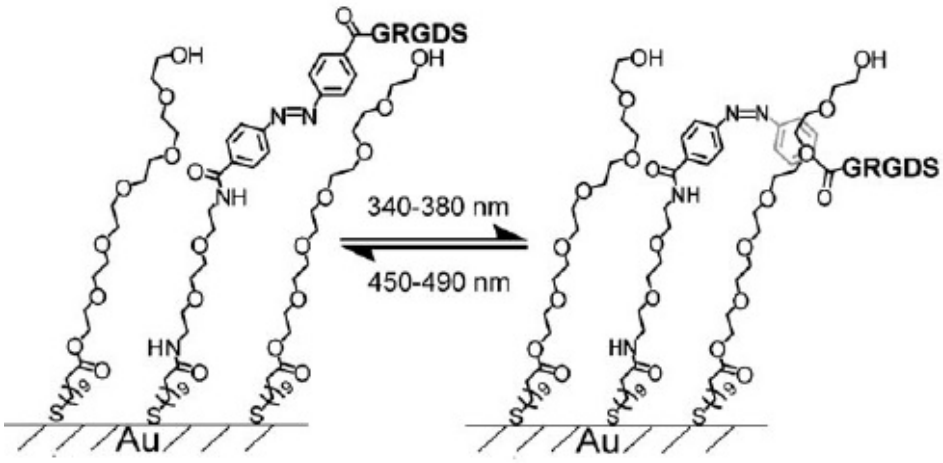

Figure 2.12: The azobenzene moiety can be converted photochemically between the E and Z configurations to either present or mask the RGD ligand and hence modulate biospecific cell adhesion. Adapted from [81].

The reversible adhesive switching described above was not used for dynamic adhesion control, but only as a means to reset the overall adhesive state of the surface in between successful cell culture attempts. Moreover, cell detachment was not observed to happen spontaneously after photoswitching and required an additional step of concurrent peptide adsorption from the bulk culture medium.

Pioneering works based on SAM have described the dynamic switching of protein adsorption/desorption. However, the mechanisms of reversible cell adhesiveness are still unexplored through SAM based surfaces. Varying stimulus inputs have shown that SAM based substrates most likely lack the local mechanical actuation that would allow for efficient cell detachment [74]. Moreover, the adsorption of several model proteins to SAMs depends on the choice of the terminal functional groups which induces selectivity in the exploitation of SAM properties. Studies aimed at probing the dynamic coverage and release of cells onto surfaces call for designing surfaces that display generic mechanisms allowing to switch cell adhesion irrespective of the cell types.

2.7.2 Stimuli responsive polymeric surfaces

The increasing need for robustness in biomedical and engineering materials has generated a growing interest for stimuli responsive polymeric materials. The solubility, volume, configuration, and conformation of these systems can be reversibly altered by chemical and physical signals. Changes in signals such as pH, metabolites, temperature, and light alter the molecular interactions of polymeric systems thereby giving rise to a reversible microphase separation. Surfaces modified with responsive polymers allow dynamic altering of their physico-chemical properties in response to the changes in the applied stimuli. Such systems provide the possibility for fabricating functional materials that find applications in controlled drug delivery, bio-separation, protein purification, viscosity modifiers, chemical sensing, drug release, cell growth and separation.

Polymeric films can be prepared on substrate surfaces using several deposition techniques having varying complexity and applications. Methods such as spin coating, chem-

ical vapour deposition, laser ablation, chemical or electrochemical reactions have been prescribed previously to fabricate polymeric films [82–84]. However there are several technical challenges associated while designing controllable surfaces which can be altered at will.

Surface tethered polymers, known as polymer brushes, have recently emerged as an extremely versatile approach to create polymer films in a robust and controlled way. Polymer brushes are long chain polymer molecules attached with one or with a few anchor sites to a surface. While SAMs offer ease of preparation and a versatile surface chemistry, polymer brushes offer advantages in providing better control over surface coverage, thickness and composition which are necessary in designing smart substrates for desirable target objectives. Controlled /living polymerization protocols such as Atom Transfer Radical Polymerization (ATRP), Reversible Addition Fragmentation chain Transfer polymerization (RAFT) [85] have provided a versatile route for the synthesis of polymeric surfaces with precisely controlled physical properties.

Thermally actuated polymers Polymer chains exhibit temperature dependent solvation behaviour due to enthalpic effects [86]. Designing temperature dependent polymeric surfaces allows expansion and collapse of the tethered macromolecules in response to changes in temperature. A significant body of work during the past years have established a class of thermally responsive polymer surfaces that have been used to control cell attachment and detachment without cell damage [87].

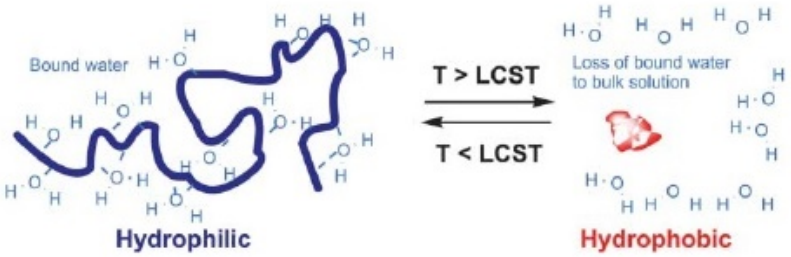

Figure 2.13: Schematic showing the response of PNIPAM based polymeric solutions as a function of temperature [88]

The most commonly studied thermoresponsive model till now is based on Poly (N-isopropylacrylamide) (PNIPAM) [88, 89], due to its sharp phase transition temperature and biocompatibility. PNIPAM undergoes a phase transition near its lower critical solution temperature (LCST) in aqueous solutions around 32°C (figure 2.13). This transition is attributed to a shift in the distribution of hydrophobic and hydrogen bond interactions. Polymer chains reversibly switch between a soluble, swollen state at low temperature, and a hydrophobic, collapsed conformation at temperatures greater than the LCST. Cells cultured on PNIPAM above its LCST adhere and proliferate, while lowering the temperature of the culture medium below 32°C induces cell detachment. The above phenomenon depends on the density of polymeric chains grafted onto substrates. Since its successful applications, many copolymeric systems have been designed in order to shift the transitions towards desirable working temperatures.

Thermoresponsive coatings for cell adhesion studies. The temperature sensitive characteristic of PNIPAM produces rapid changes of surface properties that make them applicable for switching the attachment and release of cells and cell sheets. This field was pioneered by the group of T. Okano, who used thin PNIPAM layers as the substrates on which cells adhered and proliferated at 37°C and could subsequently be detached by simply lowering the temperature of the surface below 32°C, without degrading the constituents of the secreted extra cellular matrix [90] and maintaining the cell vitality. This has allowed the development of a tissue construction technique called cell sheet engineering which involves the detachment of cell monolayers while preserving the integrity of the cell/ECM junction [91].

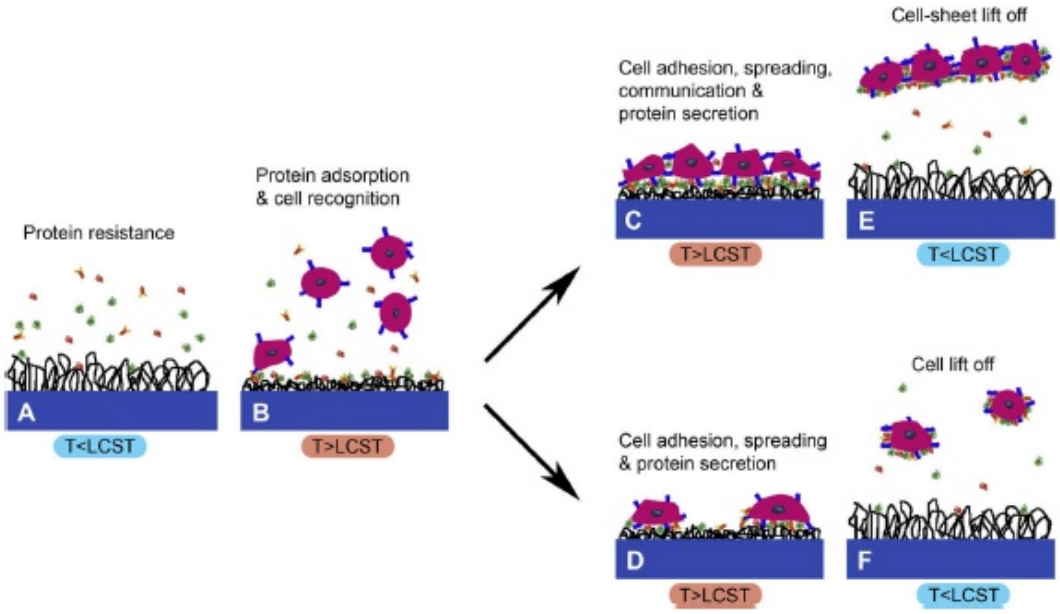

Figure 2.14: A model for thermosensitive cell attachment. (A) surface prevents protein adsorption below the LCST. (B), Raising the temperature allows adsorption of proteins and cell attachment. (C), Secretion of ECM proteins along with cell proliferation results in changes in cell shape.(D) Low seeding densities result in adherent cells without extensive cell-cell interactions. (E) cooling the temperature below the LCST allows the release of intact cells. [92–94]

The concept is based on the observation that substrates grafted with a low surface density of PNIPAM may support cell cultures at 37°C. The collapsed state of polymers allows proteins and subsequently cells to attach onto surfaces, spread and proliferate (figure 2.14). Reducing the temperature causes the coatings to hydrate, initiating the release of cells or intact sheet of cells. Removal of cells via the cooling of responsive coatings is advantageous as it prevents the degradation of cell-cell junctions and promotes ECM associated applications for tissue engineering and regenerative medicine. Since this first successful application, many studies based on cell sheets have focussed on the design of substrates for treating corneal epithelium dysfunction [95].

Reversible cell adsorption and release Protein-surface attractive and repulsive interactions are often discussed in terms of hydration states of brush grafted substrate. Although significant empirical know-how has been achieved regarding the PNIPAM-based cellular attachment and release, the physical mechanisms explaining the adsorption and release of proteins have remained unspecified. Theoretical suggestions explaining such mechanisms are very recent and focus on swelling/collapse degree as a function of hydration [96, 97].

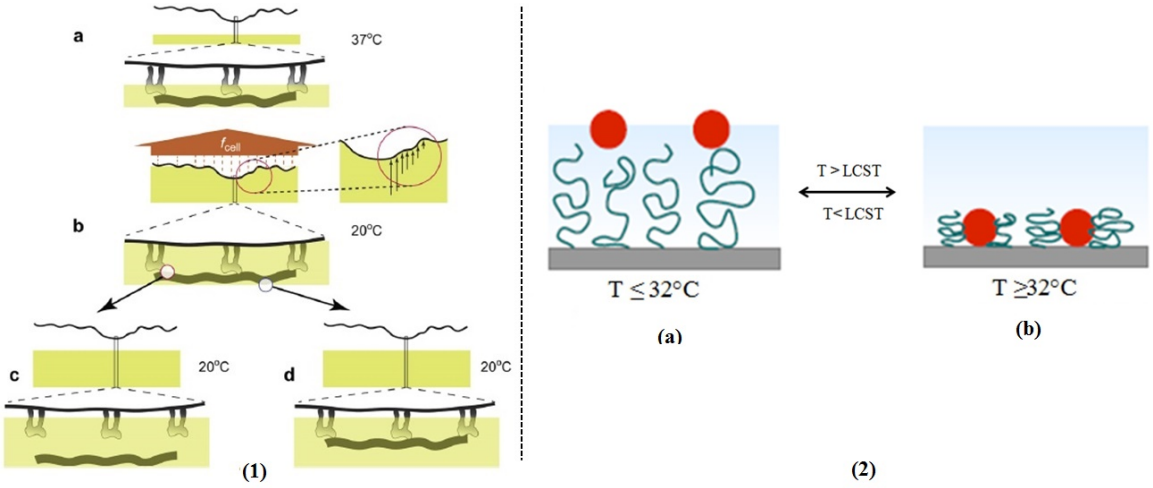

Figure 2.15: Schematic showing (1) the cell detachment mechanism upon lowering T. At T=37°C, the cell adheres with no brush confinement. (a) Brush confinement arises upon lowering temperature below LCST because of brush swelling underneath the adhering cell and gives rise to a disjoining force, F_{cell}. F_{cell} reflects the contribution of the local disjoining pressures whose amplitude increases with the local confinement. (b) F_{cell} drives dissociation of the integrin-ECM protein bonds (c) and /or desorption of the bound ECM proteins (d). (2) The adhesion and detachment of proteins on a PNIPAM brush based surface. Cell adhesion occurs on increasing the temperature beyond 32°C, whereas cells are harvested by lowering the temperature [96].

Theoretical studies based on PNIPAM brushes indicated that at temperatures higher than LCST, PNIPAM brushes collapse, thus reducing the steric contribution to repulsion that favors ECM protein adsorption and the cell adhesion. Protein adsorption on PNIPAM grafted surfaces is strongly affected by collapse/swollen mechanism (figure 2.15(2)). The events of chain collapse and re-swelling are:

- Brushes grafted on the surface lead to osmotic pressure penalty for protein insertion into the brush in a temperature dependent manner (figure 2.15(2)). This governs the protein adsorption, hence cell/substrate adhesion.

- Upon increase in temperature, the brush collapses, thereby lowering the osmotic pressure. This favours the adsorption of serum borne extra cellular matrix (ECM) components (figure 2.15(2b)).

- Once the cell is adhered, the collapsed polymer layer is confined between the cell membrane and the underlying surface (figure 2.15(1a))

- Upon temperature decrease, the swelling of the confined grafted chains generates repulsive forces that places the integrin-ECM bonds under tension. This accelerates their dissociation and promotes desorption of ECM proteins (figure 2.15(1b-d)).

Dependence of cell adsorption and release on the brush structure The molecular structure of the PNIPAM brush layer has been predicted to greatly influence cell adhesion [96]. Experimental studies performed on PNIPAM brushes show that adhesion modulation is favoured on PNIPAM brushes grafted at low surface densities [98, 99], while high density PNIPAM brushes are anti-adhesive, irrespective of the temperature [99]. However, PNIPAM brushes having high grafting densities, when properly patterned, have been shown to thermally control cell detachment [99] as illustrated in figure 2.16. This has led to the first qualitative example of single cell actuation using PNIPAM swelling. This could be further exploited to study adhesion in single cell assays.

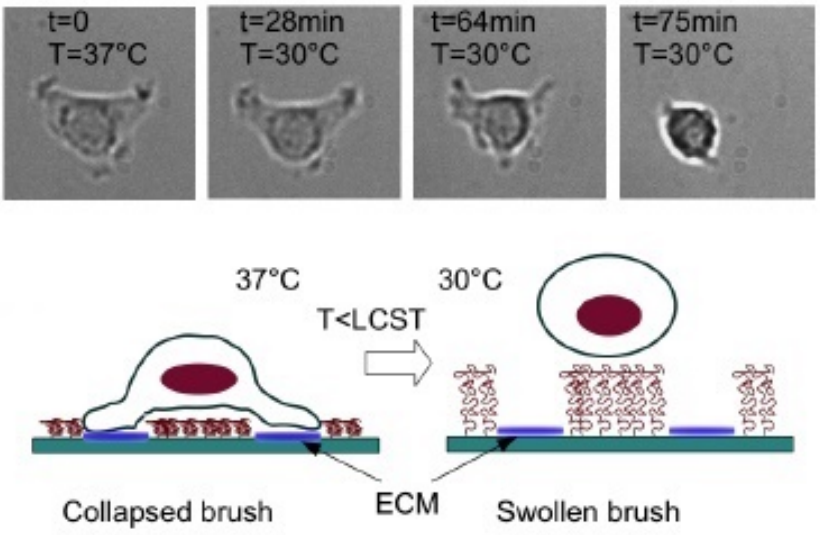

Figure 2.16: Thermally induced single cell detachment. (Up) sequence showing cell initially adhered on a V-shaped pattern and detaching upon lowering the substrate temperature. (Down) scheme of cell detachment by brush swelling. Adapted from [99]

The reversibility of PNIPAM transition has been studied to a wide extent [100, 101]. However, its reversible cell adhesive/non-adhesive properties in complex. PNIPAM based substrates have been used to show thermo-reversible cell adhesive/detachment events of proteins and cells. But some cases report partial cycling of cell adhesion/detachment. Incomplete reversibility affects the useful lifetime of many applications. Several reports have found incomplete protein removal upon cell lifting which needs better addressal. Moreover, these substrates do not allow for straight-forward spatial control of adhesion, because localized cooling or heating of the substrate is technically challenging. Temperature changes are usually applied at the macroscopic scale and thus affect adhesive state of the entire cell population on the substrate.

Light responsive Responsive Polymers Photo-responsive polymers are another interesting category of stimuli-responsive systems that allow fully reversible responses

when irradiated by a light source. Light represents an attractive signal because it triggers these switches without changing solution conditions [102]. Using light should allow for both localized and temporal control of cell adhesion and thus to achieve dynamic control of cell shape, adhesion and migration for single cell assays.

An attractive way for creating a smart surface involves polymers that have side chains functionalized with chromophores. Various kinds of polymers which contain pendant photochromic groups have been reported to change their conformation reversibly by photoirradiation in solution. Within these polymeric systems, azobenzene and spiropyran containing polymers are the most widely used [103, 104].

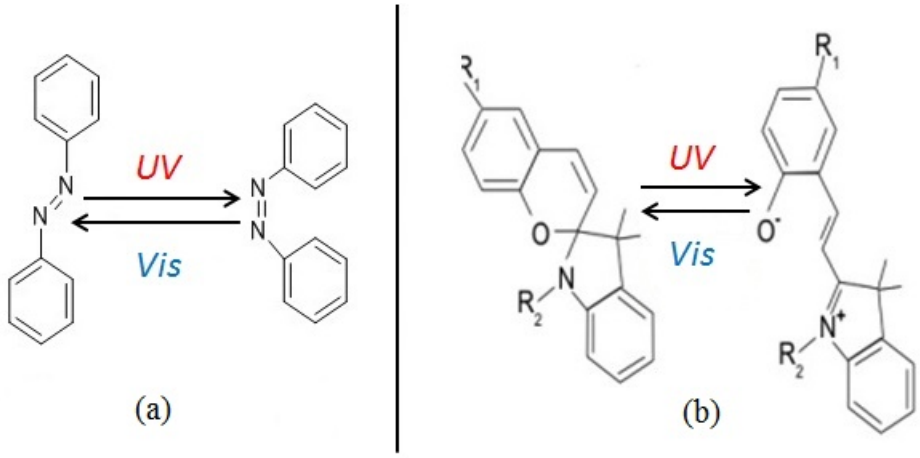

Figure 2.17: Isomerization of chromophores comprising (a) the azobenzene moieties and (b) spiropyran having light induced transformation. Conversion is achieved with UV and visible light.

For azobenzene modified derivatives, the inter-conversion between low energy trans and higher energy cis isomeric states can be achieved by a photo-chemical response. the trans form can be converted to the cis form using an appropriate wavelength of light. A different wavelength can be used to convert the molecule back to the trans form. Spiropyran isomerizes by UV illumination from the more hydrophobic spiro form to the polar, hydrophilic zwitterionic merocyanin form, while reversible isomerization can be achieved by visible light. The switching properties of polymers based on these light induced derivatives have been used in data storage, optical devices, and liquid crystalline displays [105, 106].

Photosensitive systems have been applied in biomolecular research. However, the use of photosensitive macro-molecules to control the adsorption and desorption of biomolecules at interfaces has been less studied. Taking advantage of photo-isomerization, Auernheimer *et al* [107] reported the control of cell adhesion properties on RGD-functionalized surfaces. Edahiro *et al* designed coatings of PNIPAM bearing photosensitive spiropyran lateral groups [108] on which cell adhesive property could be significantly changed by regional photoirradiation: cells adhered onto PNIPAM based responsive surfaces at temperatures around 37°C (figure 2.18(A)). After UV irradiation and low temperature washing, cells remained adhered only on the UV irradiated regions (inside of the yellow box) (figure 2.18(B)). It was observed that cell adhesion was increased by UV irradiation

and that shining visible light on the surface could then reset such a UV-enhancement of cell adhesion. This study provided the first proof of principle for reversible adhesion switching using photo-responsive polymers.

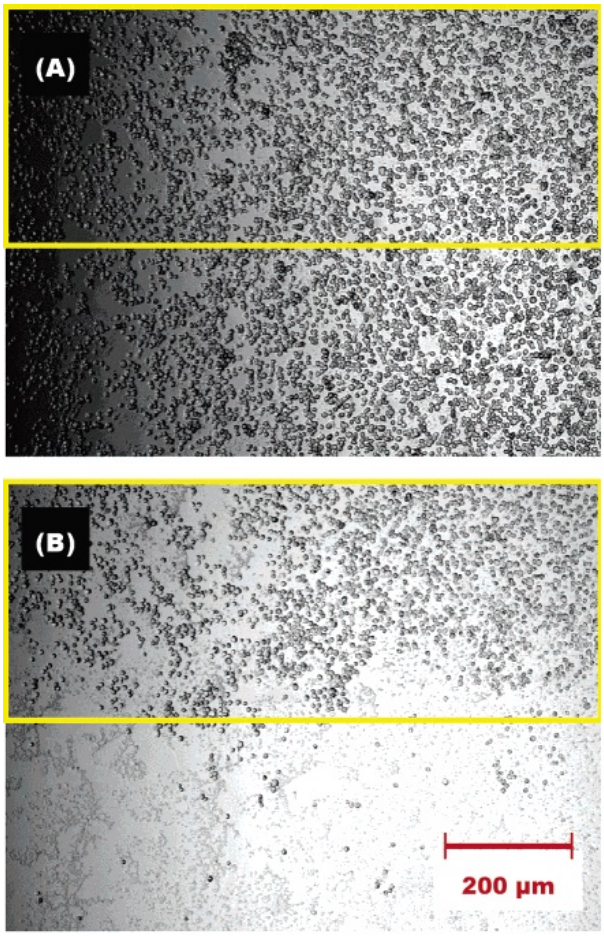

Figure 2.18: Microscopic images of photoresponsive culture surface (A) before and (B) after regional UV irradiation followed by low temperature washing [108] Images in the yellow box show the UV irradiated regions.

However, many issues were raised in this work:

- The mechanisms underlying the observed UV enhancement of adhesion remained unclear at this point. UV irradiation induced transformation of non-polar spiropyran groups into their polar form thereby making the surface hydrophilic. This was counter-intuitive to what is normally expected for cellular attachment that requires a hydrophobic surface.
- Adhesion control at the single cell level was not demonstrated.
- The reversible and dynamic cell attachment was dependent on the polymer composition which was poorly controlled.
- Cell de-adhesion after irradiation was observed only after cooling the surface below the PNIPAM LCST.

The current observations strongly suggested that polymer composition was far from being optimal, and that mechanical actuation associated with the polymer conformational

change could be exploited only upon using the temperature response. This calls for in-depth studies aiming at understanding the light induced reversible transformation from cell adhesive to cell repulsive surfaces.

Dual Responsive polymers Pioneering works led by Irie *et al* illustrated the design strategy for photo-thermo responsive polymers having pendant azobenzene groups [109]. Polymer composition was varied to observe light induced reversible switching of polymeric phase transitions. Work led by Kröger *et al* [110] showed the dependence of polymeric transitions on the composition of the polymer as well as on the degree of isomerisation. Copolymers based on N,N-Dimethylacrylamide (DMA) and azobenzene-based chromophores have shown their UV-visible phase transitions occuring within a temperature range of 40-45°C [111] (figure 2.19). DMA-azobenzene based copolymers were used to switch enzymatic activity at temperatures around 40°C [112]. The LCSTs were observed to depend on the molar fraction of the photo-sensitive monomer and could be finely tuned by varying the ratio. This photo-induced shift of polymer LCST, and thus of its conformation, forms the basic mechanism that is required here to exploit for cell adhesion control.

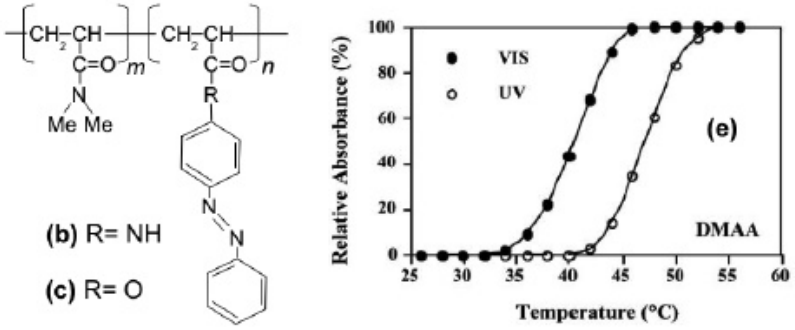

Figure 2.19: P(DMA-co-AZAA/AZAAm) and turbidity measurement of a solution of P(DMA-co-AZAA) as a function of temperature [111].

2.8 Aims of the present work

Up to now, scientific research has put a lot of emphasis on understanding the reversible control of cellular adhesive interactions using advanced functional surfaces in order to properly address biological questions and applications. The knowledge and skill acquired in tissue engineering and material science has considerably grown over the past years. Smartly patterned culture substrates are choice candidates to address such issues and represent the next generation of tools that can help to increase the understanding of cell adhesion dynamics. However, attempts to combine the various techniques and material science strategies to create functional substrates are still scarce.

Combining cell patterning with the functionalities of stimuli responsive substrates to probe the attachment and release of cells have been very recent. Still, such possibilities largely remain unexplored. Also, the rational design is often hampered by the lack of

detailed understanding of cell/surface interactions in the presence of functional films used to alter/control the surface properties. It is very recent that mechanisms have been proposed and theoretically modeled to explain cell adhesion modulation in the presence of thermoresponsive polymer layers. The current state of the art raises important questions concerning how to efficiently address dynamic cell adhesion studies at single cell level using the new class of substrates. From what is shown so far in the field on cell-surface adhesion, there are several aspects that require in depth analysis:

- Theoretical works highlight the fact that cell adhesion modulation depends on the brush architecture and its conformation. It is therefore important to understand quantitatively how changes in a brush structure and molecular parameters affect its performance.
- To control and understand the spatial and temporal cell adhesive interactions, need arises for the synthesis of photo-thermo responsive polymers whose molecular composition can be controlled in order to display switching properties under physiological conditions.

The present study initiates on original strategy aiming at designing a new class of stimuli responsive polymers that exhibit tunable adhesive properties suitable for cell adhesion studies. In parallel, efficient tools are implemented to probe the conformational change of macromolecules grafted onto the surface in order to better characterize the effects of molecular parameters on the brush structure and properties.

Surface grafting and patterning of stimuli responsive brushes The control of cellular adhesion requires proper design of brush architectures. This requires designing polymer brushes through well controlled synthesis protocols. Chapter 2 introduces polymer brushes and discusses efficient and convenient mechanisms for growing stimuli-responsive polymer brushes. Atom Transfer Radical Polymerization (ATRP) and Activators Regenerated by electron Transfer (ARGET) ATRP modes are investigated with emphasis on PNIPAM. Well-defined PNIPAM based patterned surfaces are fabricated using a UV ablation technique. Patterned PNIPAM substrates are used in particular to design protein micropattern transfer onto polyacrylamide hydrogels aimed at single cell adhesion studies.

Thermophysics of PNIPAM brushes The rational design of brushes calls for an accurate determination of the surface properties of the brushes, and for the quantification of the associated conformational changes. Chapter 3 describes the complete instrumental set up and analysis involved in designing a real-time spectroscopic Reflection Interference Contrast Microscopy (RICM) tool. The important aspects dealing with RICM studies include the validation of tools for characterizing the collapse and swelling of the polymer brushes and quantitative information about the changes of the physical properties of PNIPAM brushes across the polymeric transition temperature. The instrumental study investigates the influence of parameters such as grafting densities, and chain length on the properties of the brush. It supports the theoretical prediction for the existence of a local phase separation mechanisms that governs the changes taking place along the brush thickness as a function of temperature.

Polymer synthesis Synthesis of dually responsible polymers with tunable reversible properties is required for dynamic cell adhesion studies. Chapter 4 deals with the synthesis and characterization of dually responsive polymers based on NIPAM. Inspired by previous works on responsive polymer synthesis, bulk synthesis of photo-thermo-responsive polymers is carried out. Ter-polymers are synthesized based on a main monomer (a thermo-sensitive homopolymer), and a monomer bearing a photo-sensitive group (inducing photo-responsive nature). The synthesis of the copolymers were performed via free radical polymerization, and bulk ATRP. The composition of monomeric entities are varied in order to design polymers which ensure efficient conformational switching at 37°C, close to the physiological working environment of cells.

Bibliography

[1] Jeremy M Berg, John L Tymoczko, and Stryer Lubert, *Biochemistry. 5th edition*, W H Freeman New York (2002).

[2] C Zhu, G Bao, and N Wang, "Cell mechanics: Mechanical response, cell adhesion, and molecular deformation", *Annual Review Of Biomedical Engineering* **2**, pp. 189–226 (2000).

[3] Margaret Gardel and Ulrich Schwarz, "Cell-substrate interactions-Preface", *Journal Of Physics-Condensed Matter* **22**(19) (2010).

[4] Erich Sackmann, "Biophysics-How cells feel the force", *Nature Physics* **6**(6), pp. 407–408 (2010).

[5] BM Gumbiner, "Cell adhesion: The molecular basis of tissue architecture and morphogenesis", *Cell* **84**(3), pp. 345–357 (1996).

[6] KM Yamada and B Geiger, "Molecular interactions in cell adhesion complexes", *Current Opinion In Cell Biology* **9**(1), pp. 76–85 (1997).

[7] KA Beningo, M Dembo, I Kaverina, JV Small, and YL Wang, "Nascent focal adhesions are responsible for the generation of strong propulsive forces in migrating fibroblasts", *Journal Of Cell Biology* **153**(4), pp. 881–887 (2001).

[8] A De Arcangelis and E Georges-Labouesse, "Integrin and ECM functions: roles in vertebrate development. (vol 16, pg 389, 2000)", *Trends In Genetics* **16**(12), pp. 536 (2000).

[9] EHJ Danen and A Sonnenberg, "Integrins in regulation of tissue development and function (vol 200, pg 471, 2003)", *Journal Of Pathology* **201**(4), pp. 632–641 (2003).

[10] Kim S. Midwood, Yong Mao, Henry C. Hsia, Leyla V. Valenick, and Jean E. Schwarzbauer, "Modulation of cell-fibronectin matrix interactions during tissue repair", *Journal Of Investigative Dermatology Symposium Proceedings* **11**(1), pp. 73–78 (2006).

[11] LA Lasky, MS Singer, D Dowbenko, Y Imai, WJ Henzel, C Grimley, C Fennie, N Gillett, SR Watson, and SD Rosen, "An endothelial ligand for l-selectin is a novel mucin-like molecule", *Cell* **69**(6), pp. 927–938 (1992).

[12] H Perinpanayagam, R Zaharias, C Stanford, R Brand, J Keller, and G Schneider, "Early cell adhesion events differ between osteoporotic and non-osteoporotic osteoblasts", *Journal Of Orthopaedic Research* **19**(6), pp. 993–1000 (2001).

[13] CN Serhan and J Savill, "Resolution of inflammation: The beginning programs the end", *Nature Immunology* **6**(12), pp. 1191–1197 (2005).

[14] AD Bershadsky, NQ Balaban, and B Geiger, "Adhesion-dependent cell mechanosensitivity", *Annual Review Of Cell And Developmental Biology* **19**, pp. 677–695 (2003).

[15] Amelia Ahmad Khalili and Mohd Ridzuan Ahmad, "A review of cell adhesion studies for biomedical and biological applications", *International Journal Of Molecular Sciences* **16**(8), pp. 18149–18184 (2015).

[16] William R. Thompson, Clinton T. Rubin, and Janet Rubin, "Mechanical regulation of signaling pathways in bone", *Gene* **503**(2), pp. 179–193 (2012).

[17] GF Oster, JD Murray, and AK Harris, "Mechanical aspects of mesenchymal morphogenesis", *Journal Of Embryology And Experimental Morphology* **78**(DEC), pp. 83–125 (1983).

[18] CS Chen, M Mrksich, S Huang, GM Whitesides, and DE Ingber, "Geometric control of cell life and death", *Science* **276**(5317), pp. 1425–1428 (1997).

[19] Eileen Puklin-Faucher and Michael P. Sheetz, "The mechanical integrin cycle", *Journal Of Cell Science* **122**(2), pp. 179–186 (2009).

[20] A Folch and M Toner, "Microengineering of cellular interactions", *Annual Review Of Biomedical Engineering* **2**, pp. 227+ (2000).

[21] Milan Mrksich, "What can surface chemistry do for cell biology?", *Current Opinion in Chemical Biology* **6**(6), pp. 794 – 797 (2002).

[22] H Shin, S Jo, and AG Mikos, "Biomimetic materials for tissue engineering", *Biomaterials* **24**(24), pp. 4353–4364 (2003).

[23] Joseph Yang, Masayuki Yamato, Tatsuya Shimizu, Hidekazu Sekine, Kazuo Ohashi, Masato Kanzaki, Takeshi Ohki, Kohji Nishida, and Teruo Okano, "Reconstruction of functional tissues with cell sheet engineering", *Biomaterials* **28**(34), pp. 5033–5043 (2007).

[24] Jun Nakanishi, Tohru Takarada, Kazuo Yamaguchi, and Mizuo Maeda, "Recent advances in cell micropatterning techniques for bioanalytical and biomedical sciences", *Analytical Sciences* **24**(1, SI), pp. 67–72 (2008).

[25] D Falconnet, G Csucs, HM Grandin, and M Textor, "Surface engineering approaches to micropattern surfaces for cell-based assays", *Biomaterials* **27**(16), pp. 3044–3063 (2006).

[26] MJ Paszek, N Zahir, KR Johnson, JN Lakins, GI Rozenberg, A Gefen, CA Reinhart-King, SS Margulies, M Dembo, D Boettiger, DA Hammer, and VM Weaver, "Tensional homeostasis and the malignant phenotype", *Cancer Cell* **8**(3), pp. 241–254 (2005).

[27] MM Stevens and JH George, "Exploring and engineering the cell surface interface", *Science* **310**(5751), pp. 1135–1138 (2005).

[28] Y Tsuda, A Kikuchi, M Yamato, A Nakao, Y Sakurai, M Umezu, and T Okano, "The use of patterned dual thermoresponsive surfaces for the collective recovery as co-cultured cell sheets", *Biomaterials* **26**(14), pp. 1885–1893 (2005).

[29] JP Vacanti and R Langer, "Tissue engineering: the design and fabrication of living replacement devices for surgical reconstruction and transplantation", *Lancet* **354**(1), pp. SI32–SI34 (1999).

[30] XH Liu and PX Ma, "Polymeric scaffolds for bone tissue engineering", *Annals Of Biomedical Engineering* **32**(3), pp. 477–486 (2004).

[31] Peter X. Ma, "Scaffolds for tissue fabrication", *Materials Today* **7**(5), pp. 30–40 (2004).

[32] Dekel Dado and Shulamit Levenberg, "Cell-scaffold mechanical interplay within engineered tissue", *Seminars In Cell & Developmental Biology* **20**(6), pp. 656–664 (2009).

[33] Peter X. Ma, "Biomimetic materials for tissue engineering", *Advanced Drug Delivery Reviews* **60**(2), pp. 184–198 (2008).

[34] Fergal J. O'Brien, "Biomaterials & scaffolds for tissue engineering", *Materials Today* **14**(3), pp. 88–95 (2011).

[35] Taek Gyoung Kim, Heungsoo Shin, and Dong Woo Lim, "Biomimetic Scaffolds for Tissue Engineering", *Advanced Functional Materials* **22**(12), pp. 2446–2468 (2012).

[36] KC Dee, TT Andersen, and R Bizios, "Osteoblast population migration characteristics on substrates modified with immobilized adhesive peptides", *Biomaterials* **20**(3), pp. 221–227 (1999).

[37] A Rezania, R Johnson, AR Lefkow, and KE Healy, "Bioactivation of metal oxide surfaces. 1. Surface characterization and cell response", *Langmuir* **15**(20), pp. 6931–6939 (1999).

[38] SJ Xiao, M Textor, ND Spencer, and H Sigrist, "Covalent attachment of cell-adhesive, (Arg-Gly-Asp)-containing peptides to titanium surfaces", *Langmuir* **14**(19), pp. 5507–5516 (1998).

[39] RA Stile and KE Healy, "Thermo-responsive peptide-modified hydrogels for tissue regeneration", *Biomacromolecules* **2**(1), pp. 185–194 (2001).

[40] IV Yannas, E Lee, DP Orgill, EM Skrabut, and GF Murphy, "Synthesis and characterization of a model extracellular-matrix that induces partial regeneration of adult mammalian skin", *Proceedings Of The National Academy Of Sciences Of The United States Of America* **86**(3), pp. 933–937 (1989).

[41] A Atala, SB Bauer, S Soker, JJ Yoo, and AB Retik, "Tissue-engineered autologous bladders for patients needing cystoplasty", *Lancet* **367**(9518), pp. 1241–1246 (2006).

[42] PH Warnke, ING Springer, J Wiltfang, Y Acil, H Eufinger, M Wehmoller, PAJ Russo, H Bolte, E Sherry, E Behrens, and H Terheyden, "Growth and transplantation of a custom vascularised bone graft in a man", *Lancet* **364**(9436), pp. 766–770 (2004).

[43] Daisuke Sasaki, Tatsuya Shimizu, Shinako Masuda, Jun Kobayashi, Kazuyoshi Itoga, Yukiko Tsuda, Jun K. Yamashita, Masayuki Yamato, and Teruo Okano, "Mass preparation of size-controlled mouse embryonic stem cell aggregates and induction of cardiac differentiation by cell patterning method", *Biomaterials* **30**(26), pp. 4384–4389 (2009).

[44] R McBeath, DM Pirone, CM Nelson, K Bhadriraju, and CS Chen, "Cell shape, cytoskeletal tension, and RhoA regulate stem cell lineage commitment", *Developmental Cell* **6**(4), pp. 483–495 (2004).

[45] Manuel Thery, Victor Racine, Matthieu Piel, Anne Pepin, Ariane Dimitrov, Yong Chen, Jean-Baptiste Sibarita, and Michel Bornens, "Anisotropy of cell adhesive microenvironment governs cell internal organization and orientation of polarity", *Proceedings Of The National Academy Of Sciences Of The United States Of America* **103**(52), pp. 19771–19776 (2006).

[46] Julien E. Gautrot, Britta Trappmann, Fabian Oceguera-Yanez, John Connelly, Ximin He, Fiona M. Watt, and Wilhelm T. S. Huck, "Exploiting the superior protein resistance of polymer brushes to control single cell adhesion and polarisation at the micron scale", *Biomaterials* **31**(18), pp. 5030–5041 (2010).

[47] Manuel Thery, "Micropatterning as a tool to decipher cell morphogenesis and functions", *Journal Of Cell Science* **123**(24), pp. 4201–4213 (2010).

[48] CS Chen, M Mrksich, S Huang, GM Whitesides, and DE Ingber, "Geometric control of cell life and death", *Science* **276**(5317), pp. 1425–1428 (1997).

[49] M Thery, A Pepin, E Dressaire, Y Chen, and M Bornens, "Cell distribution of stress fibres in response to the geometry of the adhesive environment", *Cell Motility And The Cytoskeleton* **63**(6), pp. 341–355 (2006).

[50] RD Tilton, CR Robertson, and AP Gast, "Manipulation Of Hydrophobic Interactions In Protein Adsorption", *Langmuir* **7**(11), pp. 2710–2718 (1991).

[51] AN Parikh, DL Allara, IB Azouz, and F Rondelez, "An intrinsic relationship between molecular-structure in self-assembled n-alkylsiloxane monolayers and deposition temperature", *Journal Of Physical Chemistry* **98**(31), pp. 7577–7590 (1994).

[52] ME Mcgovern, KMR Kallury, and M Thompson, "Role of solvent on the silanization of glass with octadecyltrichlorosilane", *Langmuir* **10**(10), pp. 3607–3614 (1994).

[53] M Mrksich and GM Whitesides, "Using self-assembled monolayers to understand the interactions of man-made surfaces with proteins and cells", *Annual Review Of Biophysics And Biomolecular Structure* **25**, pp. 55–78 (1996).

[54] WR Gombotz, W Guanghui, TA Horbett, and AS Hoffman, "Protein adsorption to poly(ethylene oxide) surfaces", *Journal Of Biomedical Materials Research* **25**(12), pp. 1547–1562 (1991).

[55] Harris JM, *poly(ethyleneglycol)chemistry: Biotechnical and biomedical applications*, Plenum New York (1992).

[56] GP Lopez, MW Albers, SL Schreiber, R Carroll, E Peralta, and GM Whitesides, "Convenient methods for patterning the adhesion of mammalian-cells to surfaces using self-assembled monolayers of alkanethiolates on gold", *Journal Of The American Chemical Society* **115**(13), pp. 5877–5878 (1993).

[57] M Mrksich and GM Whitesides, "Patterning self-assembled monolayers using microcontact printing - a new technology for biosensors", *Trends In Biotechnology* **13**(6), pp. 228–235 (1995).

[58] V Hlady and J Buijs, "Protein adsorption on solid surfaces", *Current Opinion In Biotechnology* **7**(1), pp. 72–77 (1996).

[59] K Wadu-Mesthrige, NA Amro, and GY Liu, "Immobilization of proteins on self-assembled monolayers", *Scanning* **22**(6), pp. 380–388 (2000).

[60] XY Jiang, R Ferrigno, M Mrksich, and GM Whitesides, "Electrochemical desorption of self-assembled monolayers noninvasively releases patterned cells from geometrical confinements", *Journal Of The American Chemical Society* **125**(9), pp. 2366–2367 (2003).

[61] Chuan Zhao, Irene Witte, and Gunther Wittstock, "Switching on cell adhesion with microelectrodes", *Angewandte Chemie-International Edition* **45**(33), pp. 5469–5471 (2006).

[62] Jun Nakanishi, Yukiko Kikuchi, Tohru Takarada, Hidekazu Nakayama, Kazuo Yamaguchi, and Mizuo Maeda, "Spatiotemporal control of cell adhesion on a self-assembled monolayer having a photocleavable protecting group", *Analytica Chimica Acta* **578**(1), pp. 100–104 (2006).

[63] Jun Nakanishi, Yukiko Kikuchi, Satoshi Inoue, Kazuo Yamaguchi, Tohru Takarada, and Mizuo Maeda, "Spatiotemporal control of migration of single cells on a photoactivatable cell microarray", *Journal Of The American Chemical Society* **129**(21), pp. 6694+ (2007).

[64] Timothee Vignaud, Remi Galland, Qingzong Tseng, Laurent Blanchoin, Julien Colombelli, and Manuel Thery, "Reprogramming cell shape with laser nano-patterning", *Journal Of Cell Science* **125**(9), pp. 2134–2140 (2012).

[65] N Delorme, JF Bardeau, A Bulou, and F Poncin-Epaillard, "Azobenzene-containing monolayer with photoswitchable wettability", *Langmuir* **21**(26), pp. 12278–12282 (2005).

[66] J Wang, M Jiang, and B Mukherjee, "On-demand electrochemical release of DNA from gold surfaces", *Bioelectrochemistry* **52**(1), pp. 111–114 (2000).

[67] X Zhu, J De Graaf, FM Winnik, and D Leckband, "Tuning the interfacial properties of grafted chains with a pH switch", *Langmuir* **20**(4), pp. 1459–1465 (2004).

[68] M Panayiotou and R Freitag, "Influence of the synthesis conditions and ionic additives on the swelling behaviour of thermo-responsive polyalkylacrylamide hydrogels", *Polymer* **46**(18), pp. 6777–6785 (2005).

[69] Sally L. Gras, Tanveer Mahmud, Gary Rosengarten, Arnan Mitchell, and Kourosh Kalantar-Zadeh, "Intelligent control of surface hydrophobicity", *ChemPhysChem* **8**(14), pp. 2036–2050 (2007).

[70] G. Lopez, A. Chilkoti, P. Atanassov, and V.R. Goparaju, "Stimuli-responsive hybrid materials containing molecular actuators and their applications" (2004), US Patent 6,755,621.

[71] Martin A. Cole, Nicolas H. Voelcker, Helmut Thissen, and Hans J. Griesser, "Stimuli-responsive interfaces and systems for the control of protein-surface and cell-surface interactions", *Biomaterials* **30**(9), pp. 1827–1850 (2009).

[72] Gosuke Hayashi, Masaki Hagihara, Chikara Dohno, and Kazuhiko Nakatani, "Photoregulation of a peptide-RNA interaction on a gold surface", *Journal Of The American Chemical Society* **129**(28), pp. 8678+ (2007).

[73] Paula M. Mendes, "Stimuli-responsive surfaces for bio-applications", *Chemical Society Reviews* **37**(11), pp. 2512–2529 (2008).

[74] Jort Robertus, Wesley R. Browne, and Ben L. Feringa, "Dynamic control over cell adhesive properties using molecular-based surface engineering strategies", *Chemical Society Reviews* **39**(1), pp. 354–378 (2010).

[75] He Zhu, Jun Yan, and Alexander Revzin, "Catch and release cell sorting: Electrochemical desorption of T-cells from antibody-modified microelectrodes", *Colloids And Surfaces B-Biointerfaces* **64**(2), pp. 260–268 (2008).

[76] Eugene W. L. Chan and Muhammad N. Yousaf, "Immobilization of ligands with precise control of density to electroactive surfaces", *Journal Of The American Chemical Society* **128**(48), pp. 15542–15546 (2006).

[77] WS Yeo, MN Yousaf, and M Mrksich, "Dynamic interfaces between cells and surfaces: Electroactive substrates that sequentially release and attach cells", *Journal Of The American Chemical Society* **125**(49), pp. 14994–14995 (2003).

[78] Chuan Zhao, Irene Witte, and Gunther Wittstock, "Switching on cell adhesion with microelectrodes", *Angewandte Chemie-International Edition* **45**(33), pp. 5469–5471 (2006).

[79] S Balamurugan, LK Ista, J Yan, GP Lopez, J Fick, M Himmelhaus, and M Grunze, "Reversible protein adsorption and bioadhesion on monolayers terminated with mixtures of oligo(ethylene glycol) and methyl groups", *Journal Of The American Chemical Society* **127**(42), pp. 14548–14549 (2005).

[80] J Nakanishi, Y Kikuchi, T Takarada, H Nakayama, K Yamaguchi, and M Maeda, "Photoactivation of a substrate for cell adhesion under standard fluorescence microscopes", *Journal Of The American Chemical Society* **126**(50), pp. 16314–16315 (2004).

[81] Dingbin Liu, Yunyan Xie, Huawu Shao, and Xingyu Jiang, "Using azobenzene-embedded self-assembled monolayers to photochemically control cell adhesion reversibly", *Angewandte Chemie-International Edition* **48**(24), pp. 4406–4408 (2009).

[82] Kashmiri L Mittal, K-W_ Lee, et al., *Polymer surfaces and interfaces: characterization, modification and application*, Vsp (1997).

[83] Donald L Wise, Gary E Wnek, Debra J Trantolo, Thomas M Cooper, and Joseph D Gresser, *Photonic Polymer Systems: Fundamentals: Methods, and Applications*, CRC Press (1998).

[84] Terje A Skotheim and John Reynolds, *Handbook of Conducting Polymers, 2 Volume Set*, CRC press (2007).

[85] Krzysztof Matyjaszewski, *Controlled/Living Radical Polymerization*, American Chemical Society (2000).

[86] Martin A Cole, Nicolas H Voelcker, Helmut Thissen, and Hans J Griesser, "Stimuli-responsive interfaces and systems for the control of protein–surface and cell–surface interactions", *Biomaterials* **30**(9), pp. 1827–1850 (2009).

[87] Peter Kingshott and Hans J. Griesser, "Surfaces that resist bioadhesion", *Current Opinion in Solid State and Materials Science* **4**(4), pp. 403 – 412 (1999).

[88] Carolina de las Heras Alarcon, Sivanand Pennadam, and Cameron Alexander, "Stimuli responsive polymers for biomedical applications", *Chem. Soc. Rev.* **34**, pp. 276–285 (2005).

[89] M. Heskins and J. E. Guillet, "Solution properties of poly(n-isopropylacrylamide)", *Journal of Macromolecular Science: Part A - Chemistry* **2**(8), pp. 1441–1455 (1968).

[90] Kenichi Nagase, Jun Kobayashi, and Teruo Okano, "Temperature-responsive intelligent interfaces for biomolecular separation and cell sheet engineering", *Journal of the Royal Society Interface* **6**(Suppl 3), pp. S293–S309 (2009).

[91] Kazuo Ohashi, Takashi Yokoyama, Masayuki Yamato, Hiroyuk Kuge, Hiromichi Kanehiro, Masahiro Tsutsumi, Toshihiro Amanuma, Hiroo Iwata, Josepha Yang, Teruo Okano, and Yoshiyuk Nakajima, "Engineering functional two- and three-dimensional liver systems in vivo using hepatic tissue sheets", *Nature medicine* **13**, pp. 880–885 (2007).

[92] Ai Kushida, Masayuki Yamato, Chie Konno, Akihiko Kikuchi, Yasuhisa Sakurai, and Teruo Okano, "Decrease in culture temperature releases monolayer endothelial cell sheets together with deposited fibronectin matrix from temperature-responsive culture surfaces", *Journal of Biomedical Materials Research* **45**(4), pp. 355–362 (1999).

[93] Heather E. Canavan, Xuanhong Cheng, Daniel J. Graham, Buddy D. Ratner, , and David G. Castner, "Surface characterization of the extracellular matrix remaining after cell detachment from a thermoresponsive polymer", *Langmuir* **21**(5), pp. 1949–1955 (2005).

[94] Noriko Yamada, Teruo Okano, Hideaki Sakai, Fumiko Karikusa, Yoshio Sawasaki, and Yasuhisa Sakurai, "Thermo-responsive polymeric surfaces; control of attachment and detachment of cultured cells", *Die Makromolekulare Chemie, Rapid Communications* **11**(11), pp. 571–576 (1990).

[95] Joseph Yang, Masayuki Yamato, Chinatsu Kohno, Ayako Nishimoto, Hidekazu Sekine, Fumio Fukai, and Teruo Okano, "Cell sheet engineering: Recreating tissues without biodegradable scaffolds", *Biomaterials* **26**(33), pp. 6415 – 6422 (2005).

[96] A. Halperin and M. Kroger, "Theoretical considerations on mechanisms of harvesting cells cultured on thermoresponsive polymer brushes", *Biomaterials* **33**(20), pp. 4975 – 4987 (2012).

[97] A. Halperin and M. Kröger, "Collapse of thermoresponsive brushes and the tuning of protein adsorption", *Macromolecules* **44**(17), pp. 6986–7005 (2011).

[98] Kenichi Nagase, Minami Watanabe, Akihiko Kikuchi, Masayuki Yamato, and Teruo Okano, "Thermo-responsive polymer brushes as intelligent biointerfaces: Preparation via atrp and characterization", *Macromolecular Bioscience* **11**(3), pp. 400–409 (2011).

[99] Kalpana Mandal, Martial Balland, and Lionel Bureau, "Thermoresponsive micropatterned substrates for single cell studies", *PLoS One* **7**(5), pp. e37548 (2012).

[100] David Cunliffe, Carolina de las Heras Alarcón, Vanes A Peters, James R. Smith, and Cameron Alexander, "Thermoresponsive surface-grafted poly(nisopropylacrylamide) copolymers: effect of phase transitions on protein and bacterial attachment", *Langmuir* **19**(7), pp. 2888–2899 (2003).

[101] Mahaveer D Kurkuri, Matthew R Nussio, Alec Deslandes, and Nicolas H Voelcker, "Thermosensitive copolymer coatings with enhanced wettability switching", *Langmuir* **24**(8), pp. 4238–4244 (2008).

[102] Tsuyoshi Shimoboji, Zhongli L Ding, Patrick S Stayton, and Allan S Hoffman, "Photoswitching of ligand association with a photoresponsive polymer-protein conjugate", *Bioconjugate chemistry* **13**(5), pp. 915–919 (2002).

[103] Anton Airinei, Nicusor Fifere, Mihaela Homocianu, Constantin Gaina, Viorica Gaina, and Bogdan C Simionescu, "Optical properties of some new azo photoisomerizable bismaleimide derivatives", *International journal of molecular sciences* **12**(9), pp. 6176–6193 (2011).

[104] Akon Higuchi, Ayu Hamamura, Yosuke Shindo, Hanako Kitamura, Boo Ok Yoon, Taisuke Mori, Taro Uyama, and Akihiro Umezawa, "Photon-modulated changes of cell attachments on poly (spiropyran-co-methyl methacrylate) membranes", *Biomacromolecules* **5**(5), pp. 1770–1774 (2004).

[105] Hong-Zhi Tang, Paul D Boyle, and Bruce M Novak, "Chiroptical switching polyguanidine synthesized by helix-sense-selective polymerization using [(r)-3, 3'-dibromo-2, 2'-binaphthoxy](di-tert-butoxy) titanium (iv) catalyst", *Journal of the American Chemical Society* **127**(7), pp. 2136–2142 (2005).

[106] Ben L Feringa, Richard A van Delden, Nagatoshi Koumura, and Edzard M Geertsema, "Chiroptical molecular switches", *Chemical Reviews* **100**(5), pp. 1789–1816 (2000).

[107] Jörg Auernheimer, Claudia Dahmen, Ulrich Hersel, Andreas Bausch, and Horst Kessler, "Photoswitched cell adhesion on surfaces with rgd peptides", *Journal of the American Chemical Society* **127**(46), pp. 16107–16110 (2005).

[108] Jun-ichi Edahiro, Kimio Sumaru, Yuichi Tada, Katsuhide Ohi, Toshiyuki Takagi, Mitsuyoshi Kameda, Toshio Shinbo, Toshiyuki Kanamori, and Yasuo Yoshimi, "In situ control of cell adhesion using photoresponsive culture surface", *Biomacromolecules* **6**(2), pp. 970–974 (2005).

[109] Masahiro Irie and Dawan Kungwatchakun, "Stimuli-responsive polymers. photostimulated reversible phase separation of aqueous solutions of poly (n-isopropylacrylamide) with pendant azobenzene groups.", *Proceedings of the Japan Academy, Series B* **68**(8), pp. 127–132 (1992).

[110] Rainer Kröger, Henning Menzel, and Manfred L Hallensleben, "Light controlled solubility change of polymers: Copolymers of n, n-dimethylacrylamide and 4-phenylazophenyl acrylate", *Macromolecular Chemistry and Physics* **195**(7), pp. 2291–2298 (1994).

[111] Tsuyoshi Shimoboji, Edmund Larenas, Tim Fowler, Samarth Kulkarni, Allan S Hoffman, and Patrick S Stayton, "Photoresponsive polymer–enzyme switches", *Proceedings of the National Academy of Sciences* **99**(26), pp. 16592–16596 (2002).

[112] Tsuyoshi Shimoboji, Edmund Larenas, Tim Fowler, Samarth Kulkarni, Allan S Hoffman, and Patrick S Stayton, "Photoresponsive polymer–enzyme switches", *Proceedings of the National Academy of Sciences* **99**(26), pp. 16592–16596 (2002).

Chapter 3

PNIPAM Brushes: Design and Patterning

3.1 Abstract

In the current chapter, I introduce the physics and chemistry concepts relevant to polymer brushes. I describe the synthesis protocols employed in my work to design PNIPAM brushes via Surface-Initiated Atom Transfer Radical Polymerization (ATRP) and its variant. This is followed by the results regarding the basic characterization of the obtained brushes and the control over their molecular brush parameters such as grafting density and chain length. Finally, I present a novel and versatile method to fabricate micropatterned PNIPAM brushes. Such patterned brushes are applied to transfer protein patterns onto the surface of polyacrylamide (PAA) based hydrogels for single-cell studies using traction force microscopy.

3.2 Introduction

3.2.1 Polymer brushes

The term polymer brush refers to a system in which individual macromolecules are attached close to each other by anchor points to a surface.

Depending on how individual chains are tethered onto the surface, they can adopt different conformations (figure 3.1) [1].

- If the distance between the anchor points is larger than the size of the polymeric chains, they do not interact with the neighboring molecules and remain unperturbed. In this case, if the interaction between the chains and the surface is weak, they appear to acquire a mushroom shaped conformation (figure 3.1(a)) where the chains are randomly coiled and attached to the surface through a stem. However, if the interaction of the chains with the surface is strong, they adsorb onto the surface and adopt a pancake like conformation (figure 3.1(b)).

- A completely different picture is obtained when the anchoring points are at very short distances from each other. In such a case, the excluded volume interactions

between neighboring chain segments force the chains to stretch away from the surface to form a brush like layer (figure 3.1(c)).

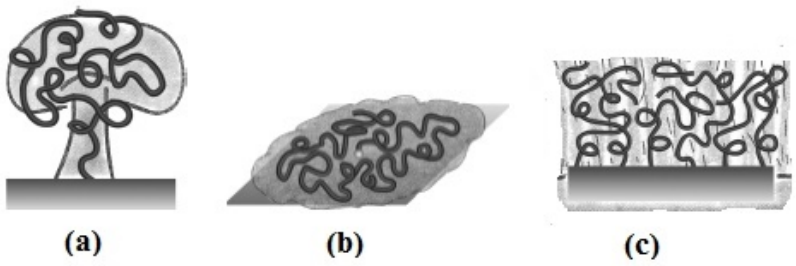

Figure 3.1: Terms (a) mushroom (b) pancake and (c) brush for the different types of conformations of surface attaches polymers. Images taken from [1]

The essential parameters of a polymer brush are the grafting density σ (the number of chains per unit area) and the polymerization index of the chains N (the number of monomer units per chain). When the size of the grafted polymer chains approaches the distance between the anchoring points, there occurs a transition from single coiled chain to the brush like architecture, which is controlled by the reduced tethering density Σ.

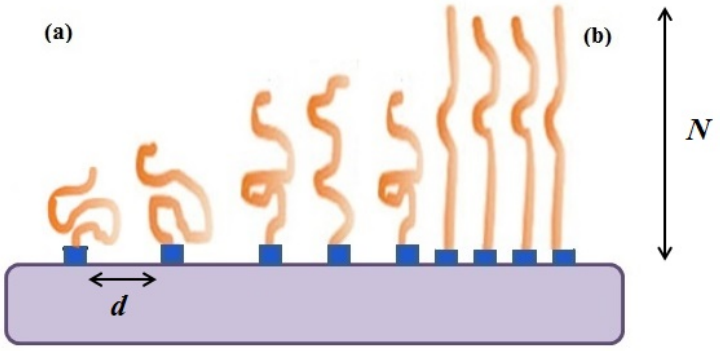

Figure 3.2: Schematic showing the crossover between the mushroom regime (a) and a brush regime (b). N is the chain polymerization index and $d = 1/\sqrt{\sigma}$ is the average distance between anchoring points. Images adapted from [2].

$$\Sigma = \sigma\pi(R_g^2) \tag{3.1}$$

where R_g is the radius of gyration of an unperturbed chain at prescribed experimental conditions of solvent and temperature. Σ describes the number of chains occupying the area that a free non-overlapping chain would occupy under same solvent and temperature conditions (figure 3.2).

The equilibrium height, h, of a brush immersed in a solvent can be computed from the free energy F of the chains, which contains two contributions. The interaction (or mixing) energy, F_{int}, accounts for the balance of monomer/solvent and monomer/monomer interactions. For a macromolecule in good solvent, F_{int} incorporates the so-called excluded volume interactions and accounts for the fact that a given chain segment occupies a volume that is inaccessible to others. Such a repulsive interaction tends to make the chain

"swell". For macromolecules bound to a surface at high concentrations, such a swelling is constrained both by surface-tethering and by neighboring chains and takes place preferentially in the direction perpendicular to the surface, resulting in a net stretching of the grafted macromolecules. This stretching, associated with a loss of configurational entropy, gives rise to an elastic contribution, F_{el}, to the free energy, which tends to restore the chains to their unperturbed, more isotropic state. While the exact form of F_{int} and F_{el} depends on the grafting density and degree of stretching of the chains [3], the equilibrium height of a brush can, on a general basis, be computed by minimizing the free energy $F = F_{int} + F_{el}$ with respect to h ($dF/dh = 0$). I provide in the next chapter a derivation of h as a function of the brush molecular parameters in the framework of a simple model that has been employed for data analysis. Independently of the modeling details, the following scaling relationship holds between h, N and σ for a brush in a good solvent:

$$h \propto N\sigma^{1/3} \tag{3.2}$$

3.2.2 Design strategies

Polymeric chains can be anchored onto a surface via physisorption or chemisorption processes. Physisorption allows attachment of pre-fabricated block co-polymers onto surfaces where one block (red component in figure 3.3(A)) acts as the anchor as it preferentially interacts with the surface whereas other blocks (blue component) offers weak affinity towards attachment. However, such type of anchoring suffers from limitations in terms of the stability and density of the polymeric assemblies.

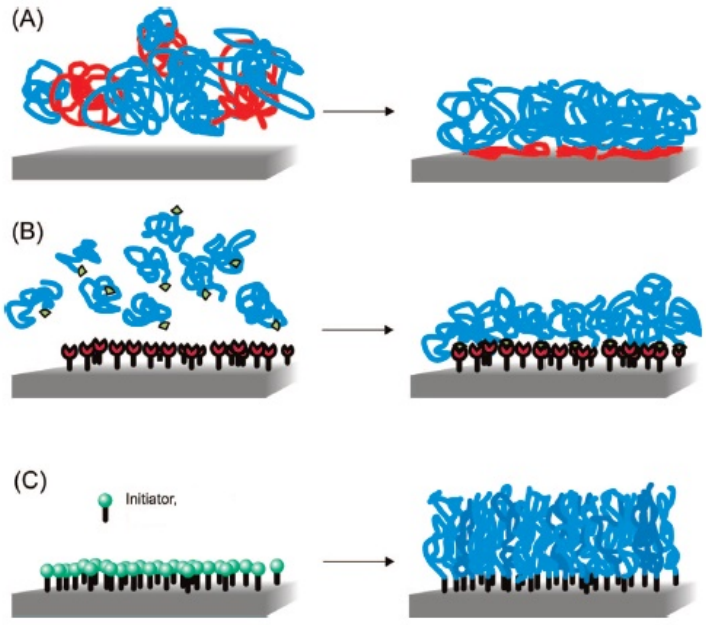

Figure 3.3: Synthesis strategies for the preparation of polymer brushes. (A) Physisorption of two-component polymers via preferential adsorption of the red blocks to the surface. (B) Chemisorption via reaction of end-functionalized polymers with complementary functional groups at the surface. (C) Polymer brushes grown via initiator grafted substrates. image source: [4].

Covalent linkage between the chains and the surface is achieved either by "grafting to" or "grafting from" technique. In the "grafting to" method, macromolecules are pre-formed and have a suitable end-functionalized group that binds to the surfaces to obtain the desired brush (figure 3.3(B)). Only a limited surface density of polymeric chains can be reached using this protocol, since the chains need to diffuse through the already formed polymer layer in order to react with the surface. Thus, this method is only able to generate brushes of low grafting densities which leads to low film thicknesses.

In order to overcome this limitation, a "grafting from" technique is utilized. This involves an *in situ* polymerization of monomers from the surface. The substrate is first modified with an initiator, followed by direct surface-initiated polymerization of the polymer. The density of the initiator can be varied at will. A densely packed arrangement of surface grafted polymers makes them adopt a brush like structure. (figure 3.3(C)). This protocol allows well defined polymer brushes having high and controlled grafting densities.

3.2.3 Chain growth protocols following the "grafting from" approach

Conventional radical polymerization has been employed to produce a large number of polymers [5]. However, the major drawback of this technique is related to the lack of control over the polymer architecture. Slow initiation, fast propagation and simultaneous termination produces polymers of high molecular weight and high polydispersities. Developments in the form of ionic polymerization protocols have allowed preparation of well defined polymers with controlled chain end functionalities [6]. Still, these methods can be used only for a narrow set of monomers which show undesirable side reactions due to the presence of functionalities.

Atom Transfer Radical polymerization

One of the most successful methods to grow polymer brushes with proper control over their structure and properties is Atom Transfer Radical Polymerization (ATRP) [7–9]. ATRP is an example of a reversible-deactivation radical polymerization. As the name implies, the atom transfer step is the key step in the reaction responsible for uniform polymer chain growth [10].

Mechanism of ATRP ATRP is controlled by an equilibrium between propagating radicals and dormant species, predominantly in the form of initiating alkyl halides (R-X) (figure 3.4). The dormant species react, with a rate constant of k_{act}, with the transition metal complexes in their lower oxidation state(M^n-Y/Ligand, with Y being a counter ion or another ligand) (figure 3.4), acting as activators. The active radical is formed by homolytic breakage of alkyl and halide bonds accompanied by halide coordinated metal complexes in their higher oxidation states (M^{n+1}-Y/Ligand). These act as deactivators that react with the radicals in the opposite way (k_{deact}) to re-form the dormant species and the activator [11]. The essential feature of ATRP [12–14] is the equilibrium between a low concentration of active propagating species and the larger number of dormant chains

via an inner sphere electron transfer process promoted through the catalyst complex [15]. In order to create a low concentration of propagating radicals, the deactivation rate should be higher than the activation rate. This shifts the equilibrium towards the dormant species.

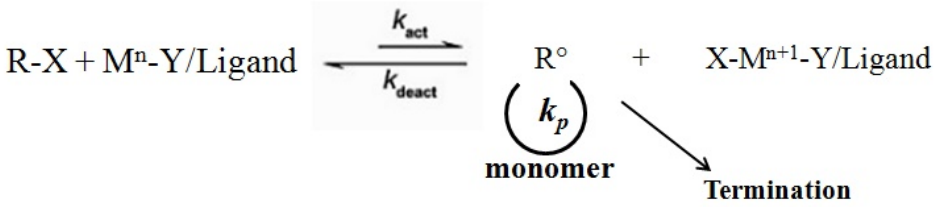

Figure 3.4: Schematic showing the mechanism of ATRP. The process occurs with rate constants of activation k_{act} and deactivation k_{deact}. Images taken from [10]

The ATRP equilibrium The ATRP mechanism consists of initiation and propagation processes that can be expressed as follows (explained in terms of a copper based catalyst system) [16].

Initiation

$$R - X + Cu^{I}X/Ligand \leftrightarrow^{k_{eq}} R^{\bullet} + XCu(II)X/Ligand \tag{3.3}$$

$$R^{\bullet} + Monomer(M) \rightarrow^{k_p} P_1^{\bullet} \tag{3.4}$$

Propagation

$$P_n - X + Cu^{I}X/Ligand \leftrightarrow^{k_{eq}} P_n^{\bullet} + XCu(II)X/Ligand \tag{3.5}$$

$$P_n^{\bullet} + Monomer(M) \rightarrow^{k_p} P_{n+1}^{\bullet} \tag{3.6}$$

Termination

$$P_n^{\bullet} + P_m^{\bullet} \rightarrow^{k_t} P_{n+m} \tag{3.7}$$

Termination occurs in ATRP mainly through radical coupling and disproportionation (conversion of Cu I into Cu II and Cu). However, ATRP minimizes radical-radical coupling at the surface because of site-specific initiation and the ATRP equilibrium, which keeps the concentration of active species or propagating radicals sufficiently low throughout the polymerization, thereby suppressing the termination. Thus, a very small percentage of polymer chains undergo termination in ATRP.

The rate of ATRP The rate of the polymerization reaction can be derived by omitting the termination step (insignificant due to radical effects).

$$R_p = k_p k_{ATRP} \frac{[P_n - X][Cu(I])[M]}{[Cu(II)X]} \tag{3.8}$$

where

$$k_{ATRP} = \frac{[P^{\bullet}][Cu(II)X]}{[Cu(I][P_n - X]} \tag{3.9}$$

$[P_n - X] and [M]$ are the concentration of the alkyl halides and the feed monomer. The overall rate is highly dependent on the redox potential of metal complexes.

Results from kinetic studies of ATRP using solubilized forms of the catalyst species indicate that the rate of polymerization is first order with respect to monomer, alkyl halide (initiator) and Copper(I) complex concentration [17].

Role of components and reaction conditions in ATRP

- Alkyl halide: The alkyl halide determines the number of initiated chains. It must rapidly and selectively migrate between the growing chain and the transition-metal complex. So far, bromine and chlorine are the most efficient candidates used. [16,17].

- Transition metal complexes: The most important role of a catalyst complex is to maintain the position of the atom transfer equilibrium and the dynamics of exchange between the dormant and active species. For efficient functioning, the metal complex must have an accessible one electron redox couple to promote the electron transfer, and upon a one-electron transfer, the metal should be able to accommodate a new ligand. Copper is the most widely used metal catalyst due to its versatility in ATRP. Apart from copper, other metals such as iron, ruthenium, and molybdenum have been used as effective catalysts [18].

- Ligands: Ligands help to stabilize the metal complexes in the solvent, control the metal selectivity by electronic and steric effects, and by doing so, they affect the redox chemistry of the final metal complex. Copper is usually seen to be coupled with bidentate (such as 2-2'bipyridine), tridentate (such as pentamethyldiethylenetriamine (PMDETA)), and tetradentate ligands (such as tris(2-(diethylamino)ethyl)amine, (ME_6-TREN)) [19] (figure 3.5).

- Monomers : ATRP has been successfully used for the polymerization of various acrylamide and acrylate based monomers [20–22]. In ATRP, one set of conditions are not generally applied to every monomer class. A unique combination of initiator, metal complex, ligand, deactivators, solvent, reaction time are employed for the ATRP of each particular monomer.

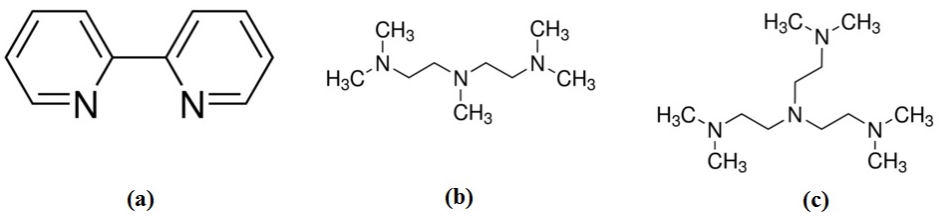

Figure 3.5: Schematic showing (a) the bi-dentate 2-2'bipyridine, (b) tri-dentate pentamethyl-diethylene-triamine(PMDETA)) and (c) tetradentate tris(2-(diethylamino)ethyl)amine (ME_6-TREN) ligands.

An ATRP variant

One limitation of ATRP method is that special handling is required to remove all oxygen and oxidants from the reaction systems prior and during polymerization reaction. This is done to avoid the oxidation of the catalyst complex, thereby maintaining the supply of active radicals for polymerization. Additionally, the presence of residual amounts of metal catalyst in polymerized systems raises concerns over their use in various applications [4]. A more attractive approach in this regard allows reduced concentration of copper catalyst and increased tolerance towards oxygen in the reaction system . A new and efficient method has been reported [23–25] for initiating controlled radical polymerization using activators regenerated by electron transfer (ARGET) ATRP.

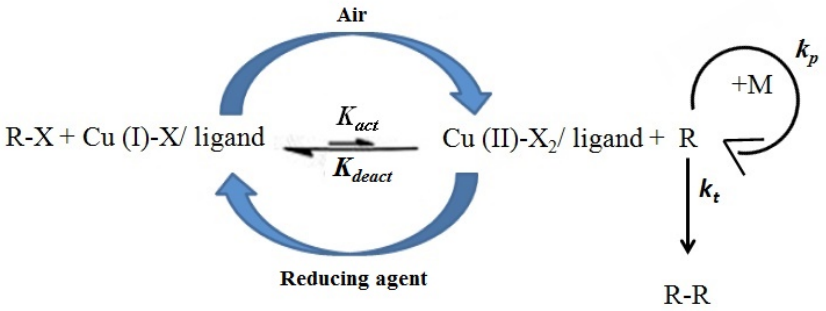

Figure 3.6: Schematic showing the mechanism of ARGET-ATRP. In the normal course of ARGET-ATRP, the catalyst is shuttled between the two oxidation states. Images taken from [26].

In a conventional ATRP polymerization, even small amounts of oxygen oxidize the Cu(I) to Cu(II) species. Since the polymerization rate is proportional to the ratio [Cu(I)] / [Cu(II)], a small amount of oxygen leads to a large reduction in polymerization rate. ARGET-ATRP overcomes this problem by using a reducing agent in the reaction mixture. The active Cu(I) complexes get regenerated from the oxidized Cu(II) species in the reaction system by the action of reducing agents (figure 3.6). These regenerated Cu(I) species thus regulate the dynamic equilibrium between the dormant and propagating species. The common reducing agents used are 2-ethylhexanoate ($Sn(EH)_2$) and ascorbic acid [27]. Sample handling with ARGET ATRP is also simplified since it is sufficient to grow brushes in a sealed environment under air. These benefits of ARGET ATRP over conventional ATRP make it a particularly attractive system for the growth of PNIPAM polymer brushes by Surface Initiated Polymerization (SIP) [26].

3.2.4 Surface patterning methods

As described in the introduction chapter, patterned substrates represent important tools used to study the behavior of cells in well defined micro-environments. In this context, a recent focus has been put on the strategies that rely on patterned polymer brushes elaborated by grafting-from protocol, for their interest in providing accurate geometric constraints to adherent cells.

Micro-contact printing The technique involves patterning a stamp (generally made up of polydimethylsiloxane (PDMS)) that is inked with the initiator molecule of interest. The inked stamp is deposited onto the surface leading to the printing of the designed pattern. The surface-bound initiator layer formed in this way can be subsequently used to grow polymer brushes via Surface Initiated ATRP protocol. Such a technique allowed designing patterned brushes used for the spatial control of single cell adhesion and polarization at micron scale [28]. Moreover, polymers with a range of functionalities and multiple components have been grafted [29]. Microcontact printing allows patterned features having a spatial resolution of the order of 5-10μm.

UV patterning A convenient method of obtaining patterned substrates involves direct patterning using a UV irradiation source to transfer a geometric pattern from a photomask onto the desired substrate. Such a technique has been used to design micropatterned surfaces based on thermoresponsive PNIPAM brushes that were used to spatially confine cell adhesion and also to actuate single cells in order to thermally induce their detachment [30]. The patterned features were spatially better resolved (on the order of 1-2μm) as compared to that obtained using micro-contact printing, thus allowing for adhesive patterns with sub-cellular resolution.

In the following section, I present the results that I obtained regarding the growth of PNIPAM brushes using ATRP and ARGET-ATRP chemical routes. I then describe an original strategy based on UV photo-ablation used to design thermo-responsive patterned substrates. The method allows a reliable means to fabricate micro-patterned molds that can be repeatedly applied for the transfer of proteins onto soft hydrogels.

3.3 Protocols for brush growth

3.3.1 Materials

N-isopropylacrylamide (NIPAM, 99%), 3-Aminopropyltriethoxysilane (APTES,99%), Triethylamine (TEA, 99.7 %), Copper (I) chloride (CuCl, 99% extra pure), Copper (II) Bromide($CuBr_2$, 99% extra pure), 1,1,7,7-Pentamethyl-diethylenetriamine (PMDETA, 99%), 2-bromo-2Methylpropionyl Bromide (BiBB, 98% pure), and Propionyl Bromide (PB, 95%) were purchased from Acros Organics. Ascorbic acid (AA, 99%) was obtained from Sigma Aldrich. All reagents were used as received except NIPAM, which was recrystallized twice in n-hexane (normapur, VWR) at 60°C and then dried for at least one day before use. Absolute ethanol and chloroform were obtained from Fischer chemicals (Laboratory Grade). Ultrapure water (18.2 MΩ.cm) was obtained from a Millipore Synergy system.

Oxidized silicon wafers were used as substrates in the present study for the growth of brushes and characterization using ellipsometry in order to test and validate the growth protocols. Si wafers were diced into 1 cm^2 pieces before use. Glass coverslips (thickness around 150μm , Thermo scientific Menzel) of 20 mm diameter were used for characterization by reflectivity (see next chapter) and in the application involving protein transfer presented at the end of this chapter.

3.3.2 Preparation of the samples

Glass and Silicon substrates were thoroughly rinsed with absolute ethanol and water, and blown dry in a stream of nitrogen. They were then transferred to a plasma cleaner (model Femto, Diener Electronics Germany, operated at 80W), where they were exposed for 6 minutes to a plasma generated in water vapour, at a pressure of 0.4 mbar. Such a treatment has been shown to yield clean and highly hydroxylated glass or oxide surfaces [31].

3.3.3 Brush growth

After the plasma hydroxylation, the substrates were grafted with a layer of 3-aminopropyltriethoxysilane (APTES) that binds covalently to silicon oxide, and exposes amine groups at the surface. The APTES amine groups were then functionalized with 2-bromo-2-methylpropionyl bromide (BiBB). This led to the surface immobilization, onto the amino-terminated sites, of surface groups with C-Br bonds that served as the ATRP initiator sites for subsequent brush growth. The last step involved growing PNIPAM chains onto the initiator grafted substrates by immersing them in an aqueous solution of NIPAM monomer. The active Cu(I) species catalyzed the C-C bond formation and subsequent growth of NIPAM chains onto the C-Br initiator sites. 1,7,7-Pentamethyldiethylenetriamine (PMDETA) was used as the ligand (in excess) to stabilize the metal complex towards disproportionation in the reaction mixture. PNIPAM brushes were grown following the protocol summarized in figure 3.7, which was adapted from previous works [30–32].

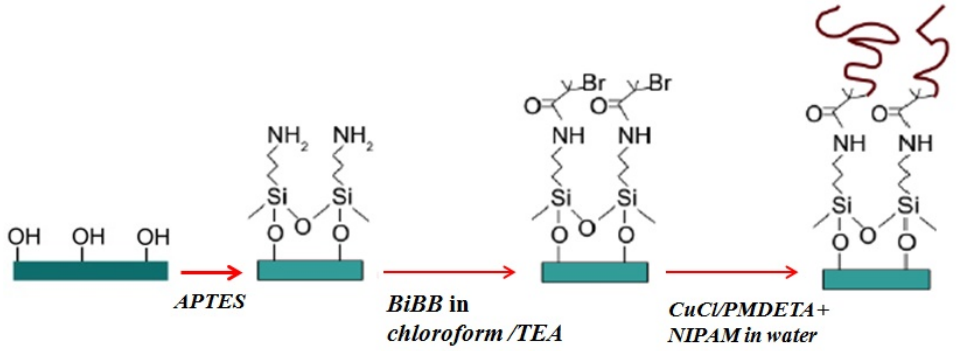

Figure 3.7: Schematic showing the ATRP brush growth: starting from a hydroxylated surface, APTES is grafted and functionalized to obtain a layer of surface-bound ATRP initiators, from which PNIPAM polymerization is performed.

Growing the APTES monolayer The plasma cleaned substrates were immersed in APTES solution (comprising of $25\mu L$ APTES, 0.5mL TEA, and 25 mL toluene) in order to form a (sub)monolayer of APTES on the surface. The chemical species were mixed and stirred for a few seconds and then immediately used (this prevented the hydrolysis of ethoxysilane groups). After APTES deposition, the substrates were sonicated for about 10-15 seconds in pure toluene, followed by rinsing with ethanol, water and ethanol again before drying.

Covalent grafting of the initiator The -NH_2 groups of the deposited APTES layer were then derivatised as follows. The APTES grown substrates were immersed in a fresh solution of BiBB ($250\mu L$) in chloroform (25 mL) with TEA (1.25mL). The solution was stirred well and then immediately used. The NH_2 terminated substrates were immersed in this solution for about 1 minute, and then rinsed copiously with pure chloroform followed by repeated rinsing with ethanol/water/ethanol.

Brush growth using ATRP A solution of NIPAM (0.6 g in 20mL pure water was mixed with $150\mu L$ PMDETA) was de-oxygenated for half an hour under continuous argon supply, after which Copper (I) Chloride (15mg) was added. Chain growth then proceeded by ATRP mechanism by immersing the functionalized substrates in the NIPAM solution containing the Copper(I)/ ligand mixture for prescribed amounts of time (from a few seconds up to two hours).

Brush growth using ARGET-ATRP PNIPAM brushes were also grown from the initiator-grafted substrates using the recently established ARGET ATRP technique that allowed performing well controlled radical polymerization reactions in ambient air (figure 3.8).

A solution of NIPAM (1.0 g) in ultrapure water (20mL) was prepared in a beaker containing a small stir bar. $CuBr_2$ (3mg) and the complexing ligand PMDETA ($40\mu L$) were sequentially added while stirring. The solution turned blue at this stage. Upon addition of ascorbic acid (30mg), the solution became colourless, due to the reduction of Cu(II) to Cu(I) . The solution was immediately poured onto the initiator-grafted substrates placed into petri-dishes that were then closed during the polymerization reaction. Polymerization was left to proceed for a prescribed amount of time (between 2 minutes and 2 hours), after which the substrates were taken out of the reaction solution and thoroughly rinsed with water.

3.3.4 Varying the brush grafting density

The variation of grafting density was changed by varying the number of ATRP initiators present on the surface following three different protocols.

- Adjusting the surface density of APTES by changing the sample immersion time in order to obtain submonolayers of APTES
- Changing the number of ATRP-active sites by functionalizing a dense APTES layer with a mixture of BiBB and PB. Propionyl bromide (PB) was used to passivate the amine groups. Functionalizing the APTES sites using PB exposed the surface with a C-methyl bond (figure 3.8) with no possible halide exchange essential for initiation. This prevented brush growth at the methyl terminated sites.
- Changing the number of ATRP-active sites by functionalizing a dense APTES layer in two steps: first with PB and then with BiBB.

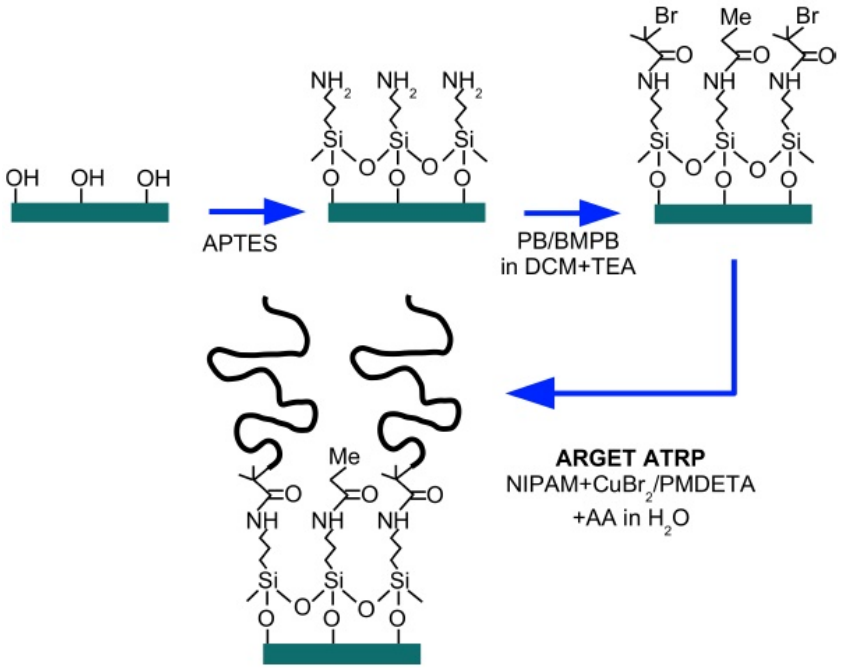

Figure 3.8: Scheme of ARGET-ATRP protocol: the initiator density can be varied through BiBB and PB molecules, leading to brush growth only at the initiator available sites.

3.4 Results and discussion

3.4.1 Characterization of brushes

The grown brushes were characterized by measuring their dry thickness using ellipsometry. The dry thickness h_{dry} is related to the grafting density σ and the polymerization index N by the relation

$$h_{dry} = Na^3\sigma \tag{3.10}$$

The relationship follows from the conservation of volume, where a dry chain of thickness h_{dry} spreading over an area of $1/\sigma$ occupies the same volume as N monomers of individual size a.

The absolute values of σ and N cannot be obtained simultaneously from dry thickness measurements only. However, fixing one of these parameters allows to probe the polymerization kinetics (h_{dry} as a function of N) or the effect of varying the grafting density (h_{dry} as a function of σ).

The Ellipsometry set-up

A custom built ellipsometer in the rotating compensator configuration, at a wavelength of 632 nm and an angle of incidence of 70° was used. The dry thickness of the brushes grown on oxidized silicon wafers was determined assuming a Si/SiO_2/PNIPAM multilayer, with a thickness of 2nm for the SiO_2 layer and refractive index of 1.46 for both the SiO_2/PNIPAM layer.

3.4.2 Effect of polymerization time with ATRP

In order to study the polymerization kinetics, we have monitored the brush thickness as a function of polymerization time. It can be seen on figure 3.9 that h_{dry} increases markedly in the first few seconds, displays a steady growth that is short lived, and shows signs of approaching saturation at reaction times above 5-10 minutes. Such a sharp increase in initial thickness followed by a clear decline in the growth rate suggests poor growth control over the ATRP mechanism under the conditions used here. Indeed, let us first recall that the rate of ATRP reaction (referring to equations 3.8 and 3.9) is expressed as:

$$R_p = k_p[P^\bullet][M] \tag{3.11}$$

with k_p the rate of monomer addition, $[P^\bullet]$ the concentration of growing radicals, and $[M]$ the monomer concentration. Neglecting termination, we expect $[P^\bullet]$ to be constant during the reaction. Since polymerization occurs only at the surface, we can roughly estimate the amount of monomer from the bulk solution that is converted into polymer as follows: assuming a typical sample surface of 1 cm^2 and a grafting density of $\sigma = 1$ chain.nm^{-1} (which corresponds to an extremely high density), we estimate a number of chains of $\sigma S = 10^{14}$. For a polymerization index growing from $N = 1$ to $N = 10000$ (the latter corresponding to high molecular weight of 10^6 g/mol for PNIPAM) in the course of the polymerization process, we thus compute a number of converted monomers ranging from $N\sigma S = 10^{14}$ to 10^{18}, *i.e.* $1.6 \times 10^{-10} - 1.6 \times 10^{-6}$ mol, which should be compared to the 5 mmol of NIPAM monomer initially present at the start of the reaction. We can therefore consider that also [M] stays constant during brush growth. Finally, k_p represents the rate of monomer addition, *i.e.* dN/dt, and we know from Eq. 3.2 or 3.10 that the brush thickness scales linearly with N, from which we conclude that $R_p \propto dh/dt$. We therefore expect h_{dry} to grow linearly with the polymerization time.

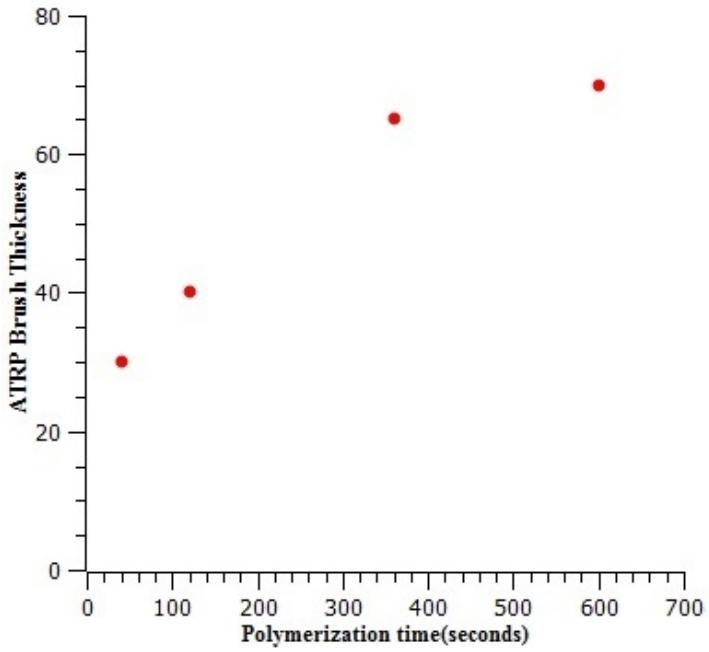

Figure 3.9: Brush thickness variation as a function of polymerization time.

In contrast to this expectation, an initial fast increase in brush thickness is observed that could be attributed to the generation of a large number of active radicals. Furthermore, slowing down and saturation may arise either due to early termination effects caused by increased radical coupling or because of a too low Cu(I)/Cu(II) ratio in the reaction system since the polymerization is performed in air.

3.4.3 Effect of polymerization time with ARGET-ATRP

Using ARGET-ATRP protocol, we observe, as shown on figure 3.10, a steady increase of h_{dry} over long polymerization times, up to one hour. Compared to the above ATRP results, there is no initial jump in the thickness, and no evidence for saturation in the growth. This shows that, although $h_{dry}(t)$ is not strictly linear, the growth of brushes by ARGET-ATRP is better controlled. Moreover, thickness measurements performed at different locations over a surface of about 1 cm^2 yields the same results within 1 nm variations showing that the brushes are homogeneous over large scales.

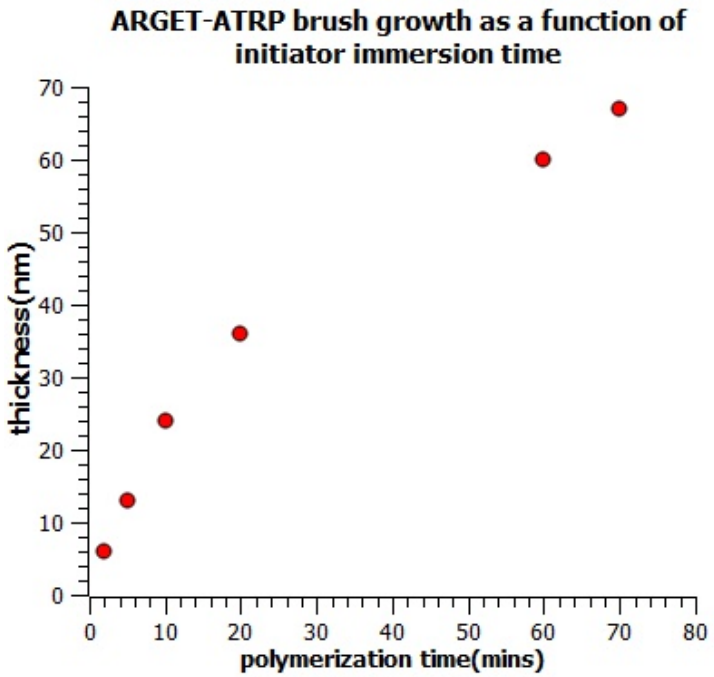

Figure 3.10: (a) Brush thickness as a function of polymerization time for ARGET-ATRP

We expect such a better controlled kinetics to result from the fact that a reduced concentration of catalyst species in the reaction system leads to the generation of low number of active radicals. Hence, the initial growth rate of brushes is slower than with ATRP as observed in the figure 3.10. The decreased coupling between the propagating radicals reduces the early termination effects. This leads to a steady increase in chain growth over the course of reaction. The concentration of catalyst species in the reaction system is maintained by the reducing agent that prolonges the growth of brushes. These results lead us to the understanding that ARGET-ATRP protocol offers better growth control of PNIPAM brushes over the conventional ATRP method. This synthesis strategy

was used to grow PNIPAM brushes for biological applications addressed in the last section of the chapter.

3.4.4 Effect of varying the APTES density

As a first attempt to adjust the brush grafting density, we have investigated the effect of varying the surface coverage of APTES at the first step of surface functionalization. This is done by changing the substrate immersion time in the APTES solution. It is seen on figure 3.11 that, while keeping the polymerization time constant, h_{dry} shows a linear increase with silanization time, up to 10 minutes, followed by a plateau.

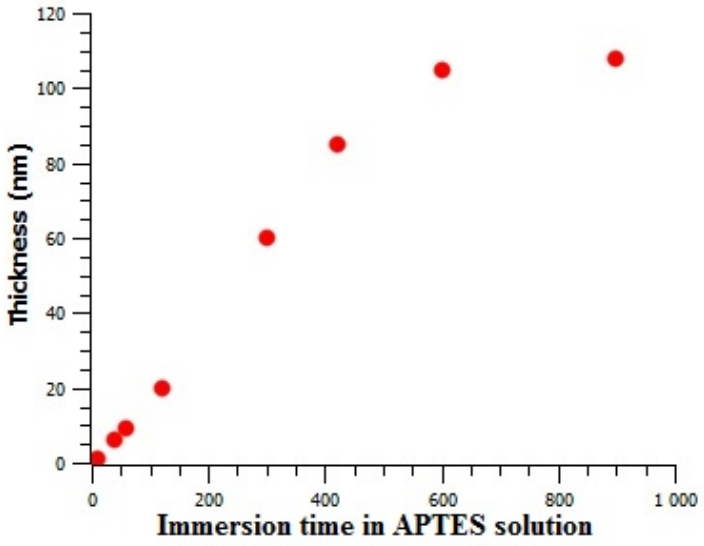

Figure 3.11: Brush thickness variation as a function of silanization immersion time (polymerized for 1 hour) obtained using ARGET-ATRP protocol

The initial increase is attributed to the progressive increase in the surface coverage of NH_2 terminated sites. The plateau reached after 10 minutes is likely to correspond to the formation of a full APTES monolayer. We have observed that immersing the substrates for times longer than 15 minutes results in a decrease of h_{dry} below the plateau value. We attribute this to the buildup of APTES multilayers, as confirmed by ellipsometry measurements of the silane layer thickness, reaching up to 3 nm, *i.e.* more than the expected monolayer thickness of ≤ 1 nm. The large range of h_{dry} covered when varying the silanization time (from a few up to a hundred nm) suggests that such a procedure is an efficient method for tuning the brush grafting density. However, low density brushes fabricated this way showed a poor stability when immersed for prolonged time (several hours) in water, resulting in a gradual decrease of h_{dry}. The most likely reason could be the chain degrafting due to hydrolysis of the siloxane bonds at the substrate/silane interface. In contrast, brushes obtained from full APTES monolayers displayed an excellent stability under the same conditions, possibly because intermolecular bonds between neighboring APTES molecules (see figure 3.8) help stabilizing the silane layer. Therefore, full APTES monolayers were used, and a different strategy to lower the ATRP initiator

density is investigated.

3.4.5 Tuning the APTES functionalization

As an alternative approach, we have studied the effect of varying the surface occupancy of ATRP initiator sites, post the APTES grafting step. This involved immersing the APTES substrates in a solution having a fixed concentration of brominated species composed of ATRP initiator (BiBB) and blank (PB) molecules. Such a method was inspired from previous works following the ATRP strategy to control the growth of oligo(ethylene glycol)methacrylate brushes [32]. At first, we prepare a substrate from a solution having only BiBB as the brominated species (100% molar ratio of BiBB/PB). Subsequently, the initiator grafting density is tuned by varying the relative amounts of BiBB and PB in the final solution (10% and 1% molar ratio). The growth kinetics of brushes obtained with 100%, 10%, and 1% molar ratios BiBB are compared on figure 3.12. It can be seen that, for a given polymerization time, the brush thickness decreases with a decrease in the initiator molar content (figure 3.12(a)). We attribute this to the progressive decrease in the occupying density of ATRP-active sites. Moreover, as seen on figure 3.12b, normalizing the three $h_{dry}(t)$ curves by the value of the thickness reached at the longest polymerization time shows that the increase in brush thickness with time occurs very similarly for the three grafting densities, suggesting that polymerization kinetics is not strongly affected by the density of initiators on the surface.

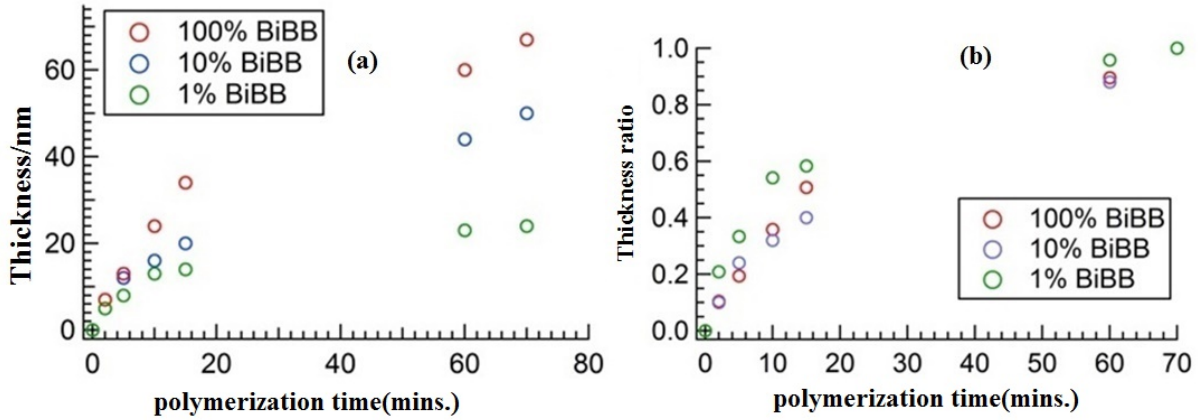

Figure 3.12: (a) Brush dry thickness as a function of time for 100%, 10% and 1% BIBB. (b) Normalized growth kinetics as a function of polymerization time for different initiator densities. Final brush thickness taken as the reference value for normalization.

We expected that such a strategy should be able to effectively control the brush grafting density. However, we observe here that a 100-fold decrease in the bulk initiator fraction brings about only a three-fold reduction in brush thickness. This suggests that BiBB binds to the surface much faster than PB molecule, which makes the control of the grafting density difficult.

This led us to adopt another method to vary the grafting density. This strategy was not studied extensively, but a few tests yielded the following encouraging results. An intermediate step was added between the APTES grafting and BiBB functionalization step. The APTES substrates were first immersed in a PB solution for a prescribed amount of time (1.5 and 6 minutes) followed by immersing in the BiBB solution, in order to first

passivate a fraction of the NH_2 groups, before functionalizing the remaining ones with BIBB. The use of two different PB immersion times thus enabled us to obtain brushes displaying a medium density (MD, obtained with 1.5 min of PB passivation) and a low density (LD, obtained with 6 min passivation time) as compared to the maximum density (HD) substrates. The LD and MD substrates were polymerized in parallel with a control substrate having maximum initiator density. The MD brush was found to have a dry thickness of $h_{dry}^{MD} = 40$ nm, while the full density control had a thickness of $h_{dry}^{HD} = 140$ nm. The LD brush displayed $h_{dry}^{LD} = 29$ nm, for $h_{dry}^{HD} = 200$ nm. We were thus able to lower the grafting density for MD brush by a factor of around 3 and for LD brush by a factor of 7. These samples were used in the study involving characterization of PNIPAM brushes by optical reflectivity, as described in the next chapter.

3.4.6 Surface patterning techniques

PNIPAM brushes have been previously patterned in our laboratory using the deep-UV ablation technique. Glass coverslips were first grafted with the initiator layer followed by a homogeneous PNIPAM brush growth all over the surface. The brushes were then selectively degraded via deep-UV irradiation using a photomask having designed features. Such a protocol could be used to pattern brushes having thicknesses up to several tens of nanometers. However, it was observed that the selective degradation of brushes under UV light was dose dependent i.e. longer exposure times were required to ablate the brush layers as their thickness increased.

A novel patterning protocol

In order to make this technique more versatile and exposure independent, we have developed an alternative "Patterning and Growing" method that we employ in the present study to fabricate patterned PNIPAM brushes. At first, the glass coverslip is grafted with the APTES layer and then functionalized with the initiator layer as done previously (figure 3.13(b)). Following this, a quartz-chromium patterned photomask is placed on top of the glass coverslip using a few μL of hexadecane spread at the sample/mask interface in order to ensure tight contact. The coverslip is then irradiated with UV light ($\lambda \leqslant 185$nm) for about 2 minutes through the photomask which allows complete removal of grafted initiator molecules at selected places (figure 3.13(c)). The substrate is carefully rinsed with ethanol and then blown dried using an N_2 stream. At this stage, the patterned initiator is ready to act as the template for brush growth (figure 3.13(d)). PNIPAM brushes are finally grown on the patterned initiator sites using ARGET-ATRP protocol as described previously (figure 3.13(e)).

Patterned brush features

We have qualitatively assessed the potential of our protocol in terms of the shapes and sharpness of the obtained brush patterns. A Photomask having hexagonal, rectangular and oval shaped features (seen via brightfield imaging in figure 3.14(a)) was used to pattern the initiator layers. The grown brushes having patterned features can be seen via phase contrast images (figure 3.14(b)). The images show that brushes can indeed be

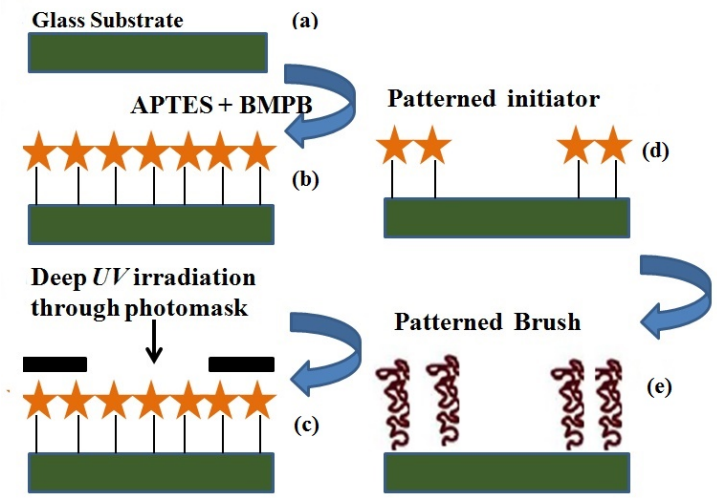

Figure 3.13: Elaboration steps: Deep UV patterning of the grafted brush surface(b,c), yielding an initiator patterned surface(d). Following PNIPAM polymerization, a polymer brush which is selectively removed by UV irradiation (e).

patterned via this method, and display features that closely resemble those present on the photo-mask. The contrast on these images arises from the difference in the height and refractive index between the polymer covered regions and the bare glass regions from where the polymer layers are removed off by the exposure of UV-irradiated source. These qualitative checks suggest that the initiator layer gets actually ablated or degraded by UV exposure. This called for further assessing the fidelity of the current fabricating technique.

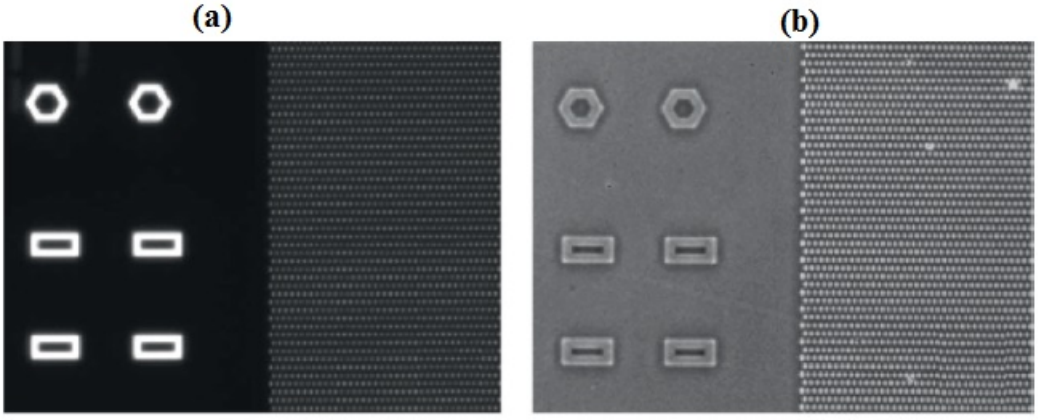

Figure 3.14: (a) bright field image of patterns on photomask (image size 486x365μm). (b) phase contrast image of corresponding patterns on a coverslip (image size 486x365μm).

AFM geometric brush features

We have evaluated the efficiency of the currently used strategy by analyzing the geometric features of the patterned brushes using Atomic Force Microscopy (AFM). The oval features of the photomask (figure 3.15(a)) are seen to be well correlated with smooth oval brush patterns mapped by AFM topography (figure 3.15(b)). The AFM mapping reveals

that the PNIPAM brush patterns are 1-2μm broader than the original patterns on the photomask. The height of the brush patterns probed by AFM (tapping mode) is found to be around 30-32 nm and shows minimal variations when probed over a number of oval shapes (figure 3.15(b,c) blue line). This value was consistent with the thickness of 33 nm quantitatively determined by ellipsometry measurements on brushes grown on control wafers of silicon. Thus, we conclude that with an exposure time of around 2 minutes, the initiator layer is fully degraded, and that the bottom in the AFM height features (figure 3.15(c)) is devoid of any brush, otherwise the height of the features would not match the ellipsometric values.

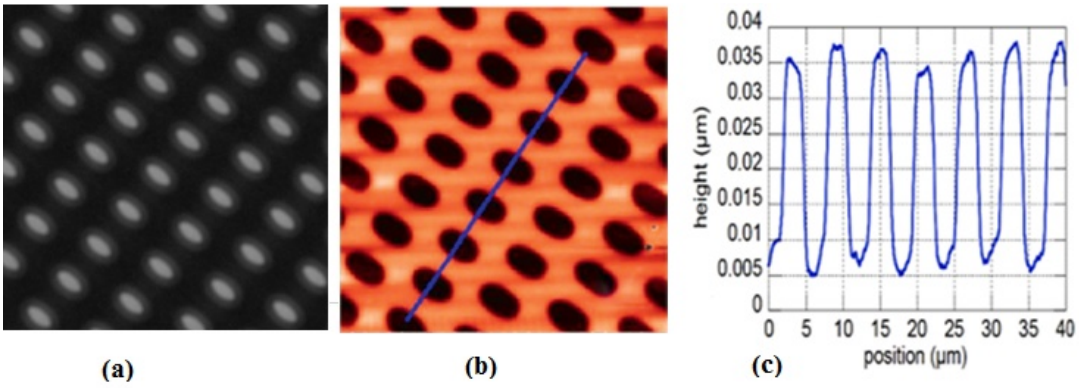

Figure 3.15: (a) Phase contrast microscope image of the photomask (50x50 μm). (b) AFM topography scan (50x50 μm) in a region of a coverslip exhibiting oval patterns. (c) height profile measured along the blue line drawn on image (c): height of features is 30-32 nm, consistent with the ellipsometric thickness of 33 nm measured for this sample

These observations highlighted the fact that the above patterning method is a fast, robust and reliable way to design patterned PNIPAM brushes useful for cell based applications discussed in the following section.

3.5 Application of patterned brushes

The results that I present in this section have been obtained by Richard De Mets during his PhD at LIPhy. I incorporate these results in order to illustrate that patterned PNIPAM brushes have been directly applied, at the laboratory scale, for cell adhesion studies.

The patterned PNIPAM substrates have been used as templates to fabricate micropatterns onto soft hydrogels based on poly-acrylamide (PAA) with sub-cellular resolution. The fabrication relies on:

- Elaborating a master mold made of patterned brushes grafted onto a thick glass plate
- Coating the mold via non-specific adsorption of proteins
- Casting of a pre-gel solution on the coated mold
- lifting off the polymerized hydrogel layer bearing the transferred protein patterns

3.5.1 Fabrication of brush based mold

Brush patterning A thick glass plate is used as the substrate instead of coverslips. This ensures a good mechanical resistance of the glass mold. The molds are sufficiently flat allowing for large scale homogeneity of the patterns transferred onto Polyacrylamide (PAA) gels. The protocol to fabricate micropatterned brushes relies on the following steps.

- Grafting the initiator, at maximum density, through previously described ATRP protocol.
- Patterning the substrate using a UV light source through the photomask.
- Employing the ARGET-ATRP protocol to make PNIPAM based brushes onto the UV exposed patterned substrates. PNIPAM brushes displayed a dry thickness in the range 50-100 nm.

The patterned mold thus obtained was used for protein coating and gel casting.

Protein Coating Once the PNIPAM glass mold was made, its surface was coated with a protein of interest. The mold was first cleaned with Phosphate buffer saline (PBS), and a drop of protein solution comprising of fibronectin and fibrinogen (fluorescent fibrinogen was used here for pattern imaging by fluorescence microscopy) was sandwiched between the patterned glass mold and a glass coverslip (figure 3.16A,B), and left for incubation during one hour at room temperature, followed by rinsing with PBS.

Gel casting Coating of the mold with protein was immediately followed by gel casting. A solution of acrylamide was put directly onto the mold. A silanized coverslip was placed over the droplet, and the gel was left for curing at room temperature for about 45 minutes. Then, the top coverslip, along with the gel bound to it through the silane layer was carefully peeled off the mold after immersion in water. The gel was washed copiously with PBS before use for cell seeding.

Cell seeding Mouse Embryonic Fibroblast cells were used for the experiments. The cell suspension was seeded onto the gel surface followed by gentle mixing in order to evenly distribute the cells over the surface. The gel surface was placed inside an incubator at 37°C under quiescent conditions. The unattached cells were washed out while the remaining cells adhered and spread on the gel by keeping the gel coverslip for about 2 hours in the incubating conditions before imaging.

3.5.2 Pattern transfer

Patterned polymer brushes have been previously used as potential substrates for protein patterning [28, 30]. In this work performed at LIPhy, Fluorescence imaging was used to observe and characterize the surface of PAA gels after they were lifted off the mold.

The transferred patterns having different well-defined patterned features are seen to be present at the surface of the PAA gels as shown in figure 3.16(C). These patterns are homogeneously distributed over large scales.

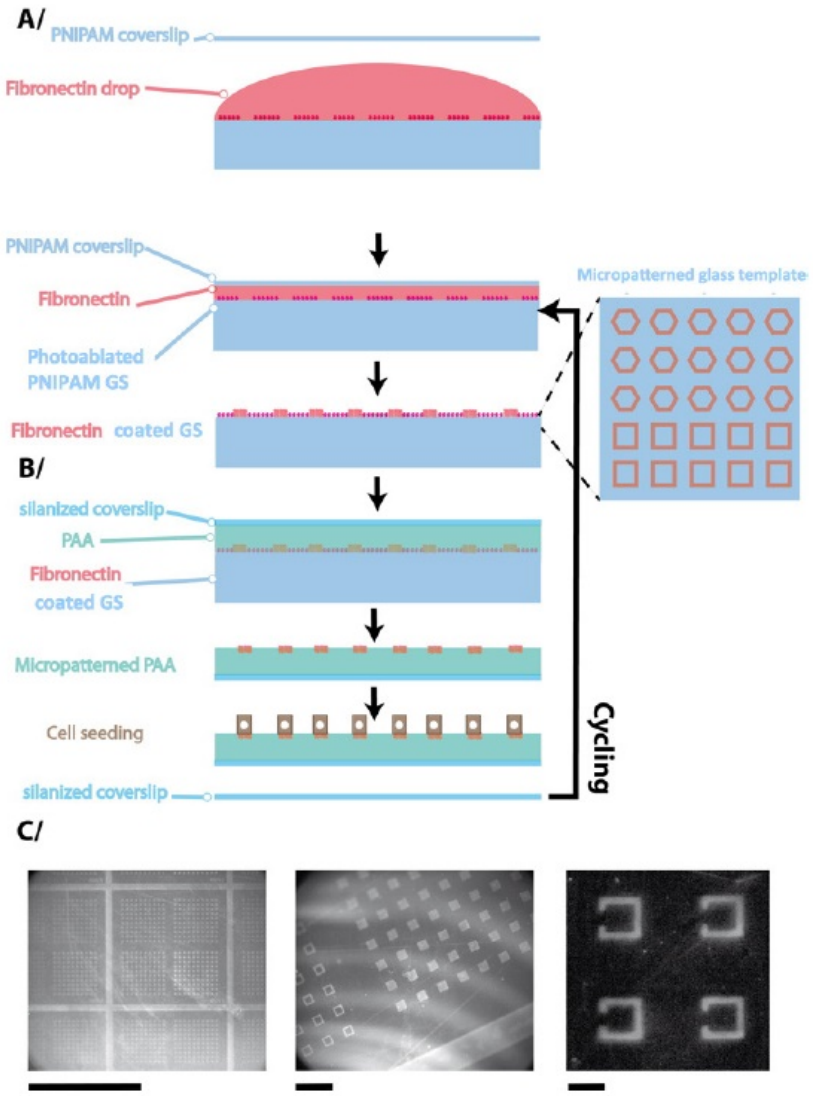

Figure 3.16: Polyacrylamide patterning from PNIPAM glass template. (A) a drop of ECM proteins (fluorescent fibrinogen mixed with non fluorescent fibronectin) is squeezed in between the patterned PNIPAM glass surface and a counter-coverslip. (B) After rinsing the functionalized glass surface with PBS a drop of polyacrylamide is sandwiched between the patterned PNIPAM surface and a silanized glass coverslip. After 45 minutes polymerization, the silanized coverslip is detached from the glass surface while ECM protein are transferred onto the gel. (C) Fibronectin and fibrinogen coating on micropatterned polyacrylamide at different magnifications. Scale bars are respectively 1.5 mm (left), 100 μm (middle), 30 μm (right).

As in previous pattern-transfer techniques [33–35], the present transfer protocol requires no chemical functionalization of the gel surface. Proteins get physically embedded in the gel network upon curing and crosslinking of the pre-gels in close contact with the

patterned mold. The mechanism being largely protein-independent, it is anticipated that the present transfer protocol should be applicable to other ECM proteins as well.

3.5.3 Patterned hydrogels for constraining cell adhesion

Fluorescence microscopy has been used to analyse the quality of the hydrogel patterns. Figure 3.17(A) shows that the fluorescence intensity profile across the arrow shaped patterns reveals a good signal-to-noise ratio corresponding to an array of proteins over the patterned regions. This indicates that the proteins are well localized over the patterns. Brightfield microscopy and fluorescence images of the actin skeleton of MEF cells seeded onto the gel surface is shown in figure 3.17(B,C). The images show that such patterned hydrogels can indeed be used to confine the adhesion of cells. The images indicate that the ECM proteins close to the gel surface are accessible to the cells, and that the bare PAA background surface exhibit non-adhesive characteristics.

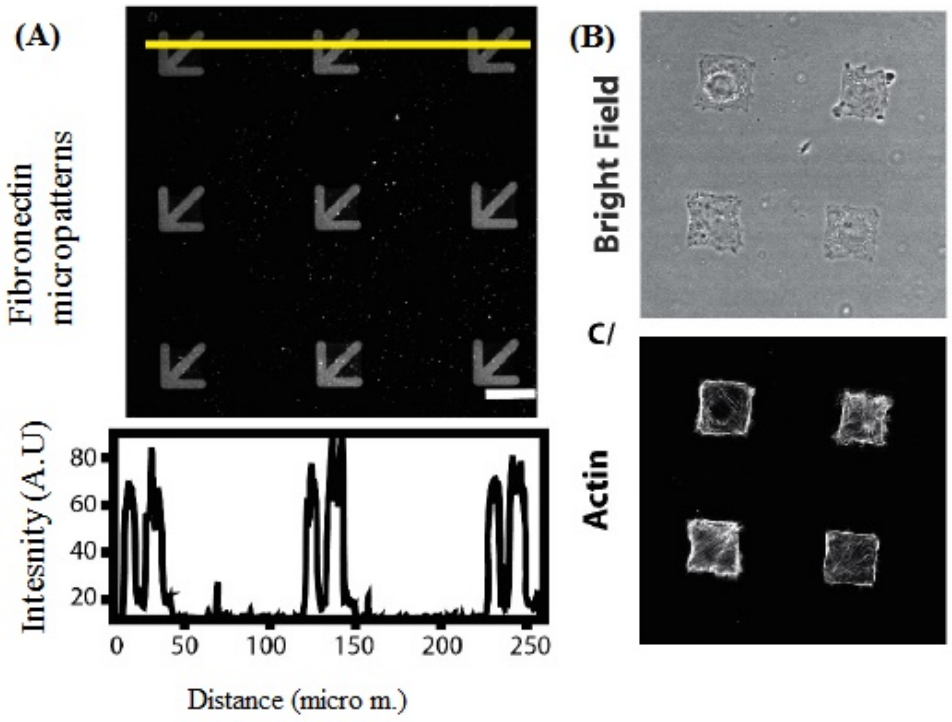

Figure 3.17: (A) Linescan of fluorescence intensity along line (yellow). Scale bar represent 30 μm (B) MEF cells (phase contrast) plated on arrow shaped micropatterned on polyacrylamide and (C) their related immunofluroscence staining.

3.5.4 Reusability

One of the striking advantage of the current patterning protocol lies in the re-usability of a mold several times. This comes from the robustness of the covalently bound polymer brush. The above feature is an improvement over previously employed protocols [33] that have relied on less robust and weakly anchored polymer layer for protein patterning. In order to assess the recyclability aspect of the mold, it is subjected to repeated

coating/casting/lift-off processes to produce different generations of gels, onto which the shapes of the seeded cells can be monitored. Between each series of experiment, the molds were thoroughly cleaned before usage. It can be seen in figure 3.18 that the same patterned mold could be re-used up to 20 times without noticing any significant change in cell shape.

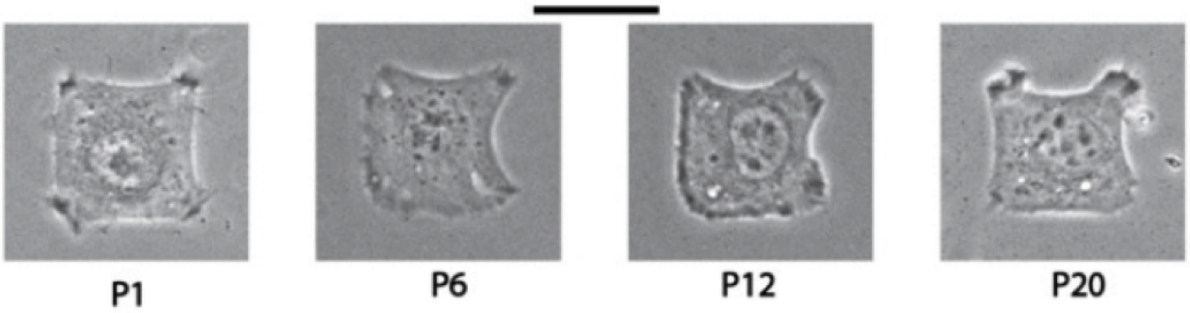

Figure 3.18: MEF cells confined by arrow-shaped patterns (A) on the first (P1), sixth (p6), twelfth (p12) and twentieth (P20) elaborated with the same mold. Scale bar: 30 μm.

Moreover, owing to the high stability of chemically grafted PNIPAM brushes, the elaborated molds can be stored at ambient conditions for further use in cell based experiments.

3.5.5 Coupling with Traction Force Microscopy

Gel patterning can be combined with Traction Force Microscopy (TFM) in order to understand the basic mechanisms governing the dynamic cell-cell and cell-ECM interactions that define its response [35, 36]. Typically, TFM involves determining the tractions exerted by cells on their substrate by monitoring the displacement of fluorescent beads encased at the near surface of the gel. When cells adhere and exert forces onto the substrate, this displaces the beads at the gel surface. From the monitoring of this displacement field, a stress field can be computed.

In order to probe the response of a cell confined to a fixed geometry, the patterned gel substrates fabricated here were employed for TFM. The hydrogels were prepared and patterned as explained earlier, and seeded with fluorescent nanoparticles, as described previously [36]. Cells were spread onto the patterned gels for about 4 hours. After this, confocal fluorescence imaging of the nanoparticles located near the gel surface, just beneath the cells, was performed. Finally, the cells were detached and reference images of unstressed gels were taken at the previously imaged cell positions. A previously described Fourier transform traction cytometry (FTTC) algorithm [36,37] was used to compute the stress field associated with the forces exerted by the cells on the substrate by measuring the resultant displacement field of the beads. Figure 3.19(A) shows the fluorescence image of the nanoparticles present at the surface of an arrow-shaped gel pattern, along with the computed stress field.

The obtained TFM results are compared with previous studies on PAA hydrogels exhibiting similar mechanical properties, but patterned using deep-UV photochemistry

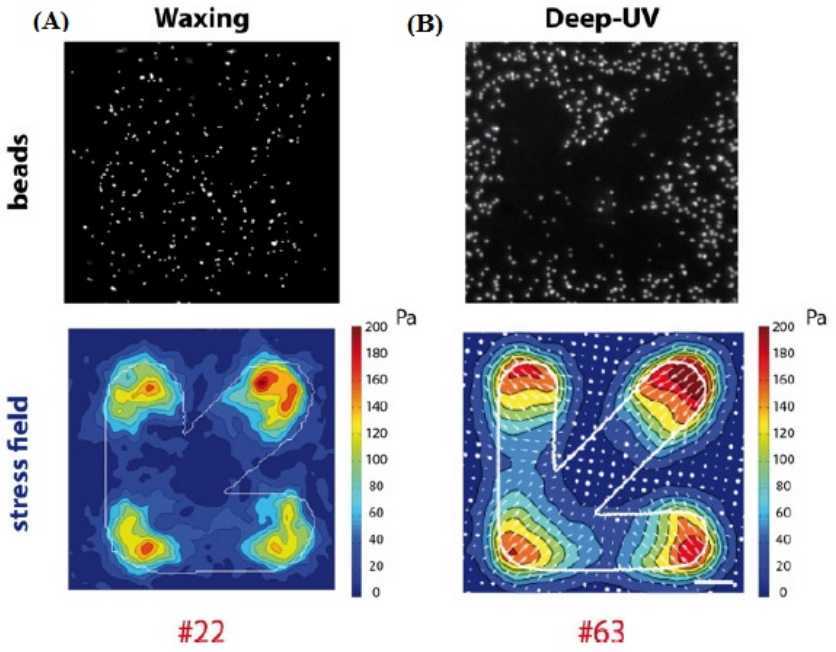

Figure 3.19: Direct comparison of stress fields obtained with the same force reconstruction algorithm using 2 different PAA patterning methods. (A) upper panel: representative fluorescence image of beads obtained using the present "waxing" method based on transfer of proteins from the PNIPAM mold to the PAA gel. Lower panel: associated stress map, obtained from averaging over 22 individual cells. (B) upper panel: image of beads after deep-UV patterning of the gel, showing that some beads are bleached below the arrow shaped pattern. Lower panel: stress field obtained from 63 cells. Scale bar : $6\mu m$.

in order to bind proteins to the surface [37] (Fig 1.19 (B)). Comparing these two set of results, the following conclusions can be drawn:

- Both patterning techniques yield similar stress maps where the stress is concentrated at the vertices of the adhesion patterns. The stress levels in these regions reach up to 200 Pa in both cases. This observation validates quantitatively the current patterning method.
- Deep-UV photochemical protein coupling resulted in partial bleaching of the beads below the patterns (figure 3.19B), whereas the present method allows maintaining the fluorescent particles fully intact over the whole surface of the gel, thus improving the spatial resolution of the computed stress field, as can be seen on figure 3.19, where the stress concentration region in the upper left vertex of the pattern is seen to be composed of two different zones, which are not resolved with photochemistry patterning.

The above observations show that the present patterning technique provides advancement in terms not only of ease-of-use for gel preparation, but also in terms of space resolution of the computed stress fields in TFM experiments.

3.6 Conclusion

We discuss the synthesis protocols used to grow PNIPAM brushes using ATRP and ARGET-ATRP. The growth of polymeric chains is seen to be modulated by varying the APTES silane concentration, polymerization time and the grafting initiator density. The polymerization in ATRP leads to poorly controlled brush growth with an initial sharp increase followed by early termination. Brush growth using ARGET-ATRP method provides better growth conditions for PNIPAM brushes in a high throughput manner. The reducing agent maintains a constant catalyst supply that supports a steady brush growth over prolonged durations .

We describe an alternate "patterning and Growth" protocol employed to design micropatterned PNIPAM substrates using Deep-UV ablation technique. The patterning strategy is used to fabricate patterned PNIPAM brushes having features that resemble closely to the original photomasks with an accuracy in the range of 1-2 μm. This marks an advantage over previously used patterning techniques such a microcontact printing. The geometric pattern features are consistent with those characterized via Ellipsometry. Such a potential patterning strategy is employed to generate micro-patterned hydrogels from PNIPAM based molds. Compared to the existing well-established templating techniques, the current method presents the following features:

- polymer brushes are elaborated from facile chemical routes.
- Polymer brushes based on PNIPAM can be grown in a robust way on glass substrates.
- Deep-UV patterning allows micron-scale patterning of the brushes in one single degradation step, without the need to degrade the gel or the target proteins by deep UV irradiation.
- Patterned hydrogels could be successfully used as templates onto which cells can modify their organization and adhere in a fixed arrangement.
- The patterned hydrogels as observed from fluorescent imaging technique show in plane homogeneity.
- Based on covalently grafted polymer brushes, such patterned molds show excellent usage and long term stability.
- These fabricated gel based substrates could be re-used for several experiments for cell substrate anchorage studies.

The latter features are a major improvement with respect to other patterning techniques, as they reduce greatly the number of elaboration steps steps required for microfabrication with many gels having similar patterns to be produced for high resolution TFM studies.

Bibliography

[1] Jürgen Rühe, *Polymer brushes- towards tailor made surfaces*, Wiley Online Library (2004).

[2] William J Brittain and Sergiy Minko, "A structural definition of polymer brushes", *Journal of Polymer Science Part A: Polymer Chemistry* **45**(16), pp. 3505–3512 (2007).

[3] ST Milner, TA Witten, and ME Cates, "Theory of the grafted polymer brush", *Macromolecules* **21**(8), pp. 2610–2619 (1988).

[4] Raphael Barbey, Laurent Lavanant, Dusko Paripovic, Nicolas Schuwer, Caroline Sugnaux, Stefano Tugulu, and Harm-Anton Klok, "Polymer brushes via surface-initiated controlled radical polymerization: synthesis, characterization, properties, and applications", *Chemical reviews* **109**(11), pp. 5437–5527 (2009).

[5] Graeme Moad and David Henry Solomon, *The chemistry of radical polymerization*, Elsevier (2005).

[6] Henry Hsieh and Roderic P Quirk, *Anionic polymerization: principles and practical applications*, CRC Press (1996).

[7] Jin-Shan Wang and Krzysztof Matyjaszewski, "Controlled/" living" radical polymerization. atom transfer radical polymerization in the presence of transition-metal complexes", *Journal of the American Chemical Society* **117**(20), pp. 5614–5615 (1995).

[8] Krzysztof Matyjaszewski and Jianhui Xia, "Atom transfer radical polymerization", *Chemical reviews* **101**(9), pp. 2921–2990 (2001).

[9] Wade A Braunecker and Krzysztof Matyjaszewski, "Controlled/living radical polymerization: features, developments, and perspectives", *Progress in Polymer Science* **32**(1), pp. 93–146 (2007).

[10] Daniel J Siegwart, Jung Kwon Oh, and Krzysztof Matyjaszewski, "Atrp in the design of functional materials for biomedical applications", *Progress in polymer science* **37**(1), pp. 18–37 (2012).

[11] Krzysztof Matyjaszewski, "Atom transfer radical polymerization (atrp): current status and future perspectives", *Macromolecules* **45**(10), pp. 4015–4039 (2012).

[12] Krzysztof Matyjaszewski and Thomas P Davis, *Handbook of radical polymerization*, Wiley (2002).

[13] Atsushi Goto and Takeshi Fukuda, "Kinetics of living radical polymerization", *Progress in Polymer Science* **29**(4), pp. 329–385 (2004).

[14] Mitsuo Sawamoto and Masami Kamigaito, "Living radical polymerizations based on transition metal complexes", *Trends in polymer science* **4**(11), pp. 371–377 (1996).

[15] Krzysztof Matyjaszewski, Nicolay V Tsarevsky, Wade A Braunecker, Hongchen Dong, Jinyu Huang, Wojciech Jakubowski, Yungwan Kwak, Renaud Nicolay, Wei Tang, and Jeong Ae Yoon, "Role of cu0 in controlled/living radical polymerization", *Macromolecules* **40**(22), pp. 7795–7806 (2007).

[16] Timothy E Patten and Krzysztof Matyjaszewski, "Atom transfer radical polymerization and the synthesis of polymeric materials", *Advanced Materials* **10**(12), pp. 901–915 (1998).

[17] Krzysztof Matyjaszewski, Timothy E Patten, and Jianhui Xia, "Controlled/living radical polymerization. kinetics of the homogeneous atom transfer radical polymerization of styrene", *Journal of the American Chemical Society* **119**(4), pp. 674–680 (1997).

[18] Fabio di Lena and Krzysztof Matyjaszewski, "Transition metal catalysts for controlled radical polymerization", *Progress in Polymer Science* **35**(8), pp. 959–1021 (2010).

[19] Wei Tang and Krzysztof Matyjaszewski, "Effect of ligand structure on activation rate constants in atrp", *Macromolecules* **39**(15), pp. 4953–4959 (2006).

[20] Xuejun Wang, Huilin Tu, Paul V Braun, and Paul W Bohn, "Length scale heterogeneity in lateral gradients of poly (n-isopropylacrylamide) polymer brushes prepared by surface-initiated atom transfer radical polymerization coupled with in-plane electrochemical potential gradients", *Langmuir* **22**(2), pp. 817–823 (2006).

[21] Rajendra R Bhat, Michael R Tomlinson, and Jan Genzer, "Orthogonal surface-grafted polymer gradients: A versatile combinatorial platform", *Journal of Polymer Science Part B: Polymer Physics* **43**(23), pp. 3384–3394 (2005).

[22] Jayachandran N Kizhakkedathu, Kainthan Rajesh Kumar, Diane Goodman, and Donald E Brooks, "Synthesis and characterization of well-defined hydrophilic block copolymer brushes by aqueous atrp", *Polymer* **45**(22), pp. 7471–7489 (2004).

[23] Wojciech Jakubowski and Krzysztof Matyjaszewski, "Activator generated by electron transfer for atom transfer radical polymerization", *Macromolecules* **38**(10), pp. 4139–4146 (2005).

[24] Ke Min, Haifeng Gao, and Krzysztof Matyjaszewski, "Preparation of homopolymers and block copolymers in miniemulsion by atrp using activators generated by electron transfer (aget)", *Journal of the American Chemical Society* **127**(11), pp. 3825–3830 (2005).

[25] Wojciech Jakubowski and Krzysztof Matyjaszewski, "Activators regenerated by electron transfer for atom-transfer radical polymerization of (meth) acrylates and related block copolymers", *Angewandte Chemie* **118**(27), pp. 4594–4598 (2006).

[26] Phanindhar Shivapooja, Linnea K. Ista, Heather E. Canavan, and Gabriel P. Lopez, "ARGET-ATRP Synthesis and Characterization of PNIPAAm Brushes for Quantitative Cell Detachment Studies", *Biointerphases* **7**(1-4) (2012).

[27] Yungwan Kwak, Andrew JD Magenau, and Krzysztof Matyjaszewski, "Arget atrp of methyl acrylate with inexpensive ligands and ppm concentrations of catalyst", *Macromolecules* **44**(4), pp. 811–819 (2011).

[28] Julien E Gautrot, Britta Trappmann, Fabian Oceguera-Yanez, John Connelly, Ximin He, Fiona M Watt, and Wilhelm TS Huck, "Exploiting the superior protein resistance of polymer brushes to control single cell adhesion and polarisation at the micron scale", *Biomaterials* **31**(18), pp. 5030–5041 (2010).

[29] Feng Zhou, Zijian Zheng, Bo Yu, Weimin Liu, and Wilhelm TS Huck, "Multicomponent polymer brushes", *Journal of the American Chemical Society* **128**(50), pp. 16253–16258 (2006).

[30] Kalpana Mandal, Martial Balland, and Lionel Bureau, "Thermoresponsive micropatterned substrates for single cell studies", *PLoS One* **7**(5), pp. e37548 (2012).

[31] Ibrahim B Malham and Lionel Bureau, "Density effects on collapse, compression, and adhesion of thermoresponsive polymer brushes", *Langmuir* **26**(7), pp. 4762–4768 (2009).

[32] Andrew A Brown, Neelam S Khan, Lorenz Steinbock, and Wilhelm TS Huck, "Synthesis of oligo (ethylene glycol) methacrylate polymer brushes", *European polymer journal* **41**(8), pp. 1757–1765 (2005).

[33] Timothée Vignaud, Hajer Ennomani, and Manuel Théry, "Polyacrylamide hydrogel micropatterning.", *Methods in cell biology* **120**, pp. 93–116 (2013).

[34] Xin Tang, M Yakut Ali, and M Taher A Saif, "A novel technique for micro-patterning proteins and cells on polyacrylamide gels", *Soft matter* **8**(27), pp. 7197–7206 (2012).

[35] Andrew D Rape, Wei-hui Guo, and Yu-li Wang, "The regulation of traction force in relation to cell shape and focal adhesions", *Biomaterials* **32**(8), pp. 2043–2051 (2011).

[36] Kalpana Mandal, Irène Wang, Elisa Vitiello, Laura Andreina Chacòn Orellana, and Martial Balland, "Cell dipole behaviour revealed by ecm sub-cellular geometry", *Nature communications* **5** (2014).

[37] Qingzong Tseng, Irene Wang, Eve Duchemin-Pelletier, Ammar Azioune, Nicolas Carpi, Jie Gao, Odile Filhol, Matthieu Piel, Manuel Théry, and Martial Balland, "A new micropatterning method of soft substrates reveals that different tumorigenic signals can promote or reduce cell contraction levels", *Lab on a chip* **11**(13), pp. 2231–2240 (2011).

Chapter 4

Probing the conformation of PNIPAM brushes by optical reflectivity

4.1 Abstract

In the current chapter, I introduce an original set-up based on Reflection Interference Contrast Microscopy (RICM). I employ it to investigate the thermal response of PNIPAM brushes over a range of surface densities σ and chain lengths N. The brushes are grown following the previously described grafted-from ARGET-ATRP protocol. I present the results in terms of spectral reflectance measurements and the density profile of the brushes obtained by theoretical models. The results present one of the very few experimental evidences of the phenomenon of vertical phase separation in PNIPAM brushes. I show that RICM is an interesting technique to estimate the molecular parameters of the "grafted from" polymer brushes, which is crucial for the rational design of smart polymer coatings for application purposes. The study of the temperature response of PNIPAM brushes upon heating/cooling cycling clarifies the physical origin of their hysteretic behaviour.

4.2 Introduction

PNIPAM is used in a number of biological applications that rely on the fact that adsorption/release of proteins on a brush-grafted surface depends strongly on the conformation of the polymeric chains [1,2]. These structural changes, in turn, depend on the molecular brush parameters, such as the brush grafting density σ and the chain length N. In this context, the rational design of PNIPAM brushes calls for understanding how the brush parameters influence their overall structure, the conformation of the grafted chains and the usage properties for the target application [3].

Up to now, the swelling/collapse transition of PNIPAM brushes (Figure 4.1) has been studied experimentally using Surface Plasmon Resonance (SPR) [4], Quartz Crystal Microbalance (QCM) [5–10] and force measurement techniques such as Surface Force Apparatus (SFA) [11, 12] or Atomic Force Microscopy (AFM) [9, 10, 13–15]. While SPR

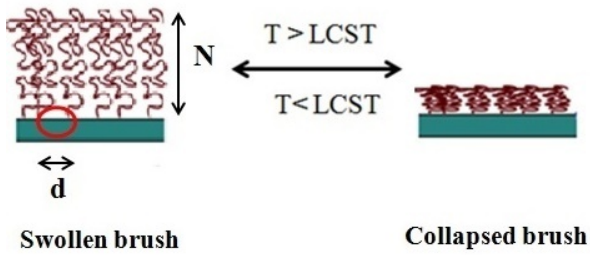

Figure 4.1: Schematic showing the temperature induced reversible brush collapse/swelling of PNIPAM grafted brush surfaces. The brush governing parameters are N, the chain length and ($\frac{1}{d^2}$), the grafting density σ.

and QCM have allowed monitoring the qualitative evolution of brush properties such as refractive index or effective mass with temperature, force measurements techniques have analysed the temperature-dependent brush swelling in terms of variations in the range of steric repulsive forces. These techniques provide a qualitative picture about the structural changes in the brushes. Only Neutron Reflectivity (NR) [16–18], and *in situ* Spectral Ellipsometry(SE) [19] have provided quantitative information about the evolution of the axial structure (*i.e.* of vertical density profile) of the brushes as a function of temperature. Brought together, these various studies have led to the following conclusions:

- The magnitude of conformational changes of PNIPAM brush depends on the grafting density and chain length [12, 17].
- PNIPAM brushes undergo thermal hysteresis during heating/cooling cycles [4, 7, 8].
- Densely grafted brushes collapse non-homogeneously within their thickness and display a so-called vertical phase separation around the LCST [17, 19].

In the following parts of the introduction, I will highlight the essential features of Neutron reflectivity (NR), or spectral Ellipsometry (SE) in resolving the height profile of the brush in terms of the monomer volume fraction ϕ as a function of the vertical distances from the grafted surface z.

4.2.1 Thermodynamics of polymer solutions

The temperature-dependent conformation of PNIPAM brushes is related to the particular thermodynamic properties of PNIPAM/water solutions.

The properties of polymer solutions are governed by the balance of monomer/monomer and monomer/solvent interactions. This balance determines the phase diagram of the solution, which can be described in terms of its free energy of mixing.

The Flory-Huggins energy equation The free energy for a polymer solution can be described by the Flory-Huggins free energy expression [20] such that

$$\frac{\triangle F}{k_B T} = \Big[\frac{\phi}{N}\ln(\phi) + \ln(1-\phi)(1-\phi) + \chi\phi(1-\phi)\Big] \tag{4.1}$$

where $k_B T$ is the thermal energy, ϕ is the volume fraction of the polymer having a degree of polymerization N, and χ is the the interaction parameter that characterizes

the difference of interaction energies between monomer/monomer and monomer/solvent. The energy equation comprises of first two entropic terms and the last energetic term that depends on the sign of χ.

The dependence of the equilibrium state of the polymer solution on χ and T can be understood by constructing a phase diagram. Typically, the phase diagram is expressed by $T(\phi)$ (or $\chi(\phi)$) plot as shown in figure 4.2(a) by determining the boundary conditions ($\frac{dF}{d\phi}$ and $\frac{d^2F}{d\phi^2}$=0) for the equilibrium state. The salient features of a $T(\phi)$ plot are as follows:

- A binodal (solid line) : It describes the co-existence curve, that separates the stable one-phase region from an unstable two-phase region.
- The plot displays a certain minimum value in the phase diagram that is referred to as the critical point (red spot), above which any infinitesimal change in a thermodynamic variable (T or χ) leads to an abrupt change in the solution properties.

The Flory parameter

The flory parameter is usually seen to be dependent only on temperature. The temperature dependence of χ can be written as the sum of two terms

$$\chi(T) \sim A + \frac{B}{T} \tag{4.2}$$

having a temperature independent entropic term A, and an enthalpic part B/T. The above parameters are seen to vary for different polymer/solvent combinations. Depending on the value of χ, the polymer solution shows the following features.

- If B is positive, then χ decreases as temperature in increased. Under this situation, the polymeric species interact more with the solvent than with each other. This leads to polymer solution exhibiting an Upper Criticial Solution Temperature (UCST) such that for all temperatures greater than T_c, a homogeneous one-phase solution exists.
- If B is negative, the situation is reversed, leading to the solution exhibiting a Lower Critical Solution Temperature (LCST) such that for temperatures lower than T_c, single phase solution exists, as shown in figure 4.2(a).

For T (or χ) values below the critical point (red dot), a homogeneous mixture is stable at any composition. However, for values higher than the critical point, there occurs an equilibrium state corresponding to two phases with different compositions that co-exist in the solution.

The phase behaviour of aqueous PNIPAM solutions has been studied using calorimetric techniques by Afroze *et al* [21] (figure 4.2(b)). These authors have shown that, in order to describe the experimental phase diagram, modifications were required in the Flory-Huggins equation by imposing a dependence on the polymer concentration ϕ of the interaction parameter χ such that χ_{eff}= $\chi(\phi, T)$. Furthermore, they obtained a ϕ-dependence of χ that was consistent with the fact that PNIPAM/water solutions demix

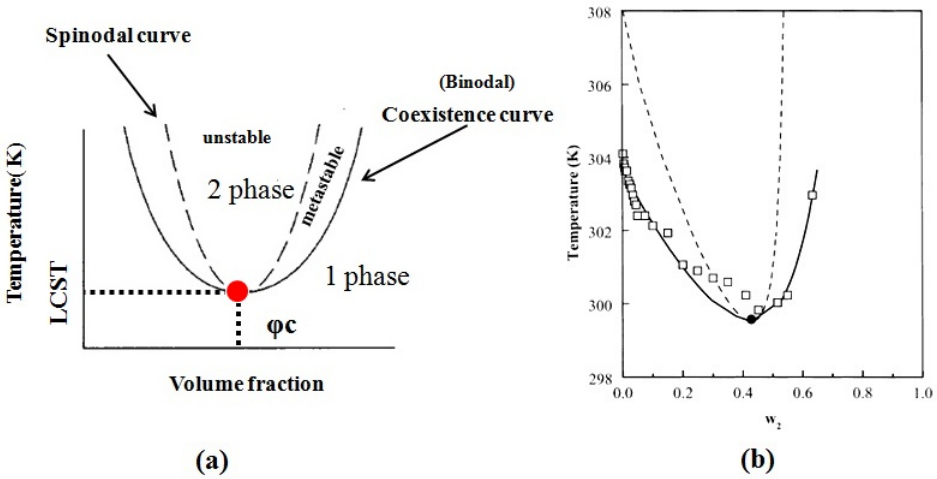

Figure 4.2: Schematic showing (a) a binodal (solid line) defining the co-existence curve. A spinodal (dashed line) marking the crossover from metastable to unstable phase showing spontaneous phase separation, and a metastable state in the region marked between the spinodal and binodal, and the critical point (red spot) (b) predicted binodal (solid line), spinodal (dashed line), and critical (solid dots) conditions for PNIPAM/ water mixtures, and experimental results (hollow squares) for the demixion temperature T_{dem} of PNIPAM/ water mixtures taken from [18]

via a type-2 phase transition, characterized by the coexistence of two different phases having finite polymer concentrations, a higher ϕ^+ and a lower ϕ^- [21]. Such a co-existence has been theoretically predicted to form the basis for a vertical phase separation phenomenon in PNIPAM brushes, *i.e.* the presence, close to the LCST, of a dense brush region near the grafted substrate and a dilute region at far off vertical distances [1,22–25]. However, these theoretical features require experimental supports in order to allow clearer identification of the mechanisms at play.

Until now, Ellipsometry and Neutron Reflectivity have provided the best experimental examples for vertical phase separation seen in polymer brushes made of PNIPAM.

4.2.2 Probing a brush density profile

Ellipsometry

In Ellipsometry, a linearly polarized light source is made incident onto the surface having the material of choice (a polymer film). On reflecting from the material there occurs a change in the polarization of the incident light which forms the detection signal. The polarization state of the reflected light is decomposed into two components, the s component which oscillates perpendicular to the plane of incidence and parallel to the sample surface, and the p component that oscillates parallel to the plane of incidence (figure 4.3). The ratio of the reflection coefficients of the p and s components can be written as

$$\frac{r_p}{r_s} = \tan(\psi)\exp^{i\Delta} \tag{4.3}$$

where $\tan\psi$ denotes the amplitude ratio of two coefficients upon reflection and Δ is the phase shift. The angle of incidence is chosen to be at Brewster angle (θ_b) to ensure

maximum difference between r_p and r_s and least abrupt changes in Δ values. This allows accurate measurements of the film parameters. The determination of film parameters (for example height) is done by iterative procedures, where unknown optical constants are used to calculate the amplitude ratio and phase shifts using Fresnel's laws of reflection. The calculated values are then matched with the experimental data to assign the parameter values.

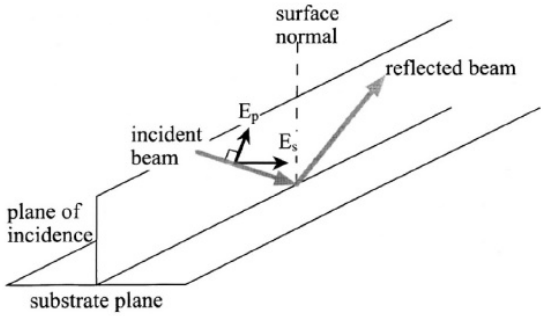

Figure 4.3: Schematic showing the direction of the electric field vector for the s-polarization and the p-polarization.

Whereas single wavelength ellipsometry relies on only one set of Ψ and Δ values and is typically limited to the determination of either the thickness or refractive index of thin films bounded by sharp interfaces, spectral ellipsometry employs a spectral source, thereby allowing to compute more complex optical characteristics of thin films, *e.g.* refractive index gradients. SE was employed to probe the collapse transition of PNIPAM brushes. The experimental results were analysed with an optical model accounting for an exponentially decaying refractive index of the brush. This showed that, as seen on figure 4.4, at temperatures close to the LCST, the brush was composed of a dense inner region, of constant index, surmounted by a more dilute one displaying a decaying index. While this indeed suggests a non-homogeneous brush collapse, the model used in this work points to the existence of rather broadly spread density gradients, which is not a clear sign of vertical phase separation.

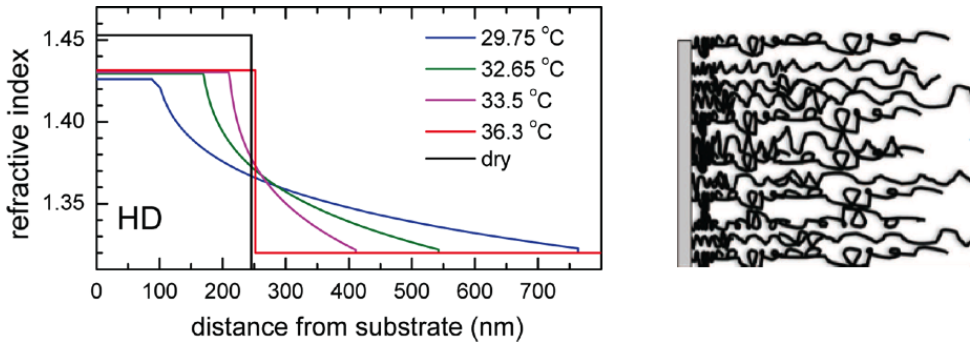

Figure 4.4: Left panel: Refractive index as a function of the distance from the substrate, for various temperatures. Close to the LCST, the brush is modeled as a double layer, with a gradient in the dilute layer. At higher temperatures, only a single layer with a constant refractive index is considered. Right panel: schematic of a structured brush, having a dense inner phase and a more dilute outer one. Images taken from [26].

Neutron Reflectivity

Neutron Reflectvity involves shining a beam of neutrons onto the surface bearing the film of interest and measuring the reflected intensity as a function of incident angle or neutron wavelength. Neutron reflectometry is a specular reflection technique, where all the incident light gets reflected back with the angle of the incident neutron beam. The reflectivity is usually described in terms of the momentum transfer vector, perpendicular to the reflecting surface denoted by q_z, which describes the change in momentum of a neutron after reflecting from the material such that

$$q_z = \frac{4\pi}{\lambda} \sin\theta \tag{4.4}$$

In order to analyze the obtained reflectivity data, theoretical models based on density profiles are required. In neutron reflectivity, this is achieved via describing the scattering length density(SLD) profiles normal to the surface, which are then converted to density profiles, *i.e.* volume fraction ϕ as a function of the distance to the substrate. The technique was used to probe the conformational changes of PNIPAM brushes as a function of temperature [18]. The modeled density profiles reported a direct evidence for a vertical phase separation in PNIPAM brushes. Upon heating, the segment profile changed from a quasi-parabolic shape to a distinct double layer around the polymer LCST and to single step-like profile at high temperatures (figure 4.5).

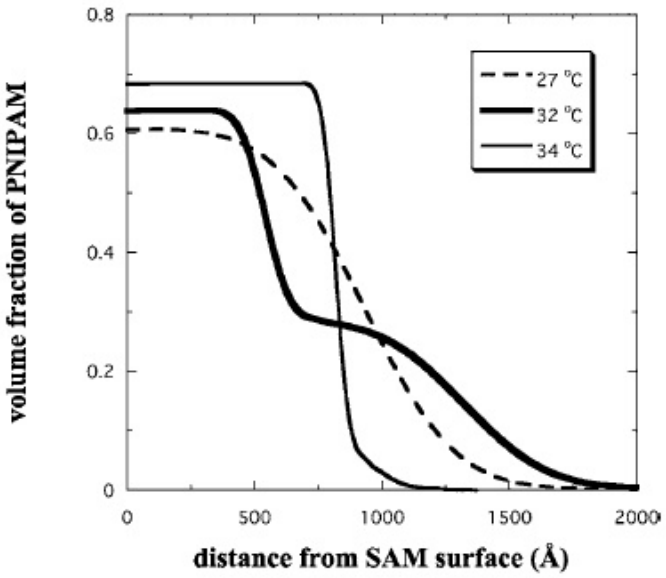

Figure 4.5: Best fit segment concentration profiles for a dense PNIAM brush at different temperatures showing the dramatic change in profile shape in the transition region. Image taken from [18]

So far, Neutron reflectivity (NR) represents the only technique that has allowed direct access to the structural evolution of PNIPAM brushes as a function of solvent quality. Moreover, theoretical predictions regarding vertical phase separation are still a matter of uncertainty despite years of research [1, 27], and require further experimental support. Hence, there is a need for experimental techniques that allow for the systematic and high-throughput screening of the effect of brush parameters on such a phenomenon. I address

this point in the present chapter and show that optical reflectivity measurements, based on Reflection interference Contrast microscopy (RICM), can provide valuable information regarding the density profiles of polymer brushes.

4.2.3 Reflection Interference Contrast Microscopy

RICM is an optical technique that can probe optical distances between two or more interfaces based on the interference patterns formed by light reflected from these interfaces.

The optical basis

RICM involves illuminating the sample with a nearly parallel beam of monochromatic incident light that is reflected by the substrate and the object under investigation placed above the substrate.

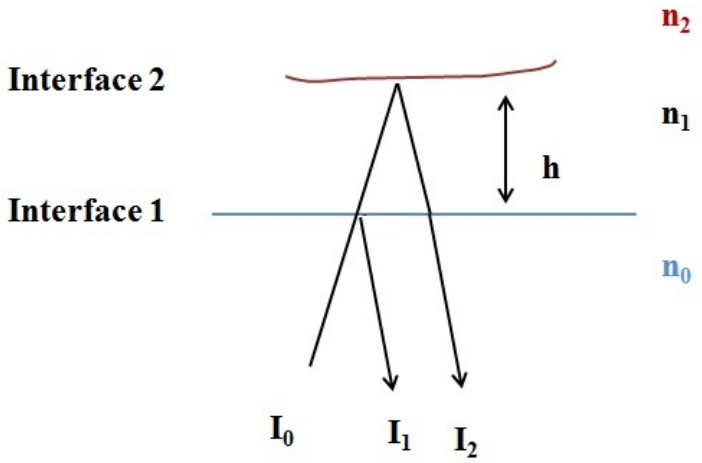

Figure 4.6: The basic principle of RICM, light reflected from different interfaces (1 and 2) in quasi-normal incidence gives rise to the resultant interference fringes. Images taken from [28].

A monochromatic incident ray I_0 at quasi-normal incidence is first reflected at the glass/medium interface (interface 1)to give the ray I_1; the transmitted ray is reflected further at the surface of the object (interface 2)and gives rise to the ray I_2 (figure 4.6). Rays I_1 and I_2 interfere and give rise to a resultant intensity I, which is given by

$$I = I_1 + I_2 + 2\sqrt{I_1 I_2}\cos[2kh(x,y) + \phi] \tag{4.5}$$

Where $k = 2\pi(\frac{n_1}{\lambda})$, ϕ a phase shift usually equal to π , and h(x,y) the distance separating the object and the substrate at lateral position (x,y).

The intensities I_1 and I_2 depend on the incident I_0 by Fresnel's law as

$$I_1 = r_{01}^2 * I_0, and \tag{4.6}$$

$$I_2 = (1 - r_{01}^2) r_{12}^2 * I_0 \tag{4.7}$$

Reflection is caused by a change in the refraction index, so on every boundary a part of the light is reflected. The amount of reflection is given by the reflection coefficient r_{ij}, according to the Fresnel reflection relation

$$r_{ij} = \frac{(n_i - n_j)}{(n_i + n_j)} \tag{4.8}$$

where i is the medium from which incident light falls onto the interface and j is the medium from where it gets reflected back to the previous medium.

The interference patterns allow precise measurements of the interfacial distances (see eq. 4.5).

Standard RICM

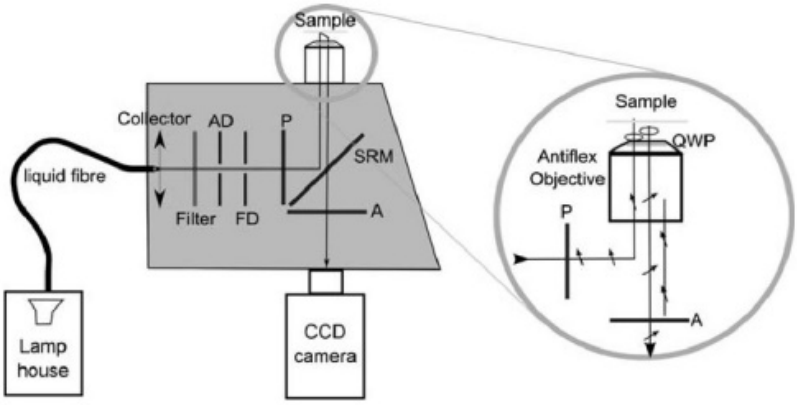

Figure 4.7: Schematic showing the RICM setup and optical path for a standard RICM microscope. AD: aperture diaphragm, FD: field diaphragm, QWP quarter-wave plate, SRM : semi-reflecting mirror, P: Polarizer, A: Analyser. The circular zoom highlighting the light polarization with the antiflex method. Image taken from [28].

The standard RICM comprises of a light source, an inverted microscope equipped with an antiflex objective and a CCD camera. The sample is observed under monochromatic illuminating light. The typical set-up is shown in figure 4.7. Illuminating light from the source passes through a collector, an interference filter and two adjustable diaphragms, an aperture diaphragm(AD) and a field diaphragm(FD) to the reflector cube. In the reflector cube, the light path is composed of a polarizer(P); a semi-reflecting mirror and a crossed polarizer(A). The objective is specially designed for RICM with a built-in Quarter Wave Plate(QWP) located in front of the front lens [28]. The quarter wave-plate is optimized for a particular wavelength, which is the recommended wavelength to use in the optical set-up.

Contrast in reflection and the Antiflex technique

The reflectivity for a polymer layer or a biological cell is usually low. In contrast to this, light coming from any part from the microscope is more intense and obscures the signal

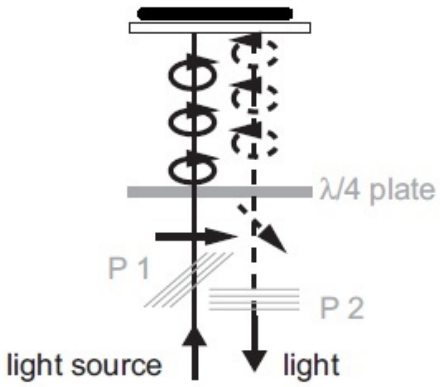

Figure 4.8: The basic principle of antiflex technique. The light gets circularly polarized by polarizer P1 and quarter waveplate. under such an effect, the polarization of light is shifted by 90° and passes through the analyser P2, which is oriented perpendicularly to P1.

of interest by contributing to noises in the images. In order to avoid this, the antiflex technique is used. Two polarisers P1 and P2 along with a quarter waveplate are placed in the path of the incoming light rays as shown in figure 4.8. The incident monochromatic light is first rendered linearly polarized by the polarizer P1 and then transformed into a circularly polarized light after passing through the Quarter Wave plate(QWP). Upon reflection of circularly polarized light from the optical interface, the direction of polarization of circularly polarized light is reversed at both the interfaces 1 and 2 (figure 4.8). After passing through the QWP, the light emerges back to a linearly polarized light, but with a polarization turned by an angle of 90° with respect to the incident light perpendicular to the incident light. An analyser P2 which is oriented perpendicular with respect to the first one, cuts off all stray lights going through it and allows only the light that passes from the QWP to exit the microscope. This allows collecting the net intensity coming only from the sample of interest.

Multi wavelength RICM

A major limitation of the conventional RICM technique is the difficulty in determining absolute height values. As the interference patterns provide a periodic series of constructive and destructive interference, absolute heights cannot be determined because the absolute phases of the lights reflected by the various interfaces are not known. In order to overcome this drawback, the sample is illuminated with another wavelength. Herein, the intensity of interference pattern for every wavelength are independently patterned. Adding another wavelength introduces another cosine function, but having a different periodicity. Additionally, the boundary conditions for both the wavelength require zero intensity at zero height, giving rise to a phase relation between the two wavelengths, and thus an unambiguous height determination (figure 4.9).

The RICM employed in the present study was adapted from the conventional RICM instrument allowing reflectivity experiments over a wavelength spectra. I describe the setup and its use in characterizing PNIPAM brushes in the Materials and Methods sec-

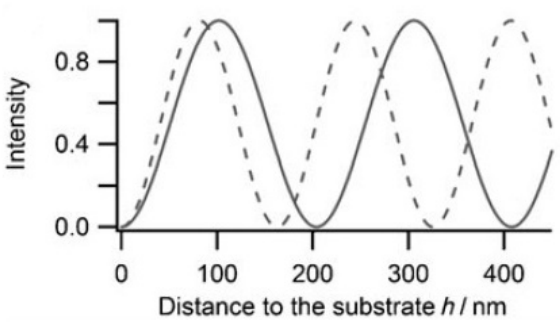

Figure 4.9: Schematic showing dual wavelength RICM (a) single green(solid lines) wavelength makes it difficult to compute absolute height from the resultant intensity. Using another wavelength (blue, dotted lines) lifts the ambiguity in computing h up to 800 nm. Images taken from [28] .

tion of the chapter.

4.3 Materials and Methods

4.3.1 PNIPAM brushes

A set of 12 different brushes were prepared on glass coverslips and Si wafers, following to the ARGET-ATRP procedure described in chapter 2. Brushes were grown at 3 different grafting densities, referred to as HD (High Density), MD (Medium Density) and LD (Low Density). The dry thicknesses of the brushes, measured by ellipsometry, are summarized in Table 1. As mentioned in chapter 2, control HD samples grown in parallel with MD and LD samples have a dry thickness suggesting that $\sigma_{MD} \simeq \sigma_{HD}/3$ and $\sigma_{LD} \simeq \sigma_{HD}/7$.

Brush	h_{dry} (nm)
HD1	200
HD2	167
HD3	138
HD4	108
HD5	90
HD6	70
HD7	62
HD8	22
HD9	17
HD10	13
MD	40
LD	29

Table 4.1: Set of brushes prepared along with their dry thickness measured by ellipsometry.

Pre-measurement protocol

The brush-grafted substrates were soaked in ultra-pure water at room temperature overnight before use in order to remove any weakly physisorbed polymer from the surface. Following this, they were dried, and the brush dry thickness was re-measured by ellipsometry. Post soaking, there was a small decrease in the thickness of the brushes, between 1nm for thinnest sample (having thickness less than 40nm) and 3-5 nm for the thickest sample. The values corresponding to the post-soaking measurements are shown in Table 4.1

4.3.2 RICM characterization

A conventional RICM set-up (figure 4.7), based on two wavelengths (470 nm and 560 nm) was used initially to perform qualitative experiments on grafted PNIPAM brush samples.

4.3.3 Spectral RICM setup

The experimental setup

The spectral reflectance instrument (figure 4.10) comprises of a white plasma light source (Thorlabs) with a continuous emission spectra in the visible range (400-800 nm). The incoming white light is linearly polarized and then coupled to the microscope using a polarising beamsplitter cube (Thorlabs). The illumination numerical aperture (INA) is set to 0.15 using a calibrated aperture diaphragm. The reflected light is detected through the beamsplitter cube and a cross polarizer.

Imaging

In contrast to standard RICM systems employing an antiflex objective (Zeiss,63X, 1.3NA) [28], the quarterwave plate in our setup is made of a mica sheet of thickness around 20-25μm is glued to the bottom of the sample (brush/glass coverslip). The mica sheet corresponds to a Quarter Wave Plate (QWP) in the 400-500nm range. This allows for control of polarization without the need of a specifically designed objective. The current approach enables us to use objectives of any magnification, immersion medium and numerical aperture. A 20X, 0.75NA super apochromat air objective (UPLSAPO 20X, Olympus) is used here to image the sample without thermal coupling through the immersion medium. The reduced chromatic and spherical aberrations ensure good image quality throughout the visible spectrum.

Spectrometer

A home built spectrometer is coupled to the output port of the microscope for spectral reflectivity measurements. A variable slit (figure 4.10a) is placed at the imaging plane to control the spectral resolution and is imaged using achromatic lenses onto a CCD camera after reflection on a diffraction grating (Thorlabs). This allows a spectral image of a line in the sample in the CCD camera (figure 4.10b). An autofocus device is coupled the microscope that allowed long-term data acquisition during temperature changes without losing the focus.

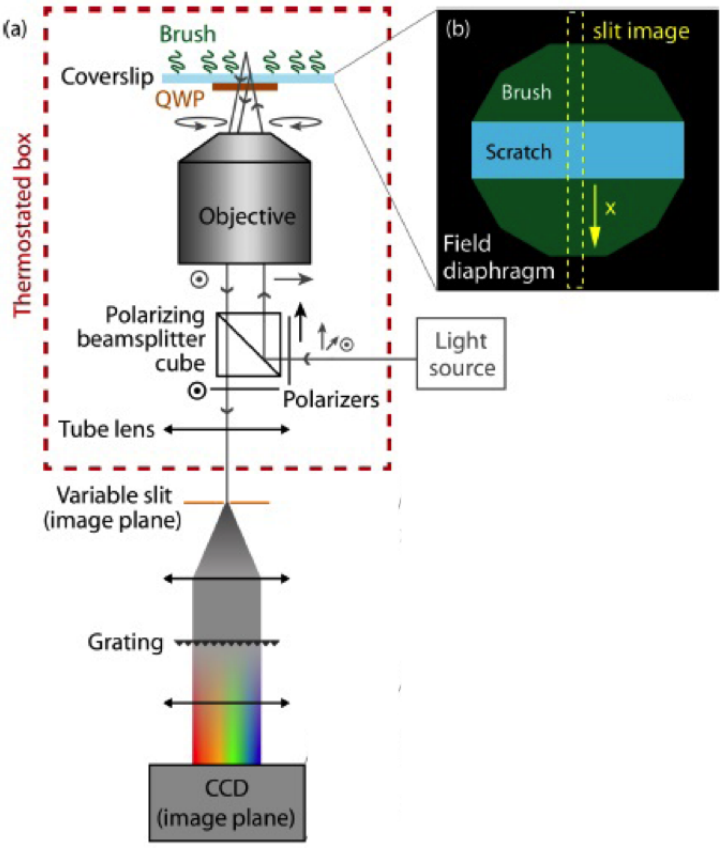

Figure 4.10: (a) Schematic view of the RICM microscope used for spectral reflectance measurements. A mica quarter wave plate (QWP) is directly glued to the bottom of the sample. (b) Schematic view of a sample image showing the position of the scratch made in the brush (used as a reference glass/water interface), and of the slit (yellow) on the image. Image adapted from Varma *et al* [29].

Temperature control

The temperature cycles were performed with a thermostated box that enclosed most parts of the microscope. Such an arrangement led to slow temperature variations during heating (0.3°C/min) and cooling down (0.15°C/min). The temperature-control system ensured that temperature changes around the samples were uniform throughout the course of the experiment, thereby allowing unbiased measurements of the brush temperature.

Temperature measurements were performed as close as possible to the imaged region of the brush. This was done by using a miniature type-K thermocouple encased within the liquid cell holder, with the sensing part placed carefully onto the brush-grafted surface. A digital multimeter(Agilent 34970A) was employed in conjugation with a second sensor measuring the reference temperature of the thermocouple cold junction, in order to monitor the temperature of the sample with an absolute accuracy of 0.1°C and a resolution of about 0.01°c. A custom-written software (Labview) was used to synchronize illumination of the sample and image acquisition with temperature measurements at fixed temperature intervals of 0.05°c.

Spectral reflectance measurements

To measure absolute spectral reflectance of the samples, brushes were scratched with a blunt steel blade, in order to locally remove the polymer layer over a narrow region (a few tens of μm in width). We placed the sample onto the microscope with the scratch on the brush located in the middle of the field of view (figure 4.10(b)). The scratch appears as a line resolved over a spectrum on the CCD. In addition, the field diaphragm of the microscope is partially closed so that its edges are visible on the CCD as dark regions on either sides of the image (figure 4.11). In this configuration, a "black" reference (using the field diaphragm image) and a "bright" reference (using the bare region in the scratch) could be simultaneously measured on the same image. Each measurement was typically performed using an exposure time of 0.5-1.0 s, limited by the signal intensity due to the small value of the reflectance of thin polymer brushes.

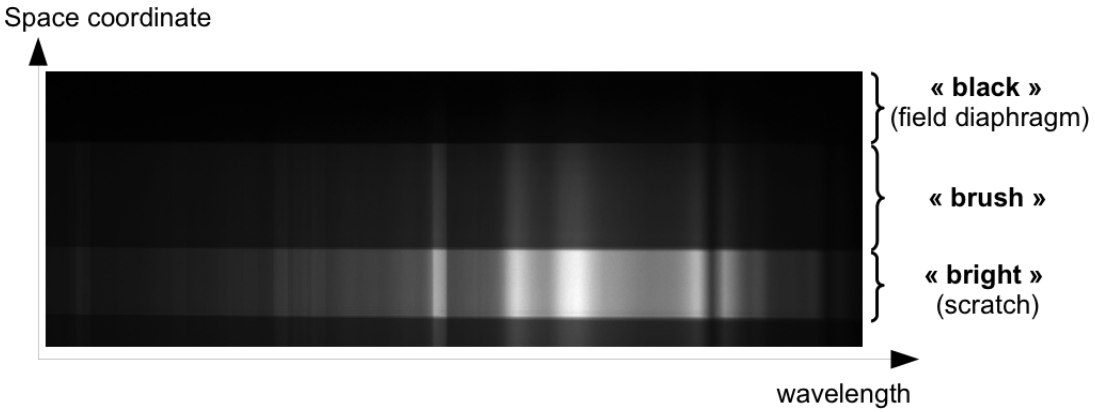

Figure 4.11: Typical image obtained in the space-wavelength plane of the CCD camera.

4.3.4 Image processing and analysis

Image processing was performed using a home-written ImageJ macro. The reflectivity of the brush covered glass is measured and calculated with respect to that of the bare glass in water. Using the "black" and "bright" references allows us to account for the light source fluctuations and background noise caused by unwanted reflections (top surface of the sample holder, mica/glass interface, etc.) For each wavelength, the quantities δ_1 and δ_2 are extracted from the RICM image (figure 4.11), with

$$\delta_1 = I_{brush} - I_{black} \tag{4.9}$$

$$\delta_2 = I_{scratch} - I_{brush} \tag{4.10}$$

where I_i are the intensities measured in the "black", "bright" and "brush" regions.

These quantities are used to obtain the reflectance, relative to that of the glass/water interface, as

$$R(\lambda)/R_{glass/water}(\lambda) = \frac{(I_{brush} - I_{black})}{(I_{scratch} - I_{black})} = \delta_1/(\delta_1 + \delta_2) \tag{4.11}$$

With the refractive indices of water and glass known, the reflectance of the sample could be computed.

From the values of $R(\lambda)$ thus computed at the various imposed temperatures, we obtain 2D temperature-wavelength maps of the sample reflectance, such as that shown on figure 4.12. From such maps, built for all the samples studied, we could extract either reflectance spectra at a selected temperature (by plotting a horizontal intensity profile) or single wavelength reflectance as a function of temperature during a heating/cooling cycle (vertical intensity profile).

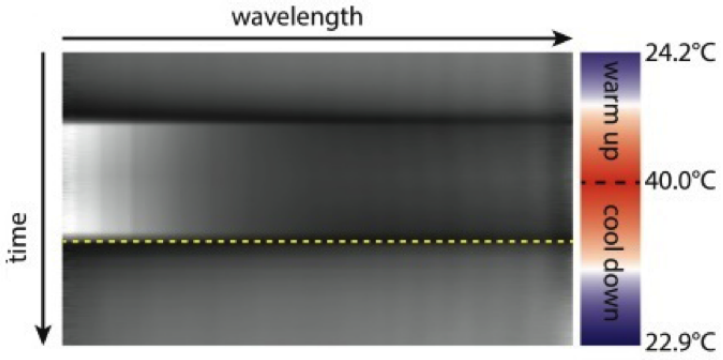

Figure 4.12: 2-D reflectance data (coded in grey levels on the map) obtained after a heating/cooling cycle from the spectral RICM experiments. Image adapted from Varma *et al* [29].

4.4 Results

4.4.1 Standard RICM imaging

At first, we have employed a conventional two-wavelength imaging RICM set-up in order to qualitatively probe the optical behaviour of PNIPAM brush/glass substrate as a function of temperature. This was done using a high density brush of dry thickness around 40nm, that was grafted onto a glass substrateand had been locally scratched in order to display a region of bare glass surface (figure 4.13). The imaged area was controlled by the RICM field diaphragm that forms a "dark" background at the image periphery. RICM images shown on figure 4.13 were built by superimposing the images obtained at two different wavelengths.

It can be seen on figure 4.13 that upon increasing the temperature across the LCST, variations in color and reflected intensity are visible in the brush-covered region of the surface. These observations suggest that the optical response of the brush is a function of the brush height and density.

These successful checks led us to systematically probe the intensity changes of the brush grown surfaces in order to obtain a clear picture of the brush response.

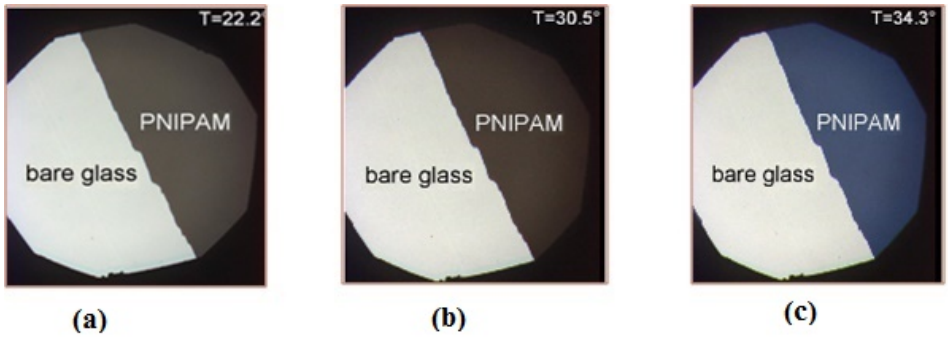

Figure 4.13: RICM images at (a) low temperature (b) around the LCST, and at (c) high temperatures. The collapse of the brush is reflected by changes in color and reflected intensity.

4.4.2 Single wavelength reflectance measurements

In order to assess the sensitivity of RICM to the thickness of the brush, we have designed a brush of dry thickness 40 nm that was patterned by deep-UV lithography (see chapter 2) in order to decrease locally its thickness down to 10 nm, over a H-shaped region (see figure 4.14a). From the measured reflected intensity over these two regions of the brush, we have built (as explained in the "Image processing" section of "Materials and methods") the reflectivity curves, measured at a single wavelength of 470 nm, as a function of temperature.

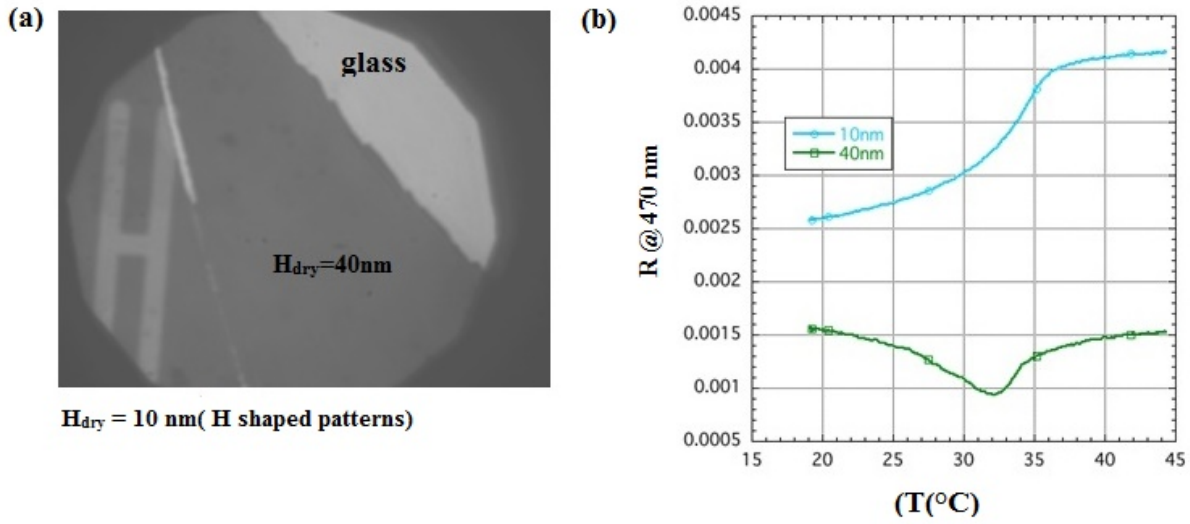

Figure 4.14: (a) A PNIPAM brush having a thickness of 40nm and a patterned region of thickness 10 nm. (b) Reflectivity curves computed over the brush of thickness 10nm (blue) and 40 nm (green curve).

It is seen on figure 4.14b that the $R(T)$ curves computed over the two regions display different magnitude and temperature dependence. Moreover, the two curves present clear variations at temperatures around the LCST. This provides strong support to the fact that RICM is a sensitive technique that should provide information regarding the height and density variations of PNIPAM brushes, including rather thin polymer layers of thickness $\sim$ 10 nm. We have attempted, as typically done in RICM data analysis (see

eq. 4.5 on p. 81), to model the brushes as thin layers of uniform refractive index $n(T)$ and height $h(T)$. However, such simple modeling assumptions did not allow to reproduce quantitatively the measured $R(T)$. This called for a more accurate modeling of the brush density profile, as well as for RICM experiments performed at multiple wavelengths, in order to have enough experimental information allowing for proper constraining of the models.

4.4.3 Spectral reflectance as a function of temperature

The spectral RICM set-up was used to analyse the set of brushes described previously in Table 1. On figure 4.15, I present a set of reflectance spectra measured at different temperatures for the HD4 brush.

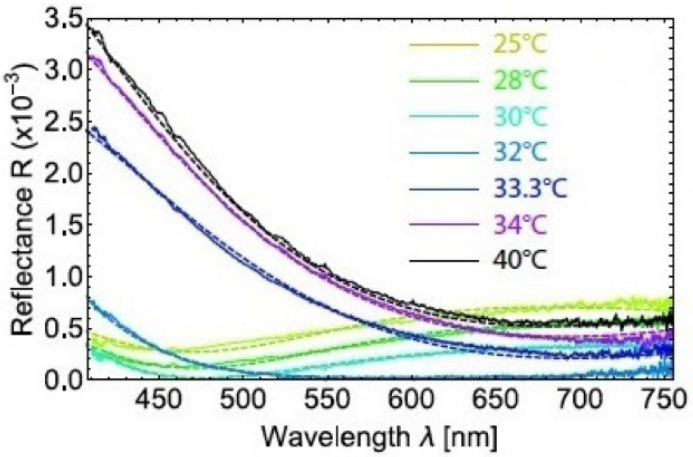

Figure 4.15: Reflectance spectra for HD4 brush at different temperatures. Solid lines are the measured spectra, and dashed lines are the best fits obtained using the density profile model described in the following section. Image adapted from Varma *et al* [29].

The spectra show qualitatively that both the magnitude and the wavelength-dependence of reflectance evolve as a function of temperature, and show significant changes around the bulk LCST of the polymer. In the following part, I describe the theoretical modeling we have performed in order to analyze such reflectance data and extract the brush density, ϕ, as a function of the vertical distance from the grafted surface z.

4.4.4 Spectral reflectance modelling

Our modeling is based on the following assumptions:

- We assume that the brush is composed of infinitesimal layers each having a reflection coefficient. Thus, the total reflection can be approximated by integrating the contribution of reflection from all the infinitesimal homogeneous axial segments. The resultant reflectance is then written as:

$$R(\lambda) = \mid \frac{(n_{glass} - n_0)}{(n_{glass} + n_0)} + \int_0^{+\infty} \frac{1}{2n(z)} \frac{\partial n}{\partial z} \exp\left(\frac{2\pi}{\lambda} \int_0^z n(z')dz'\right)dz \mid^2 \qquad (4.12)$$

  Where $n(z)$is the refractive index of the polymer brush at the axial position z.

- The refractive index of the hydrated polymer varies linearly with the monomer volume fraction $\phi(z)$ as

$$n(z) = [(n_{nipam} \times \phi(z)) + (n_{water} \times (1 - \phi(z)))] \tag{4.13}$$

Values for the refractive indices of water [30], glass [31] and PNIPAM [19] and their variation with the wavelength were taken from previous reports.

- The density profile of the brush is assumed to be made up of linear segments with different gradients. Our aim is to describe the reflectance spectra with the least possible number of fitting parameters. We have tried to fit our experimental data using profiles composed of either a single constant+linear density gradient (figure 4.16a), having 3 free parameters, which we call in the following a "single-phase" model, or composed of two such constant+linear gradients (figure 4.16b), having 6 free parameters (called "two-phase" profile). With such a simplified density model, we are however able to approximate many different shapes ranging from a simple step-like profile to a gradual density decay described by a concave or convex shape.

- The total amount of polymer is conserved (eq. 4.14), which reduces the number of free parameters for a two phase profile to 5, and for a one phase profile to 2.

$$h_{dry} = \int_0^{z_{max}} \phi(z)dz \tag{4.14}$$

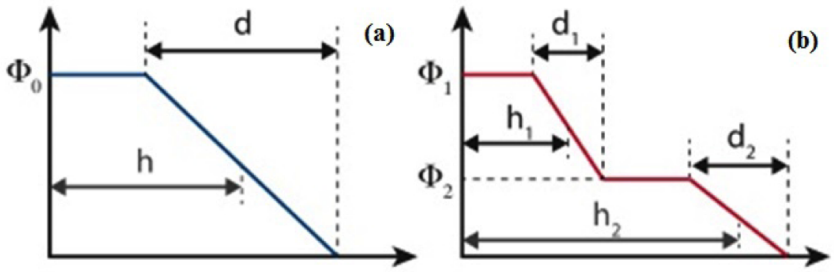

Figure 4.16: Schematic showing (a) a one-phase and (b) two-phase profile with the parameters used to decribe each profile. The parameters in black are independent and used to fit the profile, while the parameters in gray are deduced from the conservation of the total amount of monomer. Parameters h, h_1, and h_2 are the distances from the wall (z=0) to the midpoint of the linear decays. Image adapted from Varma *et al* [29].

Under these assumptions, we obtain the reflectance as a function of the 5 (2 for a one layer model) parameters:

$$R(\lambda) = (r_0 + r_1 + r_2)^2 \tag{4.15}$$

with

$$r_0 = \left(\frac{n_{glass} - n_1}{n_{glass} + n_1}\right) \tag{4.16}$$

$$r_1 = \frac{1}{4}\exp\left[\frac{4i\pi n_1}{\lambda}(h_1 + d_1\frac{n_1}{2(n_1 - n_2)})\right] \times \left(E_i(\frac{-2i\pi d_1 n_2^2}{(n_1 - n2)\lambda}) - E_i(\frac{-2i\pi d_1 n_1^2}{(n_1 - n2)\lambda})\right) \tag{4.17}$$

$$r_2 = \frac{1}{4}\exp\left[\frac{4i\pi}{\lambda}[(n_2(\frac{h_s - h_1\phi_1}{\phi_2})+n_1h_1+\frac{d_2n_wn_2}{2(n_2-n_w}\right]\times\left(E_i(\frac{-2i\pi d_2n_w^2}{(n_2-nw)\lambda})-E_i(\frac{-2i\pi d_2n_2^2}{(n_2-nw)\lambda})\right) \quad (4.18)$$

Where E_i is the exponential integral function, Δn=n_{nipam}-n_{water}, n_w=n_{water}, n_1=$\Delta n\times$ $\phi_1 + n_w$, and $n_2 = \Delta n \times \phi_2 + n_w$. The five adjusted parameters h_1, ϕ_1, ϕ_2, d_1 and d_2 are shown on figure 4.16, and h_{dry} is the dry thickess of the PNIPAM brush measured by ellipsometry. d_1 and d_2 are the density gradients.

The formula for a single phase profile is straightforwardly obtained by setting $r_2 = 0$, $\phi_2 = 0$, and $h_1 = h_s/\phi_1$.

Fitting of the experimental spectral reflectances using the above relations was performed using Mathematica in order to determine the values of the 5 (2) adjustable parameters allowing the quantitative description of the measured spectra. A discussion regarding our fitting procedure, the uniqueness of the fit solution, and a comparison of our model with the output of other models for the density profile is provided at the end of the chapter.

4.4.5 Density profiles at high temperatures

Starting with a simple situation, I first discuss the density profiles of the brushes obtained at temperatures well above the LCST (typically $T \geq 35°C$). As seen on figure 4.17, where I present data obtained for brush HD4, we find that at high temperatures, the reflectance spectra can be well fitted using a single-phase density profile having a constant volume fraction (ϕ=0.9∼1). Figure 4.17 shows that both the single- and two-phase models converge to similar best-fit solutions, which correspond to a density profile that is essentially step-like. Moreover, the distance z at which the brush density drops to zero is observed to be, within about 10%, in good quantitative agreement with the value of h_{dry} measured independently by ellipsometry. This was observed for all the brushes studied here. This provides a first validation of our data analysis, and shows that, as expected, PNIPAM brushes at temperatures well above the LCST are collapsed under the form of a homogeneously dense layer.

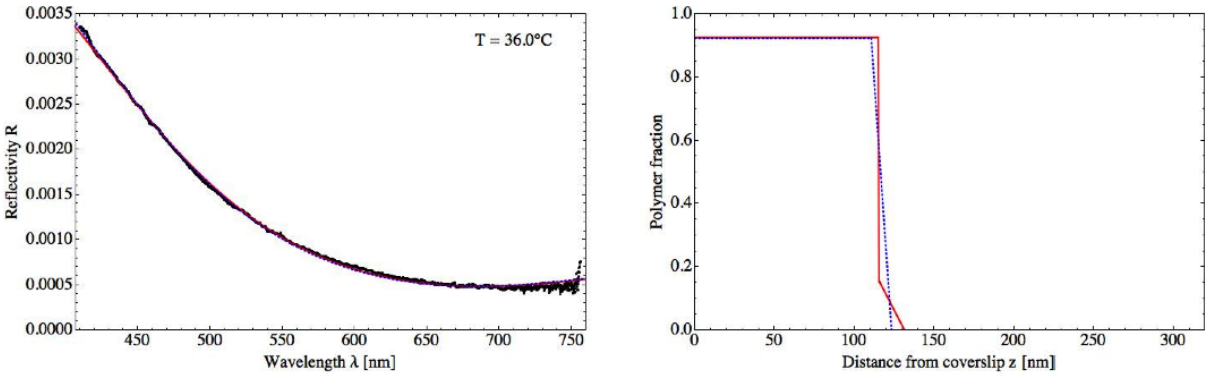

Figure 4.17: (a) experimental reflectivity data (black dots) corresponding to the HD4 brush at $T = 36°C$, along with their best fit obtained using a one phase profile (blue dotted line) and a two phase (red solid curve) profile. (b) corresponding density profiles obtained using a one phase profile (dotted blue) and two phase profile (solid red).

4.4.6 Density profiles at low temperatures and brush swelling

Far below the LCST, at temperatures $\sim 25°C$, we find that the reflectance curves cannot be properly captured using a $\phi(z)$ profile having a step-like shape or composed of a uniform density region topped by a single linear decay. Instead, the reflectance is accounted for by a more complex density profile having a decay composed essentially of two linear gradients. These two gradients are needed to fit the experimental reflectivity curves, as shown in figure 4.18A and B.

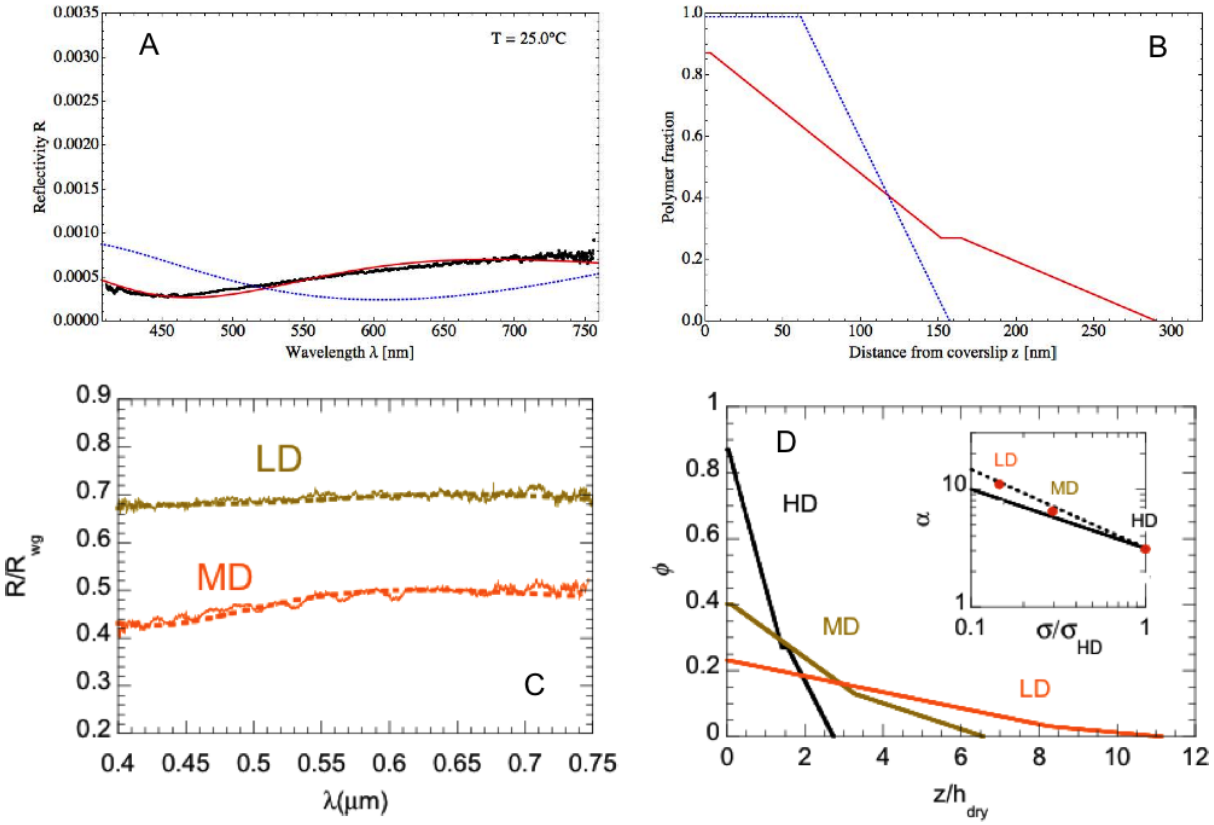

Figure 4.18: (A) experimental reflectivity data (black dots) corresponding brush HD4 at $T = 25°C$, compared to the best fit solutions obtained with a single-phase profile (blue dotted line) and a two-phase (red solid curve) profile. (B) corresponding one phase profile (dotted blue) and two phase profile (solid red). (C) experimental and best-fit reflectance spectra for the MD and LD brushes at 25°C. (D) density profiles obtained for the HD, MD, and LD brushes. The distance z to the substrate has been normalized by the h_{dry} for each brush. Inset: swelling ratio α as a function of grafting density (normalized by σ_{HD}) determined from the density profiles extracted from data fits (•). The dependence of α expected from eq. 4.22 is plotted for comparison for $\nu = 1/2$ (solid line) and $\nu = 3/5$ (dotted line). Images adapted from Varma *et al* [29].

Such features of the density profile were observed for all the brushes studied, and in particular also for MD and LD brushes of lower grafting density, as seen on figure 4.18C and D. Figure 4.18D shows that, for HD, MD and LD brushes, the density profiles display a similar double-gradient decay, and that, as the brush grafting density is decreased, the monomer volume fraction at the wall, ϕ_0, decreases, while the overall height of the brush h_{swell} (the distance z at which $\phi = 0$), normalized by the brush dry thickness, increases.

The above ratio, $\alpha = h_{swell}/h_{dry}$, corresponds to the swelling ratio of a brush, and quantifies the variation of the spatial extent of a brush between the good and poor solvent situations. As illustrated on figure 4.18D and summarized in table 4.2, we observe that α is consistently on the order of 3 for all HD brushes (having the same σ and different N), and increases to $\alpha \simeq 6.5$ for the MD brush and 11 for the LD brush. Such values of α for the HD and MD brushes are in qualitative agreement with those obtained from a previous experimental studies using surface force apparatus performed on samples of comparable grafting densities [12], as well as with recent numerical computations [32].

We now analyze the observed dependence of α on σ in the framework of a simple brush model proposed by Alexander and de Gennes [33, 34]. The model is based on the following assumptions (see figure 4.19):

- The chains are uncharged and non-adsorbing i.e not attracted to the substrate
- The chains, composed of N monomers, are uniformly stretched, having the free chain ends on top of the brush at height h
- The density profile of the brush ϕ is uniform (*i.e.* $\phi(z)$ is step-like)
- Each attached chain is described as a series of correlation blobs that do not overlap with each other, and whose size is set by the average distance between tethering points, $d = 1/\sqrt{\sigma}$.

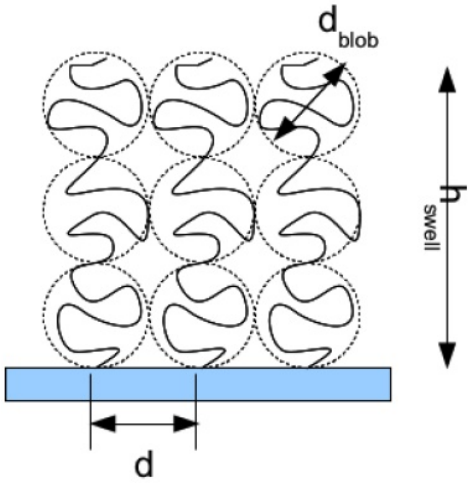

Figure 4.19: schematic showing a brush grafted onto substrates and described as blobs in the alexander de gennes picture.

The size of a blob is given by:

$$d_b = g^{\nu} a \tag{4.19}$$

where g is the number of monomers in a blob, a is the monomer size, and ν an exponent < 1 that will be specified below.

The height of a brush swollen in a solvent can thus be expressed as:

$$h_{swell} = n_b d_b \tag{4.20}$$

with n_b, the number of blobs per chain, equals N/g. Replacing $d_b = d$, n_b and g in equation 4.20 yields the following expression for h_{swell}:

$$h_{swell} = Na(\frac{d}{a})^{1-1/\nu} \tag{4.21}$$

The brush swelling ratio, $\alpha = h_{swell}/h_{dry}$, can then be computed, recalling that $h_{dry} = Na^3/d^2$:

$$\alpha = (\frac{d}{a})^{3-1/\nu} = \Big[\frac{1}{a(\sigma)^{1/2}}\Big]^{3-1/\nu} \tag{4.22}$$

Theoretical predictions for brushes immersed in a good solvent are based on $\nu = 3/5$, *i.e.* the blob size is that of isolated chain of g monomers obeying a Flory scaling. It has been found however, in experiments performed on brushes of high grafting densities, that a value of $\nu = 1/2$ describes more accurately the swelling data [35], suggesting that blobs are better described as gaussian entities.

We can already use the above framework to interpret our data regarding α:

- α values for all HD brushes are consistent with a value of around 3, indicating that brush swelling is independent of the chain length, as expected from equation 4.22.
- we find that α is larger for lower grafting densities, as qualitatively anticipated from equation 4.22. Moreover, from the theoretical prediction for α, we expect that an n-fold reduction of σ should induce a $n^{\frac{(3-\frac{1}{\nu})}{2}}$ fold increase of the swelling ratio. Starting from the average value of the swelling ratio for HD brushes ($\alpha \sim$3.1), and using the two limit values of ν (1/2 and 3/5), the swelling ratio of the MD brush, which is 3.5 times less dense, should thus lie in the range of 5.8-7.1, while α for the LD brush, whose density is 7 times lower than the HD sample, should have a value in the range 8.2-11.4. Indeed, the above scaling analysis is fully consistent with our measured values for the MD ($\alpha = 6.5$), and LD ($\alpha = 11$) brushes from the RICM experiments, as seen in figure 4.18D (inset).

4.4.7 Estimation of brush parameters

Our measurements of the brush swelling ratios are therefore in excellent agreement with the above theoretical scaling analysis. Moreover, using self-consistent field theory, Zhulina *et al* [36] have obtained, for a more realistic (parabolic) brush density profile, a relationship between h_{swell} and d that displays the same scaling as that of equation 4.22, and differs quantitalively from it by a prefactor of order 1. This has prompted us to use equation 4.22 to estimate the values of the molecular parameters σ and N for the various brushes studied.

For this, we employ relation 4.22 with $\nu = \frac{1}{2}$ and $a = 0.6$ nm[1] to compute σ_{HD} from α for the HD brushes. Using σ_{HD}, the number of monomers per chain, N, can be estimated from $h_{dry}\sigma = Na^3$. The grafting densities of the MD, and LD brushes are computed by dividing σ_{HD} respectively by 3.5 and 7, as suggested by ellipsometry measurements, and chain lengths can subsequently be estimated as before.

This procedure provides us with an estimation of the grafting density and chain length of the various brushes studied, as reported in Table 4.2. We also compute the Flory

[1]The monomer size a can be calculated using the relation $\rho = M_0/(N_A a^3)$ with ρ, the NIPAM monomer density = 0.95gcm^{-3}, M_0=113g mol^{-1}, and N_A the Avogadro's number.

radius(R_F) (radius of the unperturbed coil that the chains form in a free solution) and build the ratio of R_F to the average distance between grafting points d. As shown in table 2, this ratio is found to be larger than 1 for all the studied brush samples, both in swollen and collapsed state showing that the studied polymer layers exist in the brush regime at all the temperatures, including far above the LCST where water is a poor solvent.

Brush	$h_{dry}^{(a)}$ (nm)	$\alpha^{(b)}$	$\sigma^{(c)}$ (nm^{-2})	$N^{(d)}$	$\frac{R_F}{d}(e)$	$\frac{R_c}{d}(f)$
HD1	200	2.8	0.3	3100	41	4.8
HD2	167	3.2	0.3	2580	36	4.5
HD3	138	3.4	0.3	2130	33	4.2
HD4	108	2.75	0.3	1670	28	3.9
HD5	90	3	0.3	1390	25	3.7
HD6	70	2.95	0.3	1080	22	3.4
HD7	62	3.2	0.3	960	20	3.2
HD8	22	3.4	0.3	340	11	2.3
HD9	17	2.8	0.3	260	9	2.1
HD10	13	3.5	0.3	200	8	1.9
MD	40	6.5	0.088	2150	18	2.3
LD	29	11	0.045	3100	16	1.9

Table 4.2: Characteristics of PNIPAM brushes. (a) dry thickness measured by ellipsometry. (b) Swelling Ratio determined from reflectivity spectra at 25°C. (c) Grafting density estimated from equation 4.22, with ν=1/2 and an average swelling ratio of $\alpha = 3.1$ for all HD brushes. MD and LD densities estimated from their dry thicknesses compared to HD control wafers. (d) number of monomers per chain estimated from equation. (e) Ratio of the Flory radius $R_F = aN^{3/5}$ [34] and the estimated average distance between tethering points. (f) Ratio of the collapsed radius $R_c = aN^{1/3}$ [34] and the estimated average distance between tethering points.

4.4.8 Polydispersity in the brush

From the results shown on figure 4.18D, we observe that the experimental brush profiles deviate from the expected parabolic profiles predicted both by SCF theory [37] and simulation [38] under good solvent conditions. However, such predictions have been obtained for monodisperse brushes. As shown by self consistent field theory [37,39], such a parabolic shape is predicted to be lost when polydispersity is accounted for in the polymer brush. In the presence of polydispersity, the brush density profile, starting at the same monomer density at the wall, is predicted to adopt a concave shape that drops at $\phi = 0$ further away from the grafted surface [37,39], as illustrated in figure 4.20a.

In order to compare our profiles with those expected for monodisperse brushes, we compute parabolic profiles $\phi(z)=\phi_0(1-(\frac{z}{h_{swell}})^2)$ for the HD4, MD and LD brushes: these profiles have to satisfy the mass conservation constraint, namely $\int_0^{h_{swell}} \phi(z)dz = h_{dry}$, and start at the same ϕ_0 as that determined from fitting the experimental data. Under such conditions, the parabolic profiles are entirely determined without any free parameter. We compare the theoretical parabolic profiles with those determined from our modelling

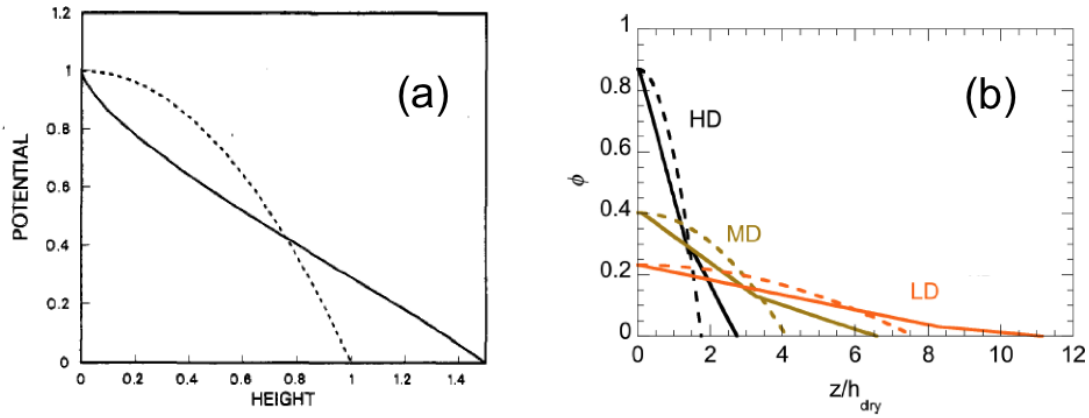

Figure 4.20: (a) SCF predictions of density profiles for a monodisperse (dotted line) and a polydisperse brush (solid line). Image taken from [37]. (b) Comparison of experimentally determined (solid lines) and computed parabolic (dotted line) profiles for HD4, MD and LD brushes. (Image adapted from Varma *et al* [29].)

on figure 4.20b. In agreement with the above-mentioned predictions, we observe that the $\phi(z)$ profiles we extract display the concave shape and the large-distance tail that characterize polydisperse brushes.

It can be seen from figure 4.20b that ϕ drops to 0 at a distance z larger than that of the parabolic decays. This means that the brushes swell more than expected for monodisperse chains, by about 50-60 percent for the three grafting densities ($\alpha^{poly}/\alpha^{mono}$ corresponding to 1.5-1.6 (figure 4.20b). The magnitude of such a polydispersity-induced overswelling is theoretically predicted to depend on the polydispersity index [39], which is defined as the ratio of the weight to number average molar mass of the chains M_w/M_n. From the simulation results obtained by de Vos *et al.* [39], who computed the amount of overswelling as a function of the brush polydispersity index, we estimate here that a 50-60% overswelling should correspond to M_w/M_n in the range 1.25-1.3.

As the measured swelling ratios for our polydisperse brushes are larger than for monodisperse brushes of the same σ and N, which is the assumption made in our Alexander-de Gennes analysis above, we conclude that we underestimate (using equation 4.22) σ by a factor of 2-2.5, and in turn overestimate N by the same factor.

4.4.9 Density profiles across the LCST: vertical phase separation

Finally, we describe the density profiles needed to account for the reflectance spectra at temperatures close to the LCST. As seen on figure 4.21a, the reflectance curves obtained experimentally at different temperatures are seen to be quantitatively described using our simple density model.

As the temperature of the solvent is increased towards the LCST, the following features emerge in the density profiles (figure 4.21b):

- A region having high and uniform segment density emerges close to the surface, and extends away from the substrate.
- The segment density profile $\phi(z)$ adopts a shape that indicates the presence of a

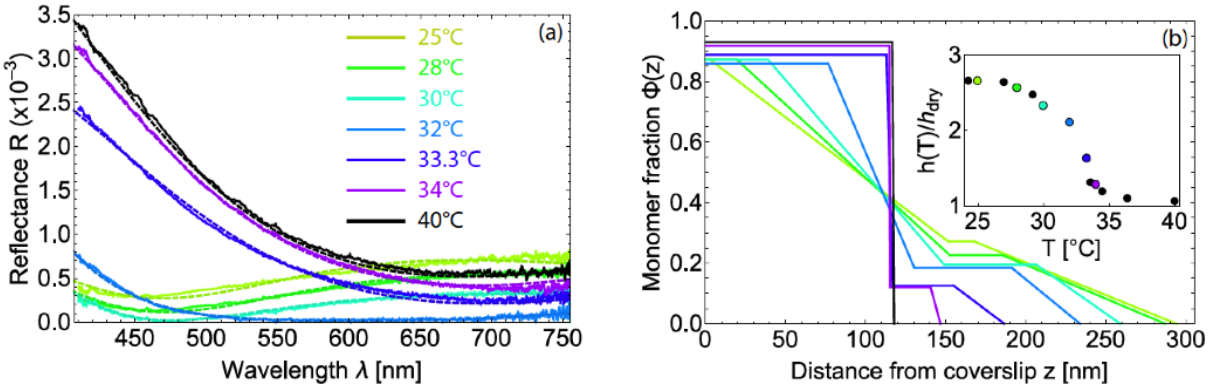

Figure 4.21: (a) Reflectance spectra from brush HD4 as a function of temperature. Solid lines are the measured spectra, dashed lines are the best fits obtained with the profiles displayed in (b). Inset, swelling ratio as a function of temperature, showing a marked transition around the LCST. Image adapted from Varma *et al* [29].

double decay in the density: a dense brush region is surmounted by a dilute brush region.

- The interface separating the dense and dilute regions becomes thinner and sharper.
- The distance from the substrate at which the segment density ϕ drops to zero, i.e. the brush height, can be seen to decrease as the temperature of the solvent is increased, as evident from the inset of figure 4.21b.

We thus find that, close to the LCST of the polymer, a two-phase profile is mandatory in order to account for the experimental reflectivity spectra. Such a feature is observed, at $T \simeq 32°C$, in the density profiles of all HD brushes with h_{dry} greater than 60 nm, as shown in figure 4.22.

For HD brushes with h_{dry} smaller than 20 nm, the reflectance curves are seen to be well fitted, over the whole temperature range, using a single-phase density profile. At temperatures close to the LCST, both the single- and two-phase profiles yield equally good fits (data not shown). We therefore cannot conclude on whether a two-phase profile exists at the LCST for the thinnest brushes investigated: while our spectral RICM technique allows us to quantitatively monitor the variations with T of the overall extension of PNIPAM brushes as thin as 13 nm, we believe that discriminating fine details in the vertical structure of such thin layers is beyond the sensitivity limit of the technique.

We can conclude, at this stage, that a double decay of the density profile, reminiscent of what has been obtained by neutron reflectivity (see figure 4.5 on page 80), is mandatory in order to describe accurately the measured reflectance spectra of the HD brushes, irrespective of chain length in the range $N = 1000 - 3000$.

A further support to such a vertical structuring upon collapse of PNIPAM brushes comes from the results obtained with MD and LD brushes. As shown on figure 4.23, these two brushes also display, around the LCST, a $\phi(z)$ profile exhibiting an inner phase of high and constant density surmounted by a much more dilute layer whose density gradually decays towards zero.

Interestingly, we note that while vertical phase separation could be clearly seen between 30 and 34°C for the HD brushes (figure 4.21b), this range is reduced to 32-34°C for the MD brush and to 33-34°C for the LD brush (figure 4.23). This shows that vertical

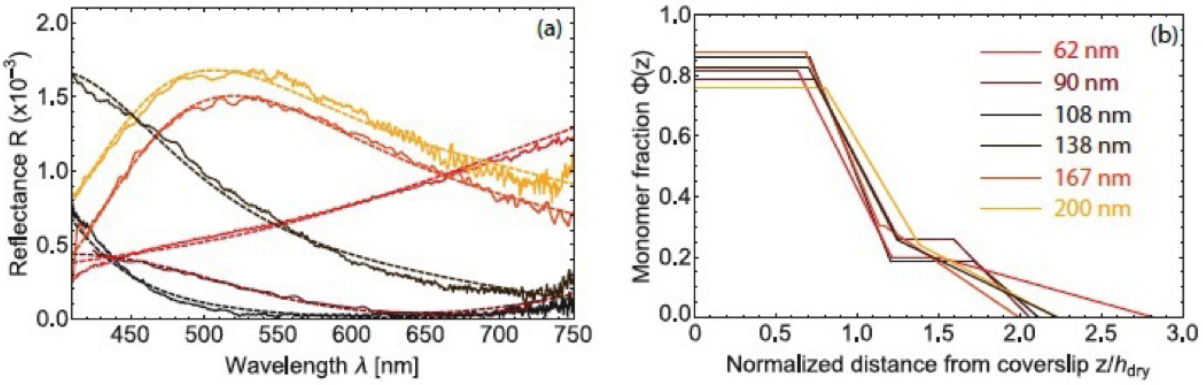

Figure 4.22: (a) reflectance spectra of brushes HD1, HD2, HD3, HD4, HD5, HD6, HD7 at 32°C(solid lines) and fits(dashed lines) with the two -phase profiles plotted in (b), showing a consistent phase separation for all six thicknesses. Brushes of smaller dry thicknesses do not appear on the figure as their potential separation cannot be resolved using the described set up. Image adapted from Varma *et al* [29].

structuring of the brushes is affected by the grafting density, and suggests that it may even disappear for low enough grafting densities.

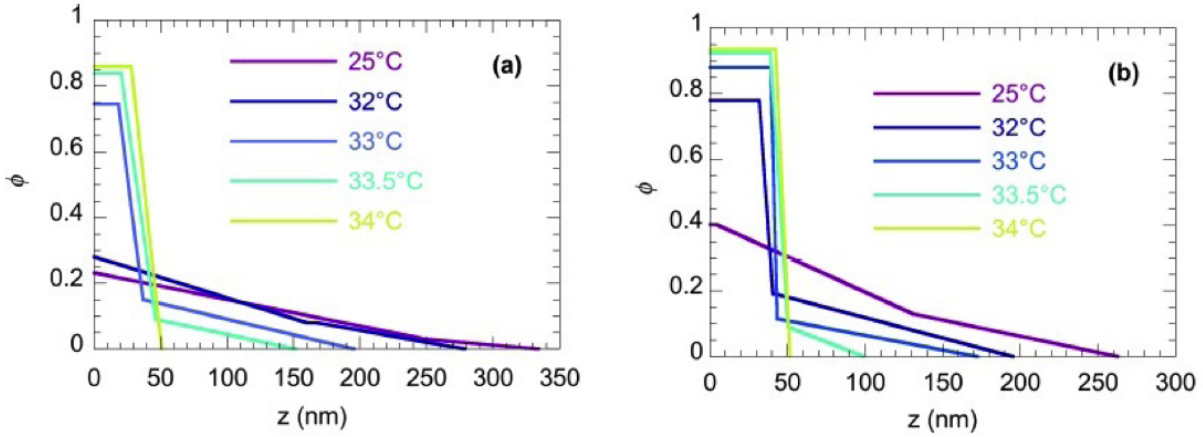

Figure 4.23: Density Profiles obtained from the reflectance spectra (not shown) as a function of temperature for (a) the low density brush and (b) the medium density brush. Adapted from Varma *et al* [29].

Overall, the above results and observations are qualitatively fully consistent with theoretical predictions regarding vertical phase separation in PNIPAM brushes. Indeed, Kroger and Halperin have recently shown [1], using self-consistent field theory incorporating the empirical $\chi_{eff}(\phi)$ determined by Afroze *et al* [21] (see page 78), that vertical phase separation should occur around the LCST in PNIPAM brushes, and that the temperature range in which such a phase separation exists gets narrower as the brush grafting density is decreased. This is shown on figure 4.24.

A more careful look at figure 4.24 however reveals that SCF theory predicts vertical phase separation to occur already around 27°C for high density brushes [1], while we observe that the two-phase profiles are found at temperatures greater than 30°C, as concluded also from neutron reflectometry studies [17,18]. This quantitative discrepancy could be attributed to the fact that the empirical χ_{eff} determined by Afroze [21], and used

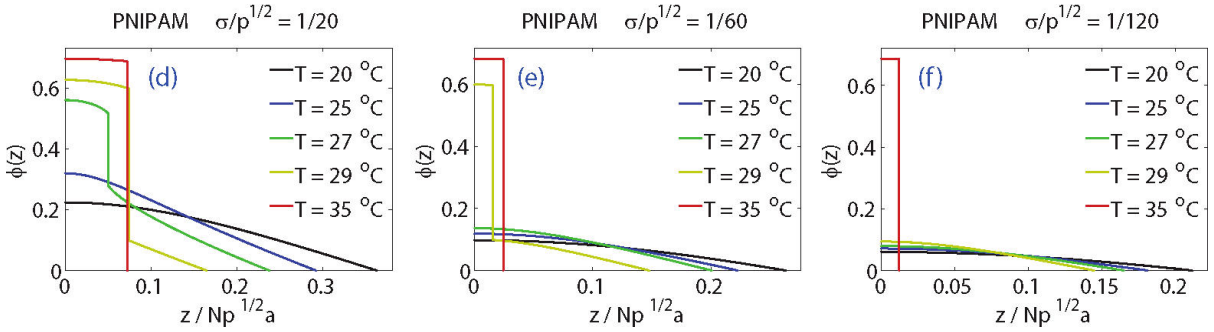

Figure 4.24: Theoretical PNIPAM brush density profiles computed by Kroger and Halperin at various temperatures. The brush grafting density decreases from left to right. Vertical phase separation is seen at 27 and 29°C for the highest σ (left panel), at 29°C only for the medium density (middle panel), and not seen for the lowest σ (right panel). Images taken from [1].

in SCF computations [1], accounts only semi-quantitatively for the PNIPAM/water phase diagram. These differences between theoretical and experimental observations raise the need to further extend the study of PNIPAM/water phase diagram in order to determine more accurately the ϕ-dependence of χ_{eff}. Alternatively, the present data obtained on brushes could be used to deduce $\chi_{eff}(\phi)$ from a confrontation with theoretical predictions.

4.4.10 Robustness of fits and comparison with other models

The results presented and discussed above have been obtained using the simple density model described in the Materials and Methods section on page 91. We discuss here the robustness of our fitting procedure, and the various assumptions made regarding the shape of the density profiles.

Fitting was achieved iteratively, starting from the collapsed (high temperature) spectrum for which initial trial values of the fit parameters can be obtained from the brush dry thickness. In order to ensure that the set of parameters yielding a quantitative fit of the data is unique, we compare systematically the quality of the fits obtained with one- and two-phase models. Far above the LCST, when the brush is fully collapsed, the two models, whose respective parameters are left free to vary, converge to the same best-fit solution that consists of a single step-like profile whose extension is in quantitative agreement with our independent ellipsometric measurement, as first illustrated on figure 4.17. This shows the uniqueness of the solution in the collapsed state, since modeling with 2 or 5 free parameters leads to similar profiles. The same strategy is applied at all temperatures: we systematically compare the fits obtained assuming a single-phase and a two-phase model, and show that, as discussed earlier, a two-phase model is mandatory in order to describe quantitatively the experimental data below and around the LCST. Once this has been identified, we further check, at selected temperatures below and at the LCST, that the profiles describing our data are indeed unique. This is done by calculating the reflectance spectrum with parameters spanning the whole range of values accessible under the physical constraints (volume fractions bounded in the range 0-1 and overall conservation of the monomer amount). We thus verify, by exploring the full parameter space, that there is only one profile that describes quantitatively the experimental data.

Fitting of spectral reflectances with the equations 4.15-4.18 relies on several modeling

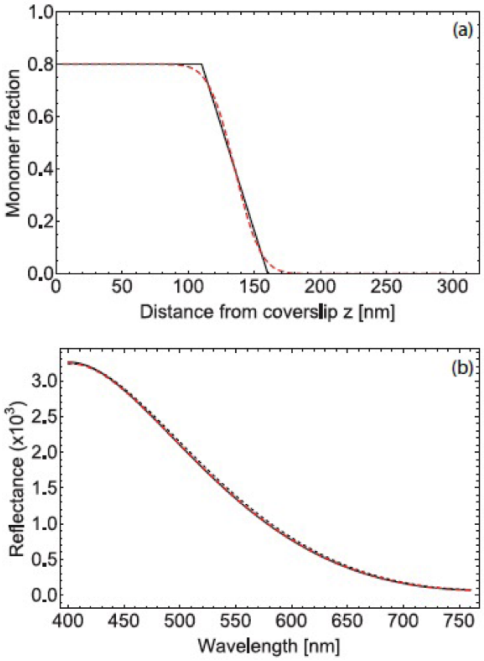

Figure 4.25: (a) we have used two one-phase profiles with identical amounts of monomer, only differing by their smoothness, to derive the spectral reflectance curves shown in (b) (black solid line and red dashed line). The straight-line profile was also used to calculate the exact reflectance without using the Born Approximation (Black dotted line in (b)). The three curves do not show any significant difference. Image adapted from Varma *et al* [29].

assumptions, in particular:

- The reflection coefficients of each infinitesimal layer are small enough to consider that light propagation through the sample is not affected by the reflected wave (Born approximation). We verified this point by comparing reflectance values derived from Eq. 4.15 to the exact numerical calculation, taking into account possible multiple reflections in the layers. Figure 4.25b shows that no significant difference was observed.

- The density profile of the brushes is described as a series of straight lines, while real profiles certainly exhibit smoother features. However, reflectance calculated from smoother profiles (erf functions) do not show differences with our simplified model, as seen on figure 4.25.

Moreover, we have compared the best fits obtained with our piecewise-linear model and with other analytical forms for the density profile, namely the parabolic and exponential decays that are frequently used to describe brushes. A comparison is given on figure 4.26, for the MD brush at temperatures below and at the LCST.

It can be seen that:

- our simplified model allows for excellent quantitative data fits while the two other profile shapes either miss (parabola) or only partially (exponential) reproduce the features of the reflectivity spectra,

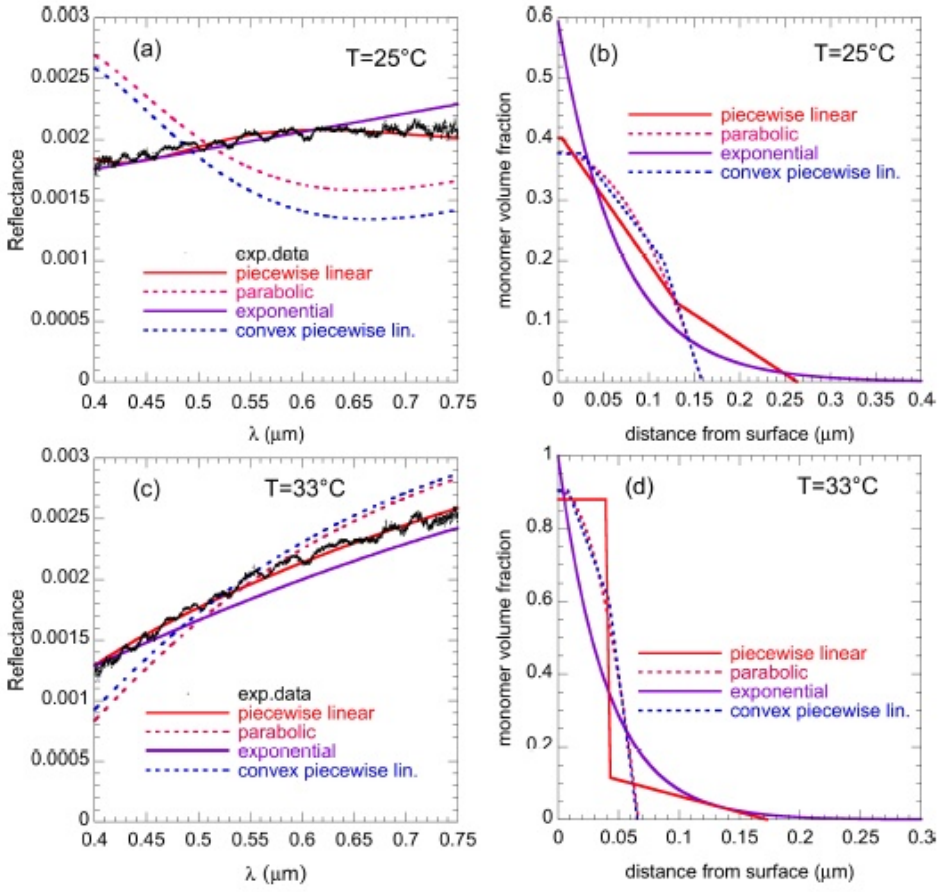

Figure 4.26: Experimental spectra obtained for the MD brush at 25°C (a) and 33°C(c) along with the best-fit spectra computed, as indicated on the panels, from an exponentially decaying profile($\phi(z) = \phi_0 \exp^{\frac{-z}{h}}$), a parabolic profile ($\phi(z) = \phi_0[1 - (\frac{z}{h})^2)$, a piecewise linear approximation of the parabola (convex piecewise linear) and our piecewise linear model. The rightmost panels show such profiles at 25°C(b) and 33°C(d). All profiles satisfy the conservation of monomer amount ($\int_0^\infty \phi(z)dz = h_{dry}$). Adapted from Varma *et al* [29].

- our simplified model can be used to approximate more complex density profiles, while retaining the important features of the reflectivity spectra, as shown on figure 4.26 and 4.25. This supports the fact that the density profiles obtained here are quantitatively reliable approximations of the actual density decay of the brushes, and that the quality of the fits would be only marginally enhanced by employing a higher number of segments to refine profile discretization, at the cost of a larger number of free parameters.

4.4.11 Hysteresis

Finally, we have probed the reversibility of the collapse/swelling transition of PNIPAM brushes with our spectral RICM technique.

As shown on figure 4.28, which provides, for the MD brush, the reflectance measured at $\lambda = 600$ nm during a heating/cooling cycle, we observe a hysteretic response of the brush between 31 and 34°C.

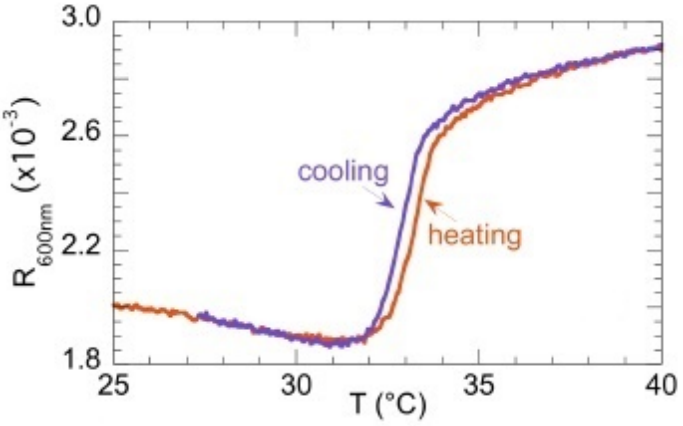

Figure 4.27: Reflectance for a MD brush, measured at a wavelength of 600 nm upon heating (red) and subsequent cooling (blue), illustrating the shift in the transition temperature. Adapted from Varma *et al* [29].

Such a behavior was observed for all the brushes that were used in our study. We have quantified the hysteresis in two different ways:

- From the reflectivity *vs* temperature curves measured at a given wavelength (figure 4.27), we compute the shift in temperature, ΔT, required in order to overlap the cooling curve with the heating curve in the transition region.

- We measure the difference between the two temperatures at which the reflectance spectra, upon heating and cooling, are identical over the whole spectral range. These two methods yielded consistent values for the temperature hysteresis ΔT.

In figure 4.28(a), ΔT is plotted as a function of the brush dry thickness h_{dry}, for the various HD, MD and LD brushes. It can be seen that below a threshold in thickness of h_{dry} $\sim$15nm, no hysteresis is observed. Above this threshold, as h_{dry} increases, the hysteresis increases from 0.3 upto 0.75°C. Furthermore, we observe that the MD and LD brushes show higher results on the $\Delta T(h_{dry})$ plot as compared to the HD samples. From these observations, we conclude that the magnitude of the hysteresis cannot be simply controlled by h_{dry}, i.e. the observed hysteresis does not only depend on the amount of monomer bound to the surface.

In order to clarify which parameter influences the hysteresis, we have plotted ΔT as a function of the average number of monomers per chain (N, as determined previously from the swelling ratio) for each brush, as shown in figure 4.28(b). Doing so, we observe that the results for the LD and MD samples are horizontally shifted and closely follow the ΔT plots as seen for the HD brushes.

Overall, it can be seen that below a threshold in chain length, no hysteresis is observed, while above this threshold, ΔT increases with N, independently of the brush grafting density. These results indicate that the observed hysteresis is essentially governed by the length of the grafted chains.

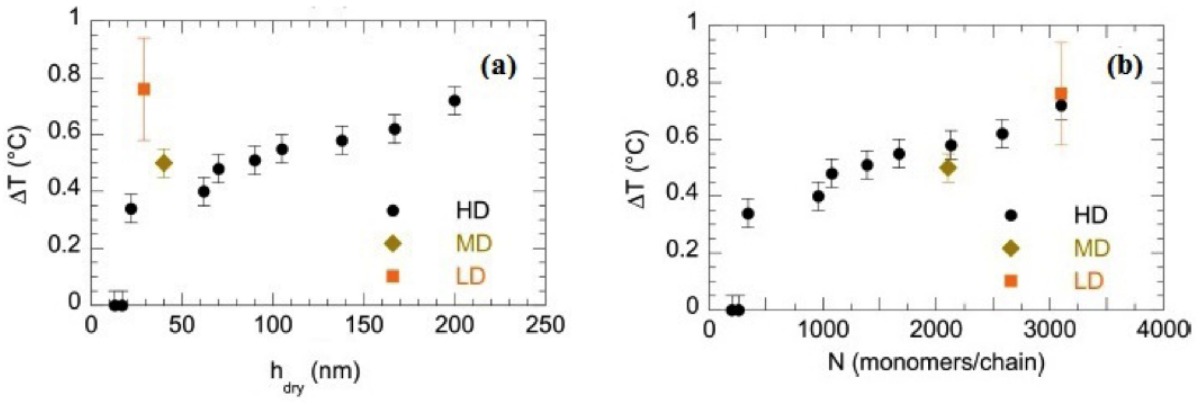

Figure 4.28: Hysteresis amplitude ΔT is plotted for the brushes listed in Table 1 as a function of (a), their dry thickness h_{dry} and (b), the chain length. Error bars in (b) and (c) are estimated for the dispersion of the mesaured values of ΔT at different temperatures and different wavelengths. Image taken from Varma *et al* [29].

Physical origins of hysteresis

Hysteresis in the thermal response of PNIPAM brushes has already been reported in several previous works using SPR and QCM. Two possible mechanisms have been proposed in these previous studies in order to explain such a hysteresis [4–8].

- Inter monomer hydrogen bonding: in the collapsed brush state, the formation of inter-monomer hydrogen bonds may act as transient crosslinks that must be disrupted upon reswelling of the chains. This mechanism has been suggested from experiments on PNIPAM chains in solutions [40].

- Entanglements: the presence of entanglements create topological constraints that limit the extent of chain swelling, and thus delay the swelling kinetics as the temperature is decreased across the LCST.

Both mechanism have been proposed on a qualitative basis, and no systematic studies of hysteresis as a function of brush parameters have yet allowed discrimination between the two. For the present study, we tried to understand our experimental results by supporting one of these mechanisms.

The presence of H-bonds "crosslinks" As per to the first mechanism, hysteresis in PNIPAM chains is expected to arise due to the difference in energy barrier between the collapse and swelling processes. If inter-monomer H-bonds were solely responsible for hysteresis, ΔT should be directly proportional to the amount of monomers, i.e. h_{dry}, and smoothly vanish to zero as h_{dry} tends to zero, in contrast to the threshold observed in our data (figure 4.28(a)). Moreover, such a mechanism cannot account for the larger hysteresis observed for low graftig densities for the same h_{dry} i.e. for the same amount of monomers, as seen in HD brushes. Hence, we rule out inter-monomer crossliking to be the reason behind the observed hysteretic behaviour.

The presence of entanglements This mechanism has a kinetic origin in which the hysteresis is mainly governed by the time required to relax the topological constraints

due to entanglements compared to the time scale at which the temperature is decreased. In our study, we find such a mechanism to be fully consistent with our results, as we now detail.

In polymeric systems, surrounding chains impose topological constrains on each other as they cannot cross. Although a clear picture of an entanglement is elusive, it can be assumed as a possible knot between two neighbouring chains in an overlapping situation (figure 4.29(a)). The collective efforts of surrounding chains on a random strand is to restrict its motion into a tube like region (figure 4.29(b)) where each monomer is effectively confined by a constraining potential in the tube with the primitive path as its centre. The tube comprises of N_e number of entangled strands of size a [20].

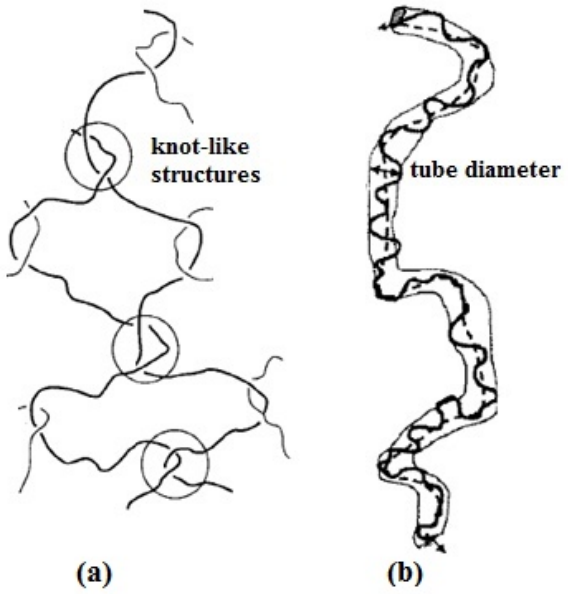

Figure 4.29: (a) The crossing over of two chains leading to the formation of an entanglement. (b) A random chain topologically constrained into a tube like region by the surrounding chains [20].

These entanglements form only when the polymer chains are longer than a critical length N_c (or, equivalently, have a molecular mass larger than the critical mass for entanglement, M_c). This is consistent with the experimental studies showing the dependence of the viscosity of polymeric melts on the chain molecular mass, wherein deviation from the entangled regimes was observed for polymeric chains having molar mass less than M_c.

Such a critical length accounts for the observed threshold in the $\Delta T(N)$ curve shown in figure 4.28(b). More precisely, we find this threshold to be around N_c=300 monomers/chain. Accounting, as discussed in the section dedicated to the effect of brush polydispersity on page 97, for a possible over-estimation of N by a factor of $\sim$ 2, we consider that N_c, determined from our hysteresis measurements, lies in the range of 150-300. This leads to a critical mass M_c=$N_c M_0$ in the range 17-34 $kg.mol^{-1}$, which covered the reported value of PNIPAM entanglement mass of $23kg.mol^{-1}$ [41].

Increasing the density of entanglements in a semi-dilute solution of linear chains is known to slow down their relaxation [42]. It can thus be expected that increasing the density of entanglements within a brush will delay further its re-swelling, thereby yielding

a larger apparent hysteresis at a given rate of temperature change. This is in agreement with our results showing that ΔT is larger for longer chains, for which the number of entanglements per chain increases.

Time scale of relaxation As a further validation step, we have compared the lifetime of entanglements with the time scale of temperature change in our experiments. τ_{exp} represents the time required to change the temperature of the solution by about 1°C around the transition. We fixed the rate of temperature decrease to $\sim$0.15°C.min^{-1} in all our experiments, yielding $\tau_{exp} \sim$ 400s. The lifetime of entanglements, on the other hand, depends on the relaxation mechanism by which the constraints are released. In the case of free linear chains in a solution or a melt, the entanglement dynamics is controlled by the diffusion of the molecules along its tube, by a process known as reptation. However, for tethered chains attached to a fixed site, reptation is suppressed and the only process by which they can relax entanglements is through an arm-retraction mechanism. Such a mechanism, known to govern the dynamics of star or branched polymers [43], describes the fact that a chain having one end fixed in space can escape the tube formed by its neighbours only by retracting a part, or all of its length, along this tube. This occurs at the cost of a large entropic penalty and a low probability of occurrence, such that the relaxation time of a tethered chain grows exponentially with the number of entanglements per chains [43–45]. Thus, the retraction time for a chain having N monomers is given by [44, 44]:

$$\tau_{arm}(s) \sim \tau_0 N^2 \exp(\mu s^2 N/N_e) \tag{4.23}$$

where $\tau_{arm}(s)$ is the time to retract a fraction s ($0 \leq s \leq 1$) of the chain made of a total of N units along the tube length, and $N_e = M_c/(2M_0) \sim 100$ (It was considered that N_e is approximately half of N_c, as suggested from rheology studies on polymer melts, with M_c =23kgmol^{-1}). The constant $\mu \sim$15/8, and the pre-exponential time $\tau_0 N^2$ is the Rouse time of the equivalent "free" chain [44, 45]. From the works of Yuan *et al* [42], we can estimate the rouse time of PNIPAM chains of length N$\approx$ 1800 units in solution in water at 25°C to be of the order of 6×10^{-3}s.

Thus, we can estimate that, for N$\approx$1800, $\tau_{arm}(s)$ is comparable to or larger than $\tau_{exp} \sim$ 400s for any s $\geq$ 0.55, and reaches upto 10^{12} s for full chain retraction (s=1). This estimate is only in terms of the order of magnitude, as the value of μ or the exact pre-exponential factor are not firmly established [20, 45] (we have used a Rouse time determined at room temperature, whereas the pre-exponential time might actually be much larger since the chain dynamics above the LCST is supposed to be significantly slower). However, such an analysis allows us to conclude that:

- Entanglements relaxed by arm-retraction indeed have a lifetime that is comparable to the experimental time scale.
- The observed hysteresis most likely results from the entanglements that are relaxed by sub-chain rearrangements at the proper lengthscale (i.e. involving s such that $\tau_{arm}(s) \approx \tau_{exp}$).

Overall, our results along with their analysis strongly support the fact that the hysteretic response of our PNIPAM brushes has essentially a kinetic origin, and arises from

the long-lived entanglements that delay swelling, as proposed theoretically in the description of the swelling dynamics of collapsed globules [46].

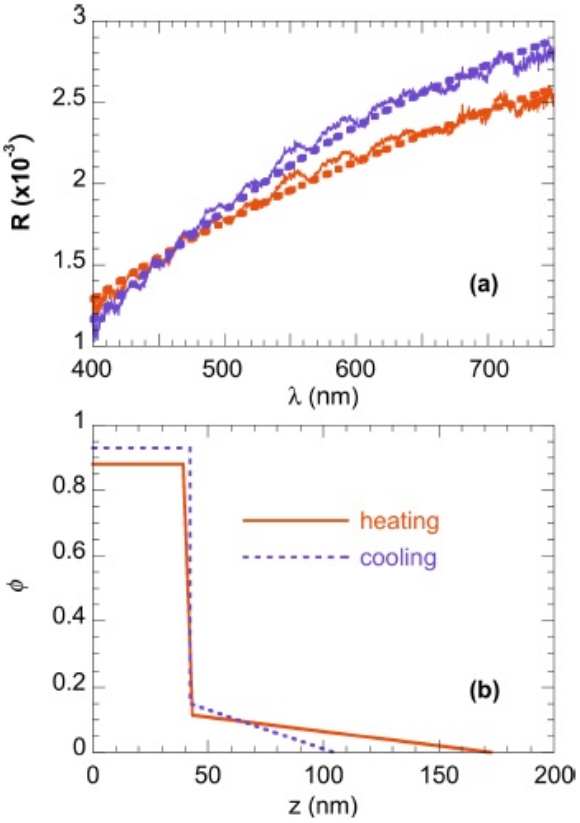

Figure 4.30: (a) Spectral Reflectance and (b) extracted density profiles of the medium density brush at 33°C upon heating and cooling. Image adapted from Varma *et al* [29].

We close this chapter by recalling that upon heating across the LCST, PNIPAM brushes display a non-uniform density profile exhibiting a dense phase close to the grafted substrate, surmounted by a more dilute layer. Our analysis of the reflectivity spectra measured during cooling also leads to similar non-uniform density profiles, as illustrated in figure 4.30 for the MD brush. A remarkable point is that when comparing the profiles extracted from a fit of the spectra measured at the same temperature, in the hysteresis region, we observe that a brush displays a denser inner region and a less extended outer layer when cooled (figure 4.30(b)). This is in good agreement with the above picture describing hindered swelling of the brushes upon cooling. Such a result provide the first direct experimental evidence that a brush exhibits two different non-uniform structures when crossing the LCST from the swollen and from the collapsed state, in agreement with qualitative pictures proposed in previous works on brushes [8] or globules [40].

4.5 Conclusion

I have describe an original optical set up based on Reflection Interference Contrast Microscopy, employed to characterize PNIPAM brushes. Spectral RICM performed over the

visible spectrum provides detailed information regarding the thickness, density, and vertical structure of PNIPAM polymer brushes in water. RICM allows us to obtain a fast and in-depth characterization of the brushes. Thus, the technique offers significant advancements over Neutron Reflectivity and Spectral Ellipsometry techniques. The important features of the technique are:

- The optical set-up is based on a microscope that enables easy combination with other imaging techniques.
- RICM allows spatially-resolved reflectance measurements, that allows us to map possible thin film heterogeneities.
- The measurements are performed onto transparent glass substrates, whereas NR and SE require opaque silicon wafer substrates. This allows for direct *in situ* characterization of the brushes, that can then be used for the target biological applications, which typically require transparent substrates for microscopy.

We have applied the spectral RICM to study the effect of molecular parameters on the thermal response of PNIPAM brushes. The reflectivity changes measured over the brush surface yield information about the non-homogeneous structural changes in PNIPAM brushes as a function of the solvent quality, and our analysis provides one of the very few evidence for vertical phase separation in PNIPAM brushes.

Moreover, RICM has allowed shedding light on the physical mechanism underlying the hysteretic response of PNIPAM brushes upon cycling in temperature. The hysteretic response of the brush is observed to have a kinetic in origin. It arises from the interchain entanglements that delay the brush re-swelling process.

Finally, RICM comes as an interesting alternative approach to characterize polymer brushes in terms of their length, grafting density and polydispersity. Indeed, the characterization of "grafted-from" brushes, in terms of grafting density and molecular weight, is a challenging task [47], even though their synthesis is easy. A promising method to characterize such polymer brushes is chromatography, that involves degrafting the tethered chains from the surface and subsequently analysing their size and distribution [48]. Herein, a large amount of polymer sample is required in order to perform an accurate solution characterization. This process is hence better suited for brushes grafted on substrates having large specific surfaces. Alternatively, polymerization can be performed, in parallel with brush growth, using free initiator in solution [35]. This strategy assumes that polymerization in the bulk and from the surface obeys the same kinetics. However, such an assumption has been shown to break down [49] due to surface-induced crowding [50] and termination effects [51]. X-ray photoelectron spectroscopy is also used in order to determine the surface coverage of polymerization initiator, but relies on an assumption regarding the fraction of initiator that actually leads to chain growth [52]. These various means for determining the molecular parameters of grafted-from brushes pose limitations in terms of ease of use or quantitative reliability. In this context, the analysis from RICM comes as an interesting approach for brush characterization, as it provides a direct *in situ* evaluation of the brushes without the need for additional bulk solution measurements or removing the grafted brushes from their substrate. Doing so, we can estimate not only σ and N, but also the polydispersity index and the errors associated with the assumption on which the present analysis relies.The utility of RICM lies in the fact that it allows for an *in situ* and non-destructive characterization of brushes that overcome many of the limitations encountered with other characterization methods.

Bibliography

[1] A. Halperin and M. Kröger, "Collapse of thermoresponsive brushes and the tuning of protein adsorption", *Macromolecules* **44**(17), pp. 6986–7005 (2011).

[2] Changying Xue, Byun-Chan Choi, Sangwook Choi, Paul V Braun, and Deborah E Leckband, "Protein adsorption modes determine reversible cell attachment on poly (n-isopropyl acrylamide) brushes", *Advanced Functional Materials* **22**(11), pp. 2394–2401 (2012).

[3] A. Halperin and M. Kroger, "Theoretical considerations on mechanisms of harvesting cells cultured on thermoresponsive polymer brushes", *Biomaterials* **33**(20), pp. 4975 – 4987 (2012).

[4] S Balamurugan, Sergio Mendez, Sreelatha S Balamurugan, Michael J O'Brie, and Gabriel P López, "Thermal response of poly (n-isopropylacrylamide) brushes probed by surface plasmon resonance", *Langmuir* **19**(7), pp. 2545–2549 (2003).

[5] Guangzhao Zhang, "Study on conformation change of thermally sensitive linear grafted poly (n-isopropylacrylamide) chains by quartz crystal microbalance", *Macromolecules* **37**(17), pp. 6553–6557 (2004).

[6] Masahiko Annaka, Chie Yahiro, Kenichi Nagase, Akihiko Kikuchi, and Teruo Okano, "Real-time observation of coil-to-globule transition in thermosensitive poly (n-isopropylacrylamide) brushes by quartz crystal microbalance", *Polymer* **48**(19), pp. 5713–5720 (2007).

[7] Guangzhao Zhang and Chi Wu, "Quartz crystal microbalance studies on conformational change of polymer chains at interface", *Macromolecular rapid communications* **30**(4-5), pp. 328–335 (2009).

[8] Guangming Liu and Guangzhao Zhang, "Collapse and swelling of thermally sensitive poly (n-isopropylacrylamide) brushes monitored with a quartz crystal microbalance", *The Journal of Physical Chemistry B* **109**(2), pp. 743–747 (2005).

[9] Naoyuki Ishida and Simon Biggs, "Direct observation of the phase transition for a poly (n-isopropylacryamide) layer grafted onto a solid surface by afm and qcm-d", *Langmuir* **23**(22), pp. 11083–11088 (2007).

[10] Naoyuki Ishida and Simon Biggs, "Effect of grafting density on phase transition behavior for poly (n-isopropylacryamide) brushes in aqueous solutions studied by afm and qcm-d", *Macromolecules* **43**(17), pp. 7269–7276 (2010).

[11] Kyle N Plunkett, Xi Zhu, Jeffrey S Moore, and Deborah E Leckband, "Pnipam chain collapse depends on the molecular weight and grafting density", *Langmuir* **22**(9), pp. 4259–4266 (2006).

[12] Ibrahim B Malham and Lionel Bureau, "Density effects on collapse, compression, and adhesion of thermoresponsive polymer brushes", *Langmuir* **26**(7), pp. 4762–4768 (2010).

[13] Satoru Kidoaki, Shoji Ohya, Yasuhide Nakayama, and Takehisa Matsuda, "Thermoresponsive structural change of a poly (n-isopropylacrylamide) graft layer measured with an atomic force microscope", *Langmuir* **17**(8), pp. 2402–2407 (2001).

[14] Naoyuki Ishida and Mikio Kobayashi, "Interaction forces measured between poly (n-isopropylacrylamide) grafted surface and hydrophobic particle", *Journal of colloid and interface science* **297**(2), pp. 513–519 (2006).

[15] Edmondo M Benetti, Szczepan Zapotoczny, and G Julius Vancso, "Tunable thermoresponsive polymeric platforms on gold by photoiniferter-based surface grafting", *Advanced Materials* **19**(2), pp. 268–271 (2007).

[16] H Yim, MS Kent, S Mendez, SS Balamurugan, S Balamurugan, GP Lopez, and S Satija, "Temperature-dependent conformational change of pnipam grafted chains at high surface density in water", *Macromolecules* **37**(5), pp. 1994–1997 (2004).

[17] H Yim, MS Kent, S Mendez, GP Lopez, S Satija, and Y Seo, "Effects of grafting density and molecular weight on the temperature-dependent conformational change of poly (n-isopropylacrylamide) grafted chains in water", *Macromolecules* **39**(9), pp. 3420–3426 (2006).

[18] H Yim, MS Kent, S Satija, S Mendez, SS Balamurugan, S Balamurugan, and GP Lopez, "Evidence for vertical phase separation in densely grafted, high-molecular-weight poly (n-isopropylacrylamide) brushes in water", *Physical Review E* **72**(5), pp. 051801 (2005).

[19] E Stefan Kooij, Xiaofeng Sui, Mark A Hempenius, Harold JW Zandvliet, and G Julius Vancso, "Probing the thermal collapse of poly (n-isopropylacrylamide) grafts by quantitative in situ ellipsometry", *The Journal of Physical Chemistry B* **116**(30), pp. 9261–9268 (2012).

[20] R. H. Rubinstein, M.; Colby, *Polymer Physics*, Oxford University Press (2003).

[21] F Afroze, E Nies, and H Berghmans, "Phase transitions in the system poly(n-isopropylacrylamide)/water and swelling behaviour of the corresponding networks", *Journal of Molecular Structure* **554**(1), pp. 55– 681 (2000).

[22] Vladimir A Baulin, Ekaterina B Zhulina, and Avi Halperin, "Self-consistent field theory of brushes of neutral water-soluble polymers", *The Journal of chemical physics* **119**(20), pp. 10977–10988 (2003).

[23] VA Baulin and A Halperin, "Concentration dependence of the flory χ parameter within two-state models", *Macromolecules* **35**(16), pp. 6432–6438 (2002).

[24] Vladimir A Baulin and Avi Halperin, "Signatures of a concentration-dependent flory χ parameter: Swelling and collapse of coils and brushes", *Macromolecular theory and simulations* **12**(8), pp. 549–559 (2003).

[25] Vladimir A Baulin, Ekaterina B Zhulina, and Avi Halperin, "A self-consistent field theory of brushes of neutral water-soluble polymers", *The Journal of chemical physics* **119**(20), pp. 10977–10988 (2003).

[26] Markus Biesalski, Jürgen Rühe, and Diethelm Johannsmann, "Segment density profiles of polyelectrolyte brushes determined by fourier transform ellipsometry", *The Journal of chemical physics* **111**(15), pp. 7029–7037 (1999).

[27] A. Halperin, M. Kröger, and F. M. Winnik, "Poly(n-isopropylacrylamide) phase diagrams: Fifty years of research", *Angew. Chem. Int. Ed.* **54**, pp. 15342–15367 (2015).

[28] Laurent Limozin and Kheya Sengupta, "Quantitative reflection interference contrast microscopy (ricm) in soft matter and cell adhesion", *ChemPhysChem* **10**(16), pp. 2752–2768 (2009).

[29] S Varma, L Bureau, and D Debarre, "The conformation of thermoresponsive polymer brushes probed by optical reflectivity", *Langmuir* **32**, pp. 3152–3163 (2016).

[30] Delphine Débarre and Emmanuel Beaurepaire, "Quantitative characterization of biological liquids for third-harmonic generation microscopy", *Biophysical journal* **92**(2), pp. 603–612 (2007).

[31] http://refractiveindex.info?/shelf=glass&book=BK7&page=SCHOTT.

[32] Fabien Leonforte and Marcus Muller, "Poly (n-isopropylacrylamide)-based mixed brushes: A computer simulation study", *ACS applied materials & interfaces* **7**(23), pp. 12450–12462 (2015).

[33] S Alexander, "Polymer adsorption on small spheres. a scaling approach", *Journal de Physique* **38**(8), pp. 977–981 (1977).

[34] P. G. de Gennes, "Conformations of polymers attached to an interface", *Macromolecules* **13**(5), pp. 1069–1075 (1980).

[35] Shinpei Yamamoto, Muhammad Ejaz, Yoshinobu Tsujii, and Takeshi Fukuda, "Surface interaction forces of well-defined, high-density polymer brushes studied by atomic force microscopy. 2. effect of graft density", *Macromolecules* **33**(15), pp. 5608–5612 (2000).

[36] EB Zhulina, OV Borisov, VA Pryamitsyn, and TM Birshtein, "Coil-globule type transitions in polymers. 1. collapse of layers of grafted polymer chains", *Macromolecules* **24**(1), pp. 140–149 (1991).

[37] ST Milner, TA Witten, and ME Cates, "Effects of polydispersity in the end-grafted polymer brush", *Macromolecules* **22**(2), pp. 853–861 (1989).

[38] DI Dimitrov, A Milchev, and K Binder, "Polymer brushes in solvents of variable quality: molecular dynamics simulations using explicit solvent", *The Journal of chemical physics* **127**(8), pp. 084905 (2007).

[39] Wiebe M de Vos and Frans AM Leermakers, "Modeling the structure of a polydisperse polymer brush", *Polymer* **50**(1), pp. 305–316 (2009).

[40] He Cheng, Lei Shen, and Chi Wu, "Lls and ftir studies on the hysteresis in association and dissociation of poly (n-isopropylacrylamide) chains in water", *Macromolecules* **39**(6), pp. 2325–2329 (2006).

[41] http://polymerdatabase.com/polymer/polyn-ispopropylacrylamide.html.

[42] Guangcui Yuan, Xiaohong Wang, Charles C Han, and Chi Wu, "Reexamination of slow dynamics in semidilute solutions: From correlated concentration fluctuation to collective diffusion", *Macromolecules* **39**(10), pp. 3642–3647 (2006).

[43] Dale S Pearson and Eugene Helfand, "Viscoelastic properties of star-shaped polymers", *Macromolecules* **17**(4), pp. 888–895 (1984).

[44] Daniel A Vega, Leopoldo R Gómez, Leandro E Roth, Jorge A Ressia, Marcelo A Villar, and Enrique M Vallés, "Arm retraction potential of branched polymers in the absence of dynamic dilution", *Physical review letters* **95**(16), pp. 166002 (2005).

[45] Armand Adjari, Françoise Brochard-Wyart, Pierre-Gilles de Gennes, Ludwik Leibler, Jean-Louis Viovy, and Michael Rubinstein, "Slippage of an entangled polymer melt on a grafted surface", *Physica A: Statistical Mechanics and its Applications* **204**(1-4), pp. 17–39 (1994).

[46] Nam-Kyung Lee, Cameron F Abrams, A Johner, and S Obukhov, "Swelling dynamics of collapsed polymers", *Macromolecules* **37**(2), pp. 651–661 (2004).

[47] Raphael Barbey, Laurent Lavanant, Dusko Paripovic, Nicolas Schuwer, Caroline Sugnaux, Stefano Tugulu, and Harm-Anton Klok, "Polymer brushes via surface-initiated controlled radical polymerization: synthesis, characterization, properties, and applications", *Chemical reviews* **109**(11), pp. 5437–5527 (2009).

[48] Rohan R Patil, Salomon Turgman-Cohen, Jirí Srogl, Douglas Kiserow, and Jan Genzer, "On-demand degrafting and the study of molecular weight and grafting density of poly (methyl methacrylate) brushes on flat silica substrates", *Langmuir* **31**(8), pp. 2372–2381 (2015).

[49] Chengjun Kang, Rowena Crockett, and Nicholas D Spencer, "The influence of surface grafting on the growth rate of polymer chains", *Polymer Chemistry* **7**(2), pp. 302–309 (2016).

[50] Christopher B Gorman, Randall J Petrie, and Jan Genzer, "Effect of substrate geometry on polymer molecular weight and polydispersity during surface-initiated polymerization", *Macromolecules* **41**(13), pp. 4856–4865 (2008).

[51] Jan Genzer, "In silico polymerization: Computer simulation of controlled radical polymerization in bulk and on flat surfaces", *Macromolecules* **39**(20), pp. 7157–7169 (2006).

[52] Changying Xue, Nihan Yonet-Tanyeri, Nicolas Brouette, Michele Sferrazza, Paul V Braun, and Deborah E Leckband, "Protein adsorption on poly (n-isopropylacrylamide) brushes: dependence on grafting density and chain collapse", *Langmuir* **27**(14), pp. 8810–8818 (2011).

Chapter 5

Dually-responsive polymers: synthesis and characterization

5.1 Abstract

In the current chapter, I first introduce the structural concepts of azobenzene that are relevant to the formation of responsive polymers. I then report the synthesis of azobenzene based dually responsive poly(DMA-AZAA) copolymers and poly(DMA-NIPAM-AZAA) terpolymers via free radical polymerization and ARGET-ATRP protocol respectively. The synthesized polymers are characterized in terms of temperature and light induced changes in solution properties. I show that the synthesized poly(DMA-NIPAM-AZAA) terpolymer exhibits tuneable properties at temperatures close to the physiological temperature of 37°C, which makes it a good candidate for future use in applications related to the spatial control of cell adhesion.

5.2 Introduction

In the previous chapters, we focused on brushes made up of PNIPAM that were used to pattern proteins and to perform a detailed structural characterization. The thermoresponsive nature of PNIPAM brushes, along with their conformational changes across the LCST, forms the basis for a range of applications, for instance, the control of protein adsorption and cell release [1].

As a stimulus, temperature is usually applied at a macroscopic scale and is challenging to control for applications that require a good spatial resolution on a surface. The applications of polymer brushes for the control of cell adhesion, especially at the single cell level, call for responsive polymers whose conformation can be changed by applying a stimulus that can be controlled in space and time. Moreover, the design of responsive polymers for biological applications has to take into account that the change in their conformation needs to occur close to physiological temperature, where the cells are the most active, and that the applied stimulus must not be harmful to the cells. To achieve these objectives, it is appealing to use light as a trigger [2]. Thus, we chose to design light responsive polymers, which can change conformation upon irradiation at a particular wavelength.

Light-induced conformational changes are most often obtained by using dually responsive polymers. A general strategy to design such macromolecules involves introducing a photochromic molecule into a temperature-responsive polymeric system [3]. The conformational change of such polymers is thus expected to depend on the isomerization of the photochromic species. Many dually responsive polymers have been designed previously, and for the present study we focus only on a specific type, having azobenzene as the photoresponsive moieties. Azobenzene is chosen for the following reasons:

- Thermal and chemical stability and ability to graft on diverse polymeric chains in a robust fashion [3].
- A very fast light triggered isomerization with excellent reversibility [4, 5].

The details of functional group transformations and the factors influencing these changes are more evident by studying the photochemistry and electronic spectra of the azo derived species.

5.2.1 The photo-isomerization of azobenzene

Aromatic azobenzene compounds exist in two interconvertible *trans* and *cis* states. The almost coplanar structure of the former state is resonance stabilized as a result of conjugation between the atoms leading to higher stability as compared to the latter form that has phenyl rings rotated out of the plane [6] (figure 5.1(a)).

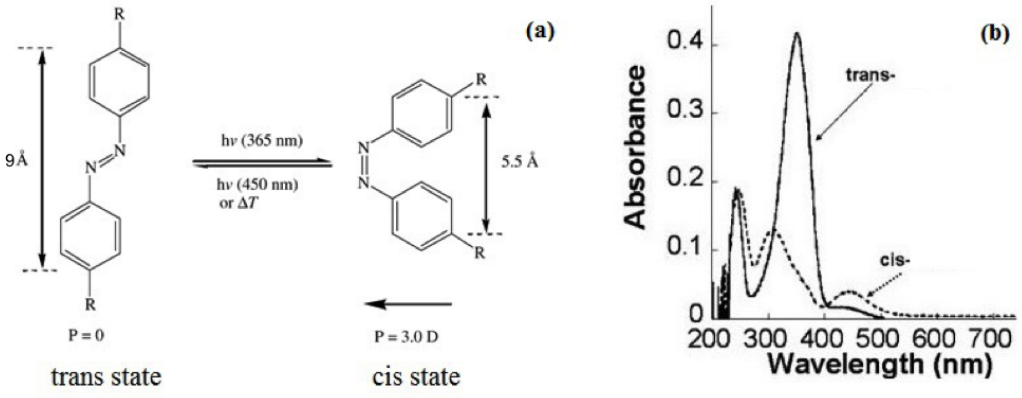

Figure 5.1: Schematic showing (a) the reversible photoisomerization between *trans* and *cis* form, and (b) the absorption spectra of *trans*-azobenzene (solid line) and *cis*-azobenzene (dashed line) in a suitable solvent. Images taken from [6].

The photo-induced *trans-cis* isomerization involves significant changes in the structure of the two forms. A decrease in the distance between the carbon atoms of the *para* substituted groups in azobenzene from about 9.0 Å in *trans* form to 5.5 Å in *cis* form can be seen. The *trans* azobenzene has no dipole moment, however under the transformation to *cis* form, the dipole moment changes to 3.0 Debye [7] (figure 5.1(a)).

The main feature of the absorption spectra of azo compounds is a low-intensity n-π^* absorption in the visible region for the *cis* form, and a higher intensity π-π^* absorption in the ultraviolet region for the *trans* form (figure 5.1(b)). Such a difference between the characteristic peaks occurs due to structural symmetry in the former, and non-planar distortions seen in the latter [8]. The wavelengths at which absorption occurs depend on the particular structure of the azo molecule. For unsubstituted azobenzenes, the spectra generally exhibit a high intensity absorption in the ultraviolet region close to 320 nm [9]. However, substitution by an electron donating group for example$-NH_2$, involves a general migration of electron density from the donor group towards the azo group thereby causing a shift in the intense *trans* peaks towards higher wavelengths. Such a shift depends upon the electron donating strength of the substituents [8].

These properties, if manifested in polymers, are of importance in the conformational changes of macromolecules and in designing polymers responsive to light. The challenge in polymer chemistry lies in applying these fundamental changes taking place at the molecular level in designing dually responsive polymers.

5.2.2 Azobenzene based responsive polymers

In general, it has been shown that the marked changes across the LCST of a polymer arise from the balance of hydrophobic/hydrophilic interactions of individual chains [10]. Depending on the desired property of the polymer, these interactions can be modified by varying the overall polymer composition and hence its LCST, as previously predicted [11]. The LCST is shifted to higher temperatures in the presence of hydrophilic co-monomer and decreases to lower temperatures in the presence of a hydrophobic co-monomer.

Based on the above principle, a variety of dually responsive polymers have been designed that exhibit tuneable thermo- and photo-responsive properties.

Poly(NIPAM-co-AZAAm)

In the pioneer work by Irie *et al.* [12], PNIPAM with azobenzene based N-phenylazophenyl acrylamide (AZAAm) groups was polymerized with the aim of inducing phase separation of polymer solution upon photo-irradiation [12]. The incorporation of the azobenzene moieties increased hydrophobicity in the parent PNIPAM system, thereby decreasing the overall LCST of the copolymer (figure 5.2(a)). The isomerization of non polar *trans* form to polar *cis* form under UV irradiation increased the solubility of the system, thereby increasing the phase separation temperature (figure 5.2(b)). A reversible effect was seen under Visible light irradiation, under which the LCST was seen to switch back to low temperature. An important observation to note is that the magnitude of the light-induced shift of the LCST was found to depend non-monotonously on the molar content of azobenzene, with a clear optimal content around 2.7% yielding a maximal shift (figure 5.2(a)), and that at optimal content the phase separation of the polymer solution could be switched isothermally under light irradiation.

These results showed an efficient way to tune the LCST of the copolymer. However,

in the perspective of biological applications, the LCST of such poly(NIPAM-co-AZAAm) is already too far below 37° to be suitable.

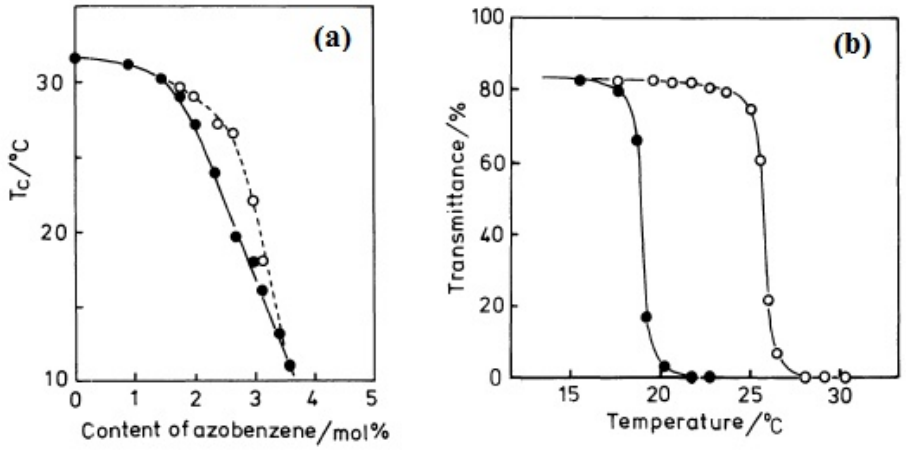

Figure 5.2: (a) Variation of the LCST with the Azo molar content in the copolymer. (○) UV-irradiated solutions, (●) dark-adapted or blue-irradiated solution. (b) Turbidity measurements (solution transmittance as a function of temperature) showing the difference in LCST before (●) and after (○) UV-irradiation. Images taken from [12].

Poly(DMA-co-AZAA)

Copolymers of N,N Dimethylacrylamide (DMA) and 4-phenyl-azophenyl acrylate (AZAA) were prepared by Kröger *et al* [13] in order to control the phase separation over a wide range of temperature. These authors have shown that while PDMA homopolymer is water soluble at any temperature, an LCST in a water was induced by copolymerization with the more hydrophobic AZAA species. They found that, similarly to the observations by Irie [12], the overall LCST decreased with increasing amount of the azobenzene-bearing monomer (figure 5.3(a)). Moreover, they observed that the reversible shift in LCST upon UV/Visible irradiation was very large (between 15 and 20°C towards hight temperatures under UV, see figure 5.3(b)) and did not significantly depend on the molar content of AZAA.

The light-induced shift in LCST was attributed to the isomerization and change in dipole moment of the azobenzene moieties upon irradiation. These DMA-based copolymers exhibited photo-tuneable properties, and AZAA incorporation at about 7 mol% appear to make them suitable for biology, since 37°C is between the LCSTs observed for *trans* and *cis* forms of AZAA.

However, a possible drawback of such copolymers is that the average value of the LCST cannot be tuned independently of the AZAA content. Furthermore, the observed effect of AZAA content on the magnitude of the LCST shift is in strong contrast with observations by Irie [12].

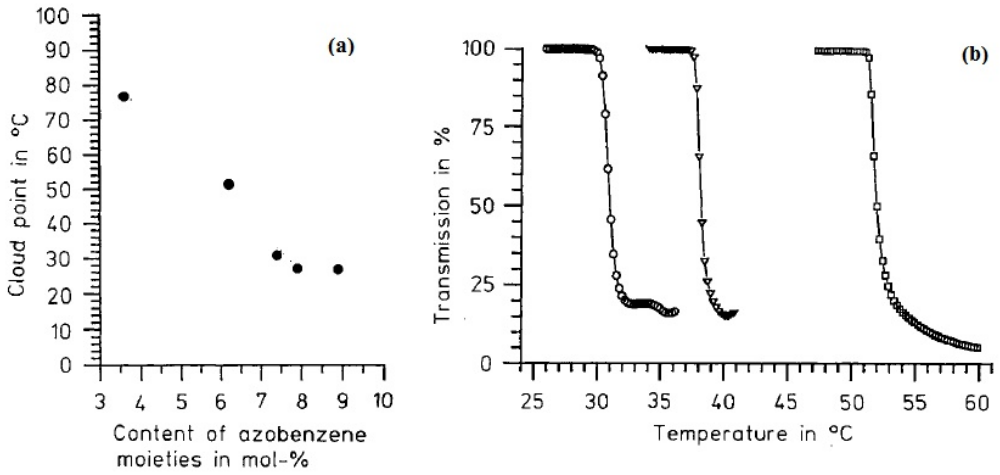

Figure 5.3: (a) LCST of p(DMA-co-AZAA) solutions as a function of azobenzene content in the polymer. (•) dark-adapted sample, (△) UV-irradiated, (□) blue-irradiated. (b) Variation of solution transmission as a function of temperature for dark-adapted (○), UV-irradiated (□), and blue-irradiated (▽) sample of copolymer with 7 mol% AZAA. Images taken from [13].

Poly(DMA-co-AZAA/AZAAm)

More recently, light responsive copolymers similar to those synthesized by Kröger *et al* were designed by Shimoboji *et al* in order to be conjugated to enzymes and reversibly regulated their activity upon light irradiation. Two different azobenzene based monomers, namely AZAA and its amide derivative (AZAAm) were copolymerized with DMA [14].

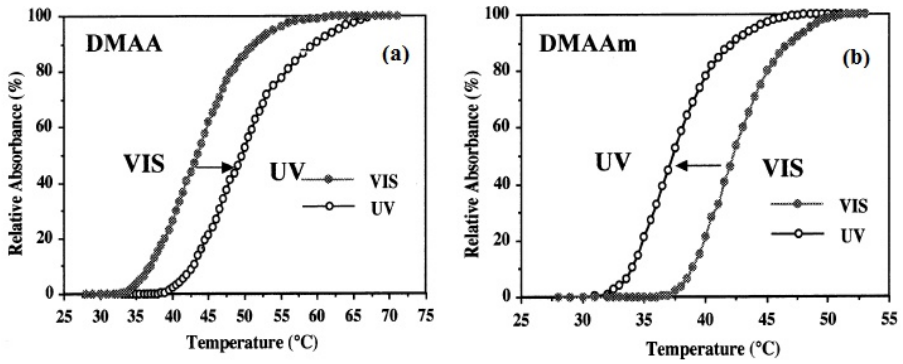

Figure 5.4: Effect of photo-irradiation on the LCST of (a) DMA-co-AZAA (5.9 mol%) and(b) DMA-co-AZAAm (9.6 mol%). Images taken from [14].

Surprisingly, the two copolymers were found to display opposite photo-induced effects: the LCST of the poly(DMA-co-AZAA) copolymer was shifted upward upon UV irradiation (figure 5.4(a)), in agreement with the above results [13], while the DMA-co-AZAAm copolymer solution showed a LCST that was lowered under UV (figure 5.4(b)).

5.2.3 Design strategy

From the three groups of results we have presented above, we see that copolymers based on NIPAM only, while they exhibit the wanted photo-induced effects and isothermal switching ability, can be used only at temperatures that are well below physiological conditions. On the other hand, copolymers based on DMA are more interesting candidates in the biological context. However, the discrepancies observed regarding the magnitude of the photo-induced shift in LCST, as well as the highly counter-intuitive effect reported by Hoffmann *et al* [14] with AZAAm (the more polar form of AZAAm yielding a lower LCST), raise questions regarding the robustness and reproducibility of these results.

In this context, we have chosen (i) to try to reproduce previous polymer synthesis [13, 14], with the scope of optimizing the copolymer composition to make it suitable for future biological applications, and (ii) to synthesize a new dually-responsive polymer.

Our polymers, synthesized from the monomers shown on figure 5.5, are:

- N,N Dimethylacrylamide (DMA) copolymerized with N-4-phenyl-azophenylacrylate (AZAA).
- N-isopropylacrylamide (NIPAM) copolymerized with DMA and N-phenyl-azophenylacrylamide(AZAAm).

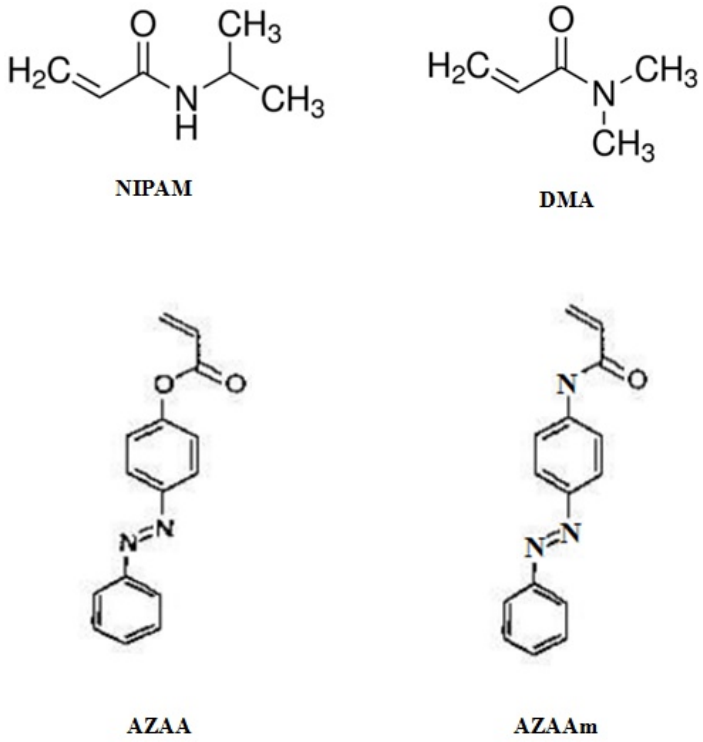

Figure 5.5: schematic showing the different monomers NIPAM, DMA along with the chromophores AZAA and AZAAm used to design dually responsive copolymers.

Figure 5.6 summarizes the goal we wish to achieve in our present study. We aim at designing a polymer such that it exhibits a transition at temperature T_a very close below 37°C. When the azobenzene chromophore is isomerized, it transforms from the non polar *trans* to polar *cis* form, thereby inducing a shift of LCST to a higher temperature T_b. At

any T lying between T_a and T_b, the polymer conformation is thus expected to be changed reversibly and isothermally under light irradiation.

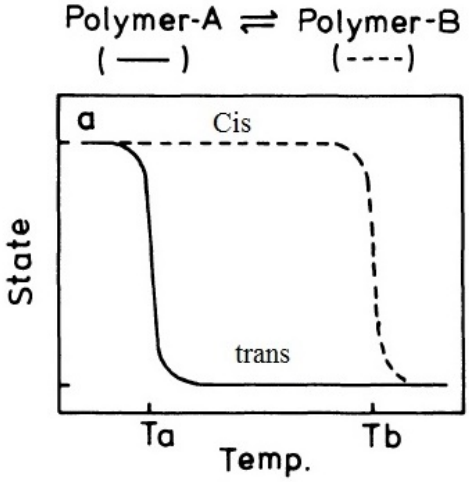

Figure 5.6: At any temperatures between T_a and T_b, the polymer of interest should be switched between state a (water soluble) and state b (water insoluble) via photo-isomerization.

5.3 Materials and Methods

Materials

N-isopropylacrylamide (NIPAM, 99%), triethylamine (TEA, 99.7%), copper (I) chloride (CuCl, 99% extra pure), copper (II) bromide ($CuBr_2$, 99% extra pure), 1,1,7,7-pentamethyl-diethylenetriamine (PMDETA, 99%), and anisole were purchased from Acros Organics. Ascorbic acid (AA, 99%), ethyl isobutyrate (EiB), and tin 2-ethylhexanoate were obtained from Sigma Aldrich. Tris[2-(dimethylamino)ethylamine] (Me_6TREN, 99% pure) was obtained from Alfa Alesar. Methyl 2-chloropropionate (MCP, 95% pure), 4-hydroxyazobenzene (99% pure), 4-amino-azobenzene (99% pure) and N,N-dimethyl-acrylamide (99% pure) were purchased from Tokyo Chemical Industries (TCI). 2,2'-azobis-butyronitrile (AIBN) was provided by Dr. Laurent Heux from the CERMAV Laboratory, Grenoble. Methanol, 1,4-dioxane and diethyl ether were obtained from VWR chemicals. Tetrahydrofuran (THF), sodium acetate, n-hexane, absolute ethanol and chloroform were obtained from Fischer chemicals (Laboratory Grade). Dimethylsulphoxide (DMSO) was obtained from Prolabo Merck Eurolabs.

All reagents were used as received except for (i) DMA, from which trace amounts of polymerization inhibitor were removed by passing over an "inhibitor remover" pre-packed column obtained from Sigma Aldrich, and (ii) NIPAM, which was recrystallized twice in n-Hexane at 60°C and then dried for at least one day before use.

5.3.1 Synthesis of photoresponsive monomers

Two azobenzene containing monomers, namely N-4-phenyl-azophenyl acrylate (AZAA) and N-4 phenyl-azophenyl acrylamide(AZAAm), were synthesised.

Synthesis of 4-phenyl-azophenyl acrylate (AZAA) monomer The synthesis of the acrylate monomer was performed following a condensation reaction as described previously in the works of Menzel *et al* [13]. In a round bottom flask, 4-hydroxyazobenzene (0.02 mol, 3.96 grams) and triethylamine (TEA, 0.022 mol, 3.06 mL, acting as a promoter) were dissolved in 20 mL of diethyl ether (figure 5.7). The flask was tightly sealed using a rubber septum, cooled to 0°C in an ice bath and stirred continuously under argon supply for about 30 minutes. A solution of acryloyl chloride (0.02 mol, 1.62mL) in 10 mL of diethyl ether was then added dropwise using a glass syringe. The reaction solution was constantly stirred, and the formation of triethylammonium salt in the form of a precipitate was observed immediately upon the acryloyl chloride addition. After addition of the acryloyl chloride, the reaction mixture was washed thrice using an aqueous solution of sodium hydrogencarbonate (6 weight %,). This was done to ensure complete removal of unreacted polar compounds. The organic solution was then dried via solvent evaporation technique. The dry crude product obtained was recrystallized from a mixture of ethanol and water (1:1). The final product was characterized using UV/Visible spectroscopy and ^1H NMR spectroscopy. The yield was around 50 %.

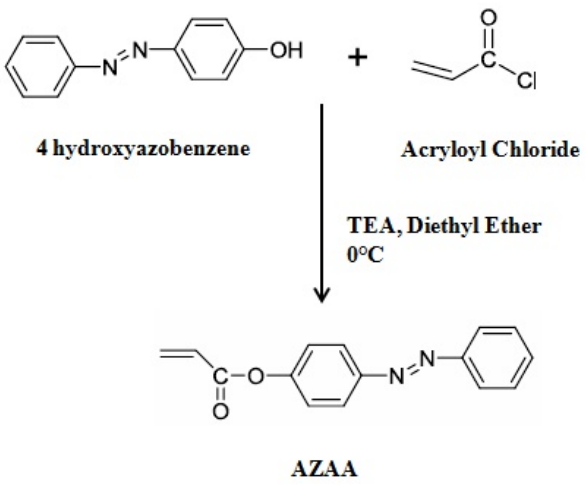

Figure 5.7: schematic showing the synthesis of 4-phenyl-azophenyl acrylate (AZAA) monomer

Synthesis of 4-phenyl-azophenyl acrylamide (AZAAm) monomer AZAAm was prepared by the condensation of 4-amino-azobenzene and acryloyl chloride, using a protocol adapted from [15] (figure 5.8).

In a triple-neck round bottom flask, 4-amino-azobenzene (0.02 mol, 3.49 grams) was dissolved in 30 mL of THF solvent, to which TEA (0.03 mol, 4.18mL) was added. A volumetric glass pipette, equipped with a stopcock was fixed to one of the necks of the

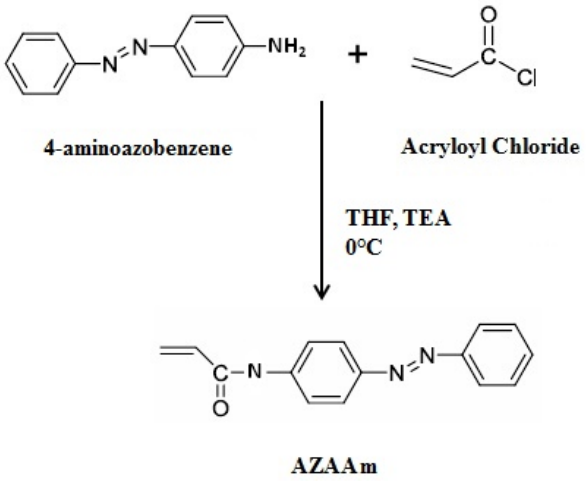

Figure 5.8: schematic showing the synthesis of 4-phenyl-azophenyl acrylamide (AZAAm) monomer

flask. The flask was tightly sealed, purged with argon and stirred at 0°C in an ice bath for about 30 minutes. Acryloyl chloride (0.02 mol, 1.62mL), dissolved in 8mL of THF was added dropwise via the glass pipette. The resulting solution was maintained at 0°C and constantly stirred. The salt formation took place immediately upon the acryloyl chloride addition. After completion, the reaction mixture was stirred for about 48 hours at room temperature. The precipitate was removed by filtration, and the organic solution was washed three times with an aqueous sodium hydrogencarbonate solution to remove the polar compounds. The organic layer was then dried and the crude product was purified over a silica column using a 1:1 n-hexane:sodium acetate solution as the eluent. Prior to this step, the proper choice of eluent was made by carrying out Thin Layer Chromatography. The final solution was dried and collected. The yield was around 65%.

5.3.2 Synthesis of Stimuli responsive polymers

Copolymerization of DMA with AZAA monomer

The copolymer poly(DMA-co-AZAA) was synthesized by free radical polymerization, as described previously [13]. DMA (0.05 mol) was dissolved with varying feed ratios of AZAA in 20 mL of 1,4-dioxane solvent. AIBN (0.5 mmol) was used as the polymerization initiator (figure 5.9). The solution was degassed under argon for 15 minutes and heated to 60°C for varying amounts of time depending upon the monomer compositions of AZAA added. The polymerization was stopped by cooling the solution in an ice bath, and the polymer was precipitated into diethyl ether solvent. The resulting polymer was collected and characterized using turbidity measurements and UV/visible spectroscopy.

Copolymerization of NIPAM with DMA and AZAAm

Terpolymer poly(DMA-NIPAM-AZAAm) were synthesized using the ARGET-ATRP protocol (figure 5.10). DMA and NIPAM in varying molar ratios were dissolved in 1.5mL

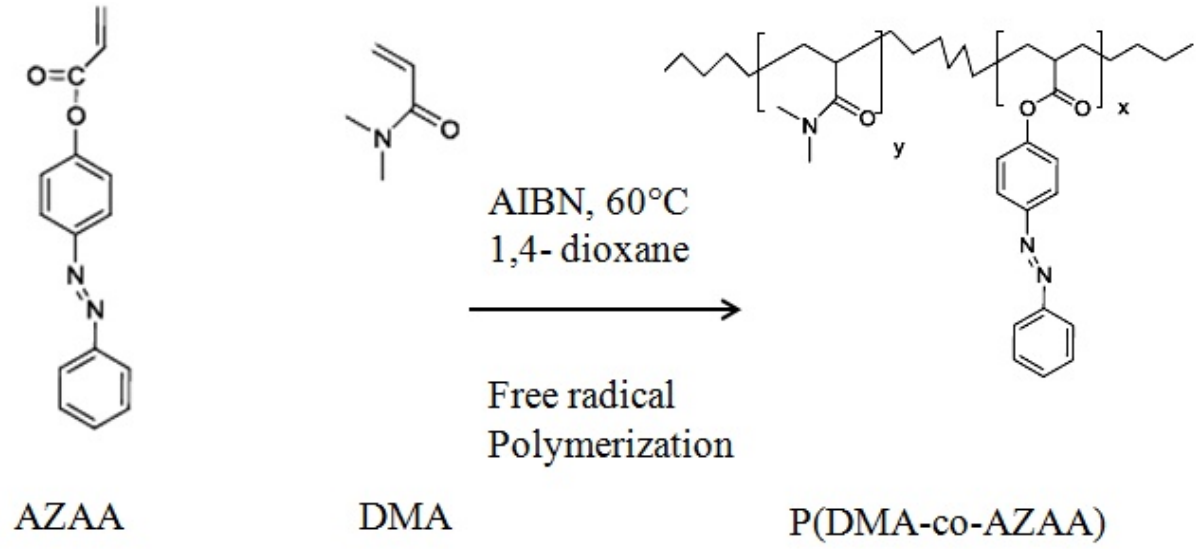

Figure 5.9: schematic showing the structure of AZAA monomer, DMA, and Copolymer(DMA-co-AZAA)

methanol as the solvent under a closed sealed flask with constant stirring.

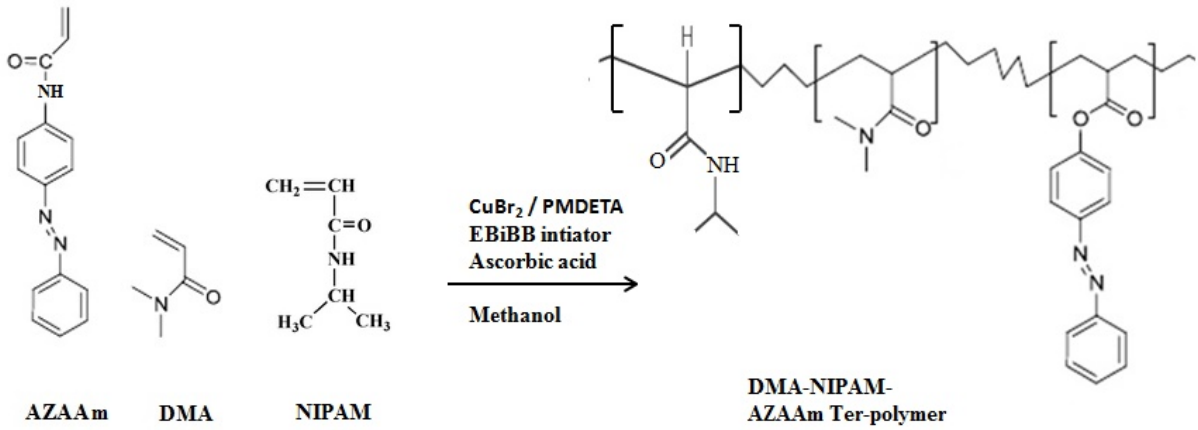

Figure 5.10: schematic showing the ARGET-ATRP protocol to generate the ter-polymer DMA-NIPAM-AZAAm

Following this, 1.5mg $CuBr_2$ and 40μL PMDETA were sequentially added in the mixture solution. Ascorbic acid (30 mg) was then added to the mixture. AZAAm in varying amounts was finally added along with 15μL EiB initiator while constantly stirring the solution. Polymerization lasted until a viscous solution was formed. Chain growth in the solution was monitored from time to time by precipitating a fixed aliquot of the polymer solution in diethyl ether solvent kept in an ice bath.

An alternative strategy was used to design poly(DMA-NIPAM-AZAAm) terpolymers. A catalyst solution having CuCl (10 mg), Me_6TREN (100μL) and $Sn(EH)_2$ (100 μL) in 1 mL DMSO was prepared and purged under argon supply. A monomer solution containing NIPAM (1g, 8.88 mmol), DMA (0.54 mL, 5.25 mmol), AZAAm (43mg, 0.17 mmol) along with 3μL MCP initiator in 1ml DMSO was separately prepared and purged

under argon supply. The degassed catalyst solution was then injected into the monomer solution with constant stirring and the final mixture was left to polymerize for prescribed time periods. The reaction was started by the initial addition of 200 μL of the catalyst solution, after which a rate of fresh catalyst injection of 100 μL/hour was maintained using a syringe pump. Fixed amounts of polymer aliquots were precipitated at regular intervals in cold diethyl ether.

5.3.3 Characterization of polymers

Turbidity measurements

Turbidity measurements allows us to optically probe the solubility changes of a polymer in solution. This is done by monitoring the changes in solution transmission as a function of temperature. As the solvent temperature increases, an initially transparent polymer solution starts to phase separate by turning "cloudy". At this point, the transmission values begin to decrease. From such cloud point measurements, we define the LCST as the particular temperature $T_{50\%}$ at which the transmission drops to half of the initial value.

Turbidity measurements were performed using a home built set-up comprising of a collimated laser diode (1mW), a thermostated sample holder equipped with Peltier elements, and a photodetector. The changes in transmittance were recorded at λ= 632nm, well above the absorption bands of azobenzene.

An empty quartz cuvette was first placed in the sample holder and light from the laser diode was allowed to pass through it. Transmitted light was collected at the photodetector and converted to a readout voltage via a built-in amplifier. Following this, a polymer solution, kept at 4°C for about 2 hours prior to the experiments, was placed into the cuvette. The readout voltage recorded for the clear and cold polymer solution was equal to that of the empty cuvette, and was taken as 100% transmission. The sample was then subjected to alternate heating and cooling cycles between 25 and 70°C. The Peltier elements allowed control of the heating and cooling within fraction of degrees, with a variation rate fixed at 0.01°C/second. The transmission and temperature values were recorded as a function of time with an Agilent Datalogger (34970A) interfaced with Labview.

Turbidity measurements allowed:

- Estimating the LCST of the polymer solution
- Studying the effect of light irradiation on the LCST shift
- Assessing the ability of the polymers to undergo isothermal photoswitching

UV Visible Spectroscopy

UV/visible spectra were recorded on a JASCO-V650 instrument and methanol was used as the solvent. The spectra were recorded over a range of 200-650 nm using in a double-beam configuration. The incoming light was split into two beams before it reached the

sample. One beam was used as the reference passing through pure solvent, and the other beam passed through the sample. The reference beam intensity was taken as 100% transmission (or 0 absorbance), and the resultant spectrum displayed the ratio of the two beam intensities, thus showing the net absorbance only for the molecule of interest. The intensity of light passing through a sample (I) was compared to the intensity of light passed through the reference (I_0), giving rise to a resultant transmittance T given by the relation $T = (\frac{I}{I_0})$. The absorbance ($Abs.$) was then computed as:

$$Abs. = -log(T) \tag{5.1}$$

UV-Visible spectroscopic analysis were done in the present study in order to

- characterize the absorption peaks of the synthesized chromophores
- Investigate their reversible photo-isomerization, and
- Quantify the monomer content of chromophores in the resulting polymers.

In both turbidimetry and UV/Vis spectroscopy experiments, photo-isomerization was achieved using:

- A high-power UV source (CS2010 from Thorlabs, 27W/cm^2 at 365 nm).
- A fibred blue laser diode equipped with a collimated lens (LEDMOD 470 from Omicron-Laserage, 300 mW at 465 nm).

Nuclear Magnetic Resonance (NMR) spectroscopy

NMR spectroscopy allows confirming the identity of the photochromic monomers synthesized. Depending on the strength of the external magnetic field, the magnetic nuclei (^{1}H) gets aligned to the direction of the the applied field and oscillates with a resonance frequency. All protons present in the sample give different resonance signals due to the differing electronic environments surrounding the nuclei. Upon application of an external magnetic field, the electrons generate a local magnetic field that "shields" the proton from the applied magnetic field, which must therefore be increased in order to achieve resonance. Such increments are very small, and usually exist in parts per million (ppm). This operation therefore gives the chemical shift that provides information about the structure of the molecule.

^{1}H NMR spectra were recorded on a Bruker 400 MHz spectrometer. Chemical shifts for ^{1}H NMR spectra were referenced relative to residual protium in deuterated methanol (CD_3OD, δ = 3.31 ppm). ^{1}H NMR spectra were performed at the ICMG Chemistry Nanobio Platform, Grenoble, under the supervision of Dr. Jerome Fortage.

In the following section, I present the results obtained during my studies on responsive polymers in terms of the structural characterization of the photochromic species and the solution properties of the designed polymers.

5.4 Results

5.4.1 Characterization of the synthesized monomers

At first, we have probed the reversible cis-trans isomerization of the synthesized chromophores AZAA and AZAAm via UV/Visible absorption spectroscopy.

The electronic absorption spectra for a dilute solution of AZAA in methanol shows an intense *trans* absorption peak (π-π^* transition) around 322 nm in the UV region and a low intensity *cis* absorption peak (n-π^* transition) around 440 nm in the visible region (figure 5.11 black and red peaks respectively). The λ_{max} values for the two absorption peaks of AZAA in methanol were consistent with values obtained previously [13].

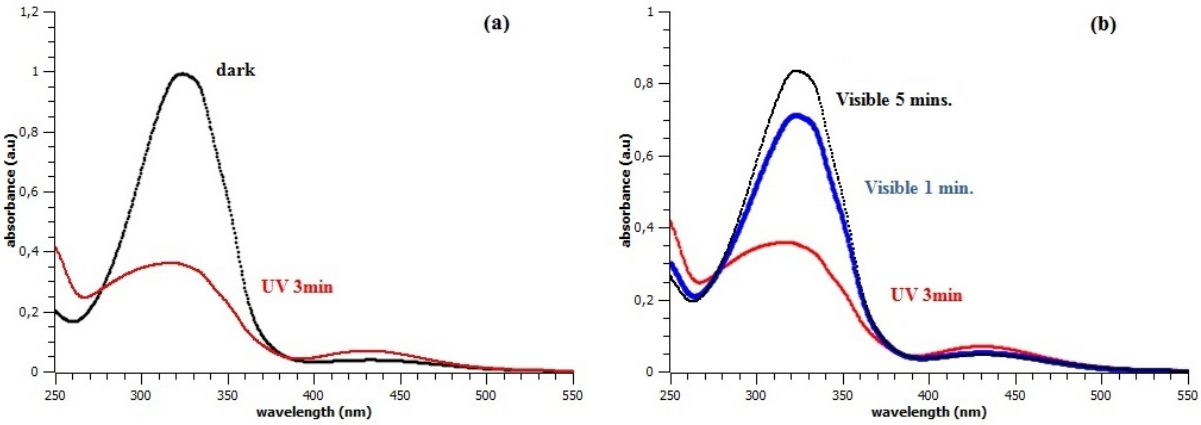

Figure 5.11: Absorption spectra of a dilute AZAA solution in presence of (a) UV irradiation showing the decrease in the *trans* band (black curve) and increase in the *cis* band (red curve)(b) Blue irradiation for 1 and 5 minutes showing the increase in the *trans* absorption band (black curve) and a corresponding decrease in *cis* band.

Under UV irradiation, we observe a strong decrease in the intensity of *trans* absorption band accompanied by an increase in the *cis* absorption band (figure 5.11(a)). This effect lasts until the photo-stationary state is reached, where the absorption peaks are seen to remain unchanged in response to UV irradiation. The UV isomerization effect was seen to last up to 3 minutes. Following this, a reversible $cis - trans$ transformation can be induced by shining blue light, which is marked by a gradual increase in the intensity of the *trans* absorption band and a subsequent decrease in the intensity of *cis* band. The blue-irradiation effect was seen to be prolonged up to 5 minutes.

The characteristic spectra for a dilute solution of AZAAm in methanol shows a high intensity *trans* absorption peaks around 354 nm and a *cis* absorption peak around 440 nm (figure 5.12(a)). Both the UV induced enhancement in *cis* peaks and the blue irradiation-induced increase in the *trans* peaks correspond to the reversible isomerization in AZAAm.

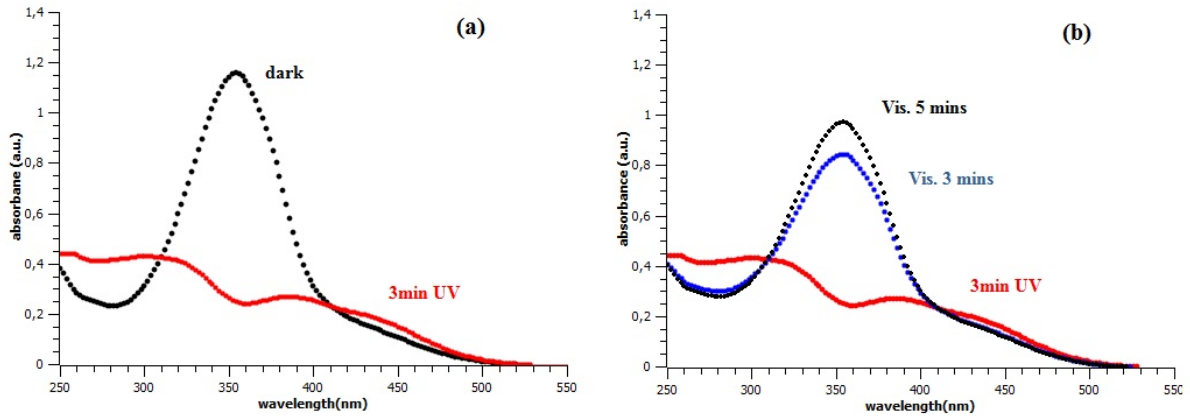

Figure 5.12: Absorption spectra of a dilute AZAAm solution showing reversible changes in *trans* (black curves) and *cis* peaks (red curves)in presence of UV and Visible light irradiation.

NMR spectra for the Chromophores

The 400MHz ^{1}H NMR spectra were used to confirm the structures of AZAA and AZAAm species. The AZAA species has different set of protons that are magnetically and chemically non equivalent.

The spectrum associated with AZAA is shown in figure 5.13. It shows three single peaks corresponding to the three protons of the acryloyl group having chemical shifts δ in the range 6-6.8 ppm. The two protons ortho to the azo bond (-N=N-) are shielded strongly by the nitrogen atom and display two doublets having δ= 7.8-8.2 ppm. A proton at a free para position gives a triplet peak. The proton next to the oxygen leads to a doublet at δ values around 7.4 ppm. The characteristic chemical shifts for the various protons are well correlated with those obtained from literature [13] in methanol. The spectrum therefore indicates a successful AZAA synthesis having properly assigned peaks.

The spectrum for AZAAm is shown in figure 5.14. The characteristic peaks for the azobenzene and acryloyl protons are depicted as δ= 5.8-6.6 (3H) for the acryloyl protons, δ= 7.4-7.6 (3H) and 7.8-8.0 (6H) for the azobenzene species. The characteristic peaks for the different protons in methanol have not been previously reported. As a comparison, the spectra recorded in DMSO [14] show marginal variations with respect to our data. This suggests a successful AZAAm synthesis with no unwanted peaks due to any impurities.

The absorption studies, along with NMR structural characterization, indicate a successful synthesis of the photochromic monomers. We have exploited their features for the design of dually responsive polymers, as described now.

5.4.2 DMA-co-AZAA copolymer: synthesis and characterization

We have prepared a set of DMA-co-AZAA copolymers by free radical polymerization. The overall polymer composition was varied by changing the molar contents of AZAA (from 3.5 to 12 mol% in the feed) in order to place the LCST at about 37°C. The characteristics

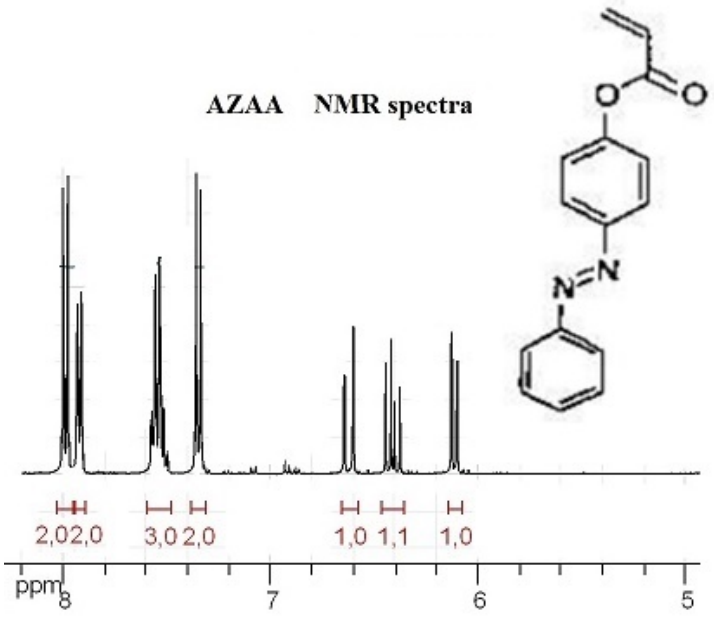

Figure 5.13: The NMR spectra for AZAA showing the characteristic peaks corresponding to the various protons.

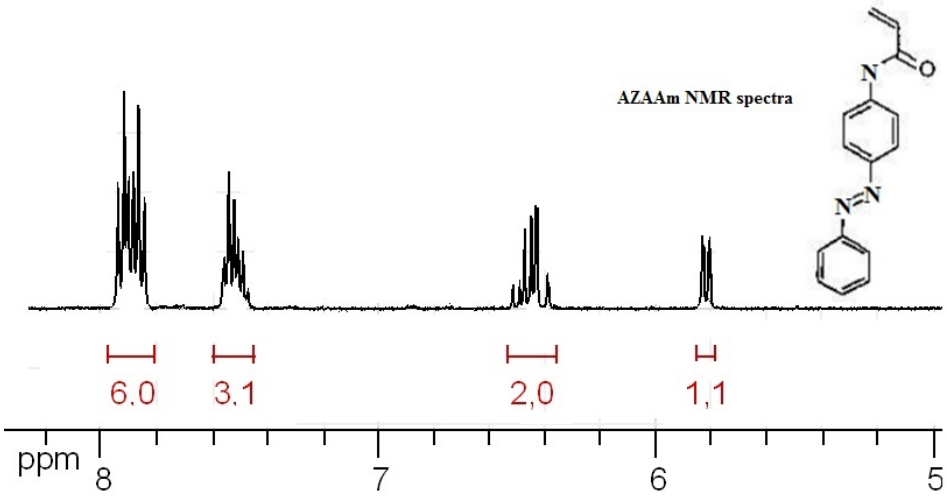

Figure 5.14: The NMR spectra for AZAAm showing the characteristic peaks corresponding to the various protons.

of the various co-polymers are summarized in Table 5.1.

We have investigated the light induced-isomerization of the azobenene group of the photosensitive copolymers. The electronic spectra for a copolymer solution (Cp5 , as shown in the Table 5.1) are shown on figure 5.15. It shows that the absorption peaks are located at wavelengths that closely match those obtained for the AZAA monomer (referring to figure 5.11). UV irradiation decreases the intense *trans* band (black curves) and leads to the appearance of a *cis* peak (red curves) post the isomerization. During the relaxation of the excited azobenzene back to its initial state via blue irradiation, the

Co-polymer	feed DMA/AZAA molar ratio	actual AZAA content (mol%)	LCST-(dark)/°C	LCST-(UV)/°C	LCST-(Vis)/°C	ΔT_{UV}/ °C
Cp1	100:3.5	4.0	100	-	-	
Cp2	100:8	9.1	72	74	73	2
Cp3	100:9	11.6	45	-	-	-
Cp4	100:9.5	11.2	42	-	-	-
Cp5	100:10	11.2	34	38	34.5	4
Cp6	100:12	30	40	-	-	-

Table 5.1: List of the various DMA copolymers, with their solution properties.

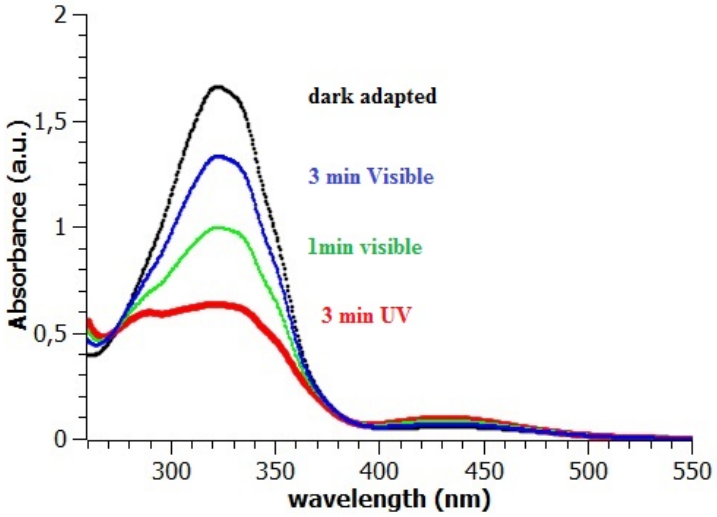

Figure 5.15: The absorption spectra for DMA-co-AZAA(10) showing the reversible $cis-trans$ isomerization

trans peak re-emerges at its initial position (green and blue curves). Such an effect is seen for all the synthesized copolymers. These spectra show a successful incorporation of the AZAA into the copolymer.

Following this, we have quantified the actual AZAA content in the copolymers using the UV/Vis spectroscopic data.

Estimation of the molar content in the copolymer

The molar contents of AZAA have been estimated from the absorption peaks in the spectra as follows.

First, a reference absorption spectrum of the photoresponsive monomer is measured with a dilute AZAA solution of known molar concentration C_{mono}^{AZAA}. Then, a dilute solution of the copolymer of interest is prepared at a known mass concentration of polymer, and an absorption spectrum is subsequently measured.

The monomer and polymer solution concentrations are chosen so that they both follow the Beer-Lambert law, for which the respective absorption can be written as:

$$Abs_{mono} = C_{mono}^{AZAA} \times L \times \epsilon \tag{5.2}$$

and

$$Abs_{poly} = C_{poly}^{AZAA} \times L \times \epsilon \tag{5.3}$$

where L is the length of the quartz cuvette, ϵ is the molar absorption coefficient of the chromophore, and C_{poly}^{AZAA} is the molar concentration of AZAA in the polymer solution. Assuming that the molar absorption coefficient of AZAA is the same in its monomer and polymerized form, C_{poly}^{AZAA} can be expressed as:

$$C_{poly}^{AZAA} = C_{mono}^{AZAA} \frac{Abs_{poly}}{Abs_{mono}} \tag{5.4}$$

From this relationship, we can express the number of moles of AZAA present in the polymer solution of known volume V as:

$$n_{poly}^{AZAA} = C_{mono}^{AZAA} \frac{Abs_{poly}}{Abs_{mono}} V \tag{5.5}$$

By measuring the absorbance *Abs* at the *cis* or *trans* peaks for the monomer and polymer solutions, and knowing V and the reference concentration C_{mono}^{AZAA}, we can therefore compute n_{poly}^{AZAA}.

Besides, the mass of polymer in the solution, m_{poly}, is related to the monomer content as:

$$m_{poly} = n^{DMA} M^{DMA} + n_{poly}^{AZAA} M^{AZAA} \tag{5.6}$$

with n and M the number of moles and molecular weight of the two monomers. From eq. 5.6, with $M^{DMA} = 99.1$ g/mol, $M^{AZAA} = 252.3$ g/mol, and the known polymer mass in the solution, we can compute the amount of DMA in the solution:

$$n^{DMA} = \frac{m_{poly} - n_{poly}^{AZAA} M^{AZAA}}{M^{DMA}} \tag{5.7}$$

From eqs. 5.5 and 5.7, we can finally compute the actual molar content of AZAA in the copolymer, x_{AZAA}, as

$$x_{AZAA} = \frac{n_{poly}^{AZAA}}{n^{DMA} + n_{poly}^{AZAA}} \tag{5.8}$$

The estimated molar contents of the azobenzene moieties in the copolymer are presented in Table 5.1.

The estimated values show little deviation at low feed ratios, but are seen to be largely inconsistent above 10% feed content. The observed discrepancy in chromophore contents suggests a poorly controlled incorporation of AZAA into the polymer at large molar contents using conventional radical polymerization.

Thermoresponsive properties

In order to understand the variation of LCST with respect to the added photochromic monomer, we have studied the solution properties for the set of synthesized copolymers using turbidity measurements.

We observed that at least 3.5 mol% azobenzene moieties needed to be incorporated into the polymer to induce a phase separation upon heating. This is consistent with previous attempts towards synthesizing azobenzene based DMA copolymers [13]. Figure 5.16 shows that the LCST of the dark-adapted solutions (stable *trans* form of AZAA) progressively decreases as the AZAA feed ratio is increased from 3.5 to 10%, and increases beyond 10%.

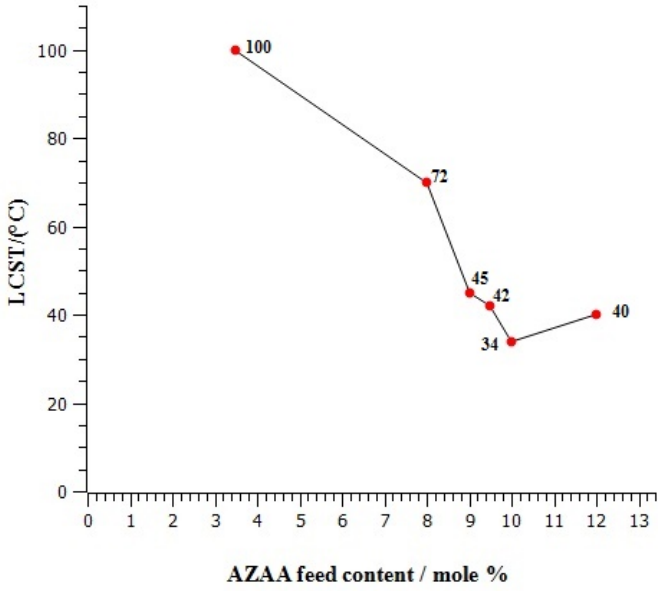

Figure 5.16: Variation of LCST as a function of added azobenzene chromophore.

The introduction of hydrophobic azobenzene groups should make the resulting polymer less soluble, thereby decreasing the LCST. This is consistent with the behaviour observed at AZAA molar content lower than 10%.

However, the increase in LCST for higher feed contents of 12 mol % is counter-intuitive. Reports of such a non monotonic LCST variation are rare but have been observed previously by Liu *et al* for PNIPAM based terpolymers having variable compositions of hydrophilic oligo(ethylene oxide) side groups and azobenzene moieties [16]. These authors attributed the surprising increase in LCST at high chromophore content to a phenomenon of clustering of the hydrophobic azo groups, inducing the formation of small ($\sim$ 100 nm) micelle-like chain aggregates that were stable and more water-soluble at high temperatures than individual chains, thus shifting to larger temperature the formation of the large (micron-size) aggregates typically detected in turbidity measurements.

Photo-responsive properties

We have probed the photo-response of the designed copolymers by studying the dependence of their LCST in response to UV/Visible light irradiations. Figure 5.17 shows the transmittance changes of an aqueous solution of the Cp5 copolymer (see Table 5.1) under different light exposures.

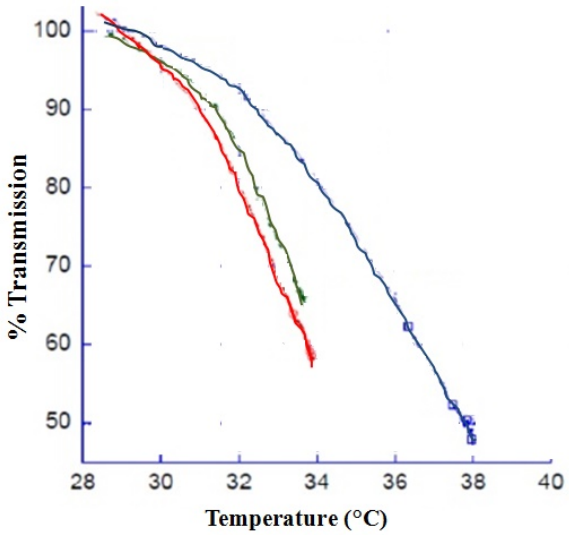

Figure 5.17: Transmission changes of an aqueous solution of Cp5 (10 mol % AZAA) when heated in dark (red curves), in presence of UV irradiation (blue curves), and in presence of visible irradiation (green curves).

Upon heating the dark-adapted copolymer solution (red curve), it starts to phase-separate and becomes turbid around 32°C, and its LCST, defined as T at which $T\% = 50\%$, is found to be around 34°C. On cooling the system, the turbid solution again becomes transparent (cooling curves not shown here).

The UV irradiated Cp5 solution displays a LCST around 38°C, consistent with the isomerization of *trans* azobenzene into the more polar *cis* form that increases the solubility of polymer in solution. Under the visible light exposure ($\lambda \sim 465$ nm), the polar *cis* form are re-isomerized to the less polar *trans* species, which leads to a LCST back around 34°C (green curve). The LCSTs differ by a value of 4°C between UV and visible irradiation. These results show that the Cp5 copolymer solution undergoes phase separation at temperatures that can be reversible tuned under alternate exposure of UV and Visible lights. These findings are consistent with previous results showing a light induced reversible shift in LCST in DMA-co-AZAA and DMA-co-AZAAm copolymers by about 5°C [14].

In an attempt to demonstrate a photo-induced isothermal phase transition, we have investigated the effect of UV/Visible photocycling on the solubility changes of an aqueous Cp2 copolymer solution. As seen in figure 5.18, at temperatures close to the LCST, where the solution appears cloudy, irradiation with UV light leads to a spontaneous increase in transmittance value. Conversely, irradiating the solution with visible light leads to reap-

pearance of cloudiness in the solution, that is characterized as a decrease in transmission. This provides our first proof-of-principle for the possibility of isothermal photo-switching of the DMA-AZAA copolymer solubility.

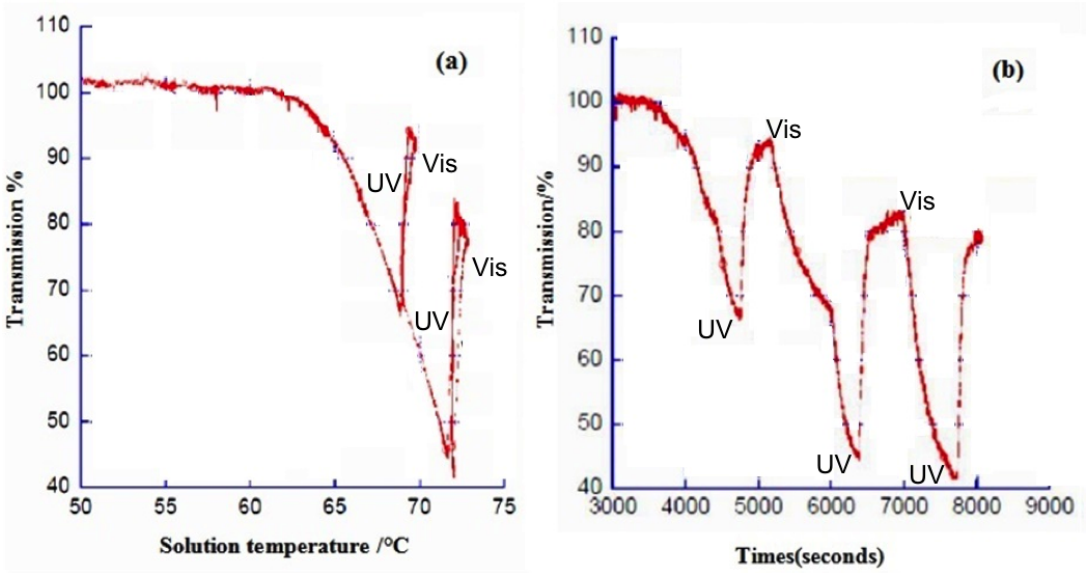

Figure 5.18: (a) Transmission of a water solution of Cp2 as a function of temperature: at two different temperatures in the transition region, shining UV light is seen to increase the transmission, while shining blue light brings the transmission back to its initial level. (b) same data plotted as a function of time.

It is however important to note at that stage that, although the expected photo-induced effects were seen with Cp2 and Cp5 aqueous solutions, their response in temperature calls for comments. Indeed, it is seen on figure 5.17 and 5.18 that the decrease in solution transmission, signing the good to poor solvent transition, occurs over a rather broad range of temperature (typically 10°C), such that our definition of a single LCST as $T_{50\%}$ might be questionable. Such a spread transition is reminiscent of the observations of Hoffmann *et al* [14] (see figure 5.4), from which we have directly adapted the free radical polymerization scheme to produce similar DMA-AZAA copolymers here. On the one hand, conventional free radical polymerization is known to yield polymers with a fairly broad mass distribution (high polydispersity). On the other hand, it is documented for other thermoresponsive polymers that chains of different length exhibit different LCST [17]. Overall, we are thus tempted to attribute the observed broad thermal transition as resulting from high polydispersity of the synthesized polymers.

In addition, the expected photo-induced control of polymer solubility were observed only with Cp2 and Cp5 copolymers, while, as seen in Table 5.1, the 4 other copolymers, some having compositions very close to Cp5, did not show any shift of the LCST under light irradiation. This, added to the fact that the actual molar content of AZAA appeared difficult to control accurately, encouraged us to explore a different design strategy to obtained the desired polymeric systems.

5.4.3 DMA-NIPAM-AZAAm terpolymer: synthesis and characterization

We have synthesized a novel acrylamide based terpolymer following the ARGET-ATRP protocol. This method is chosen for it allows a proper control of polymerization growth, as shown in the previous chapters, in contrast to free radical polymerization. The polymeric system comprises of predominant fractions of NIPAM along with varying amounts of DMA and N-phenyl-azophenyl-acrylamide (AZAAm) as the photoresponsive monomer. Herein, we use only acrylamide based monomers in order to avoid species having different rates of polymerization reactions. The feed ratios of the chromophores are kept low in order to avoid any possible aggregation in polymeric chains, as discussed above [16].

As performed previously, the characteristic photochemistry of the terpolymers is first verified by recording their absorption spectra. As shown in figure 5.19, the location of the absorption bands show marginal variations from that of the individual AZAAm chromophores along with a photo-induced disappearance/re-appearance of the absorption bands. These results indicate a successful addition of azobenzene monomer in the polymer system.

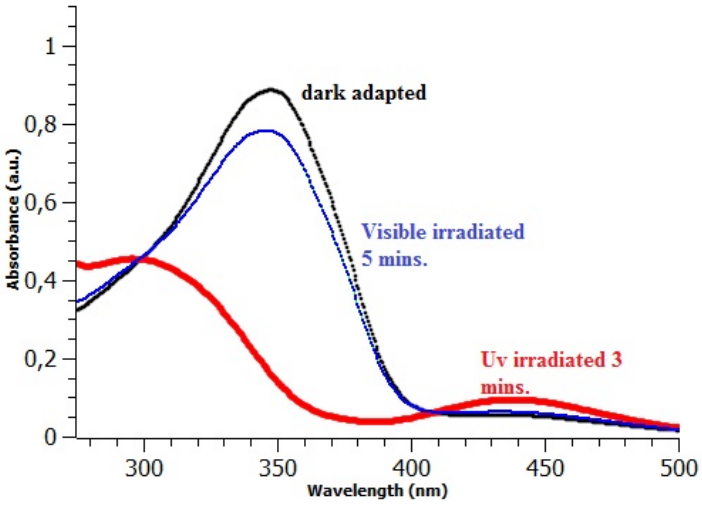

Figure 5.19: Absorption spectra showing reversible *trans cis* isomerization in P(DMA-NIPAM-AZAAm) in a dilute solution of Terp1. (see table 5.2)

Estimation of molar content

For the estimation of the molar content of the azobenzene chromophore in the terpolymer DMA-NIPAM-AZAAm, we have used UV/Vis spectroscopy, as for DMA-AZAA copolymers, by simply adapting equations 5.6 and 5.8 to a three-component situation. The characteristic features of the prepared terpolymers are shown in Table 4.2.

We observe that the feed and determined chromophore contents are closely related over the whole range of incorporated feed percentages. This suggests that ARGET-ATRP allows a better growth control of polymeric chains. These fundamental studies encouraged us to investigate the solution properties of the terpolymer systems.

Ter-polymer	fed molar ratio (DMA-NIPAM-AZAAm)	AZAAm actual content	LCST-(dark)	LCST-(UV)	LCST-(Vis)	ΔT_{UV}
Terp1	50:50:2.5	2.25	34.2	36.4	34.4	2.2
Terp2	50:50:2	2.01	38.0	39.4	38.6	1.4
Terp3	50:50:1	0.53	47.7	52	46.9	4.3
Terp4	40:60:1	0.68	42	44.7	43	2.7
Terp5	30:70:1	0.58	32.7	34.8	33	2.1
Terp6	40:60:1.2	0.75	39.1	43.5	40.5	3.8
Terp7	40:60:1.5	0.98	38.2	40.4	38.9	2.2
Terp8	37:63:1.2	0.80	36.9	39.4	37.2	2.5

Table 5.2: Summary of the characteristic features of the terpolymers synthesized via ARGET-ATRP protocol.

Solution Properties

All the different terpolymers synthesized following the ARGET-ATRP protocol display a LCST in water and exhibit light-induced LCST variations, in contrast to DMA-co-AZAA. In order to obtain phase separation around the desired temperatures, we have tried to optimize our terpolymer system by varying the polymeric compositions in the following way:

- Varying the net hydrophobicity of the system by changing the incorported amounts of the azo chomophore
- Changing the relative comonomer DMA:NIPAM ratios with fixed azo contents
- Minutely adjusting the relative comonomer ratios and the azo content in the terpolymer simultaneously.

Effect of varying the NIPAM:DMA molar content on LCST

With an aim to tune the LCST at 37°C, we first investigated the effect of varying the comonomer composition in the reaction feed. This involved decreasing the relative molar ratios of DMA with respect to NIPAM, keeping a fixed azo molar content in the terpolymer. We observe that with progressive decrease in DMA molar contents and the corresponding increase in NIPAM molar contents, the LCST values for Terp3 (black curves), terp4 (blue curves) and terp5 (red curves) can be varied over a large range of temperature (figure 5.20).

The incorporation of DMA, a hydrophilic monomer, accounts for an increase in the overall solubility of the system. Thus, a progressive decrease in the relative amounts of DMA leads to a decrease in the LCST of the resulting terpolymer. In contrast to what we have obtained with DMA-AZAA copolymers, we observe a sharp transition from clear to turbid solutions, occurring over a narrow range of temperature, suggesting a much narrower polydispersity of the chains using ARGET-ATRP. These results encouraged us

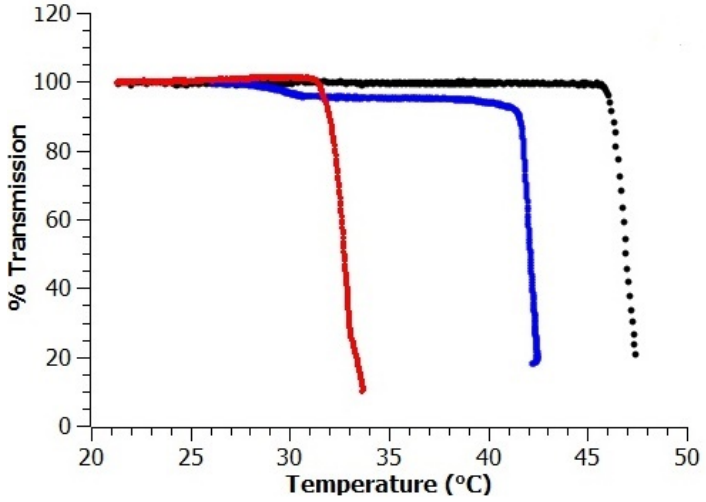

Figure 5.20: Turbidity measurements for different terpolymers terp3 (black curve), terp4 (blue curves) and terp5 (red curves) with varying DMA:NIPAM molar content.

to further tune the LCST so as to achieve the target temperature.

Effect of AZAAm content on LCST

Next, we have studied the effect of varying the azobenzene content on the resulting LCST. This was done by varying the AZAAm molar ratios in the polymerization feed, keeping the molar ratio of NIPAM and DMA fixed. Doing so, we observe (in figure 5.21) that sharp transitions in temperature are obtained. The LCSTs for the terpolymers Terp1 (red curves), Terp2 (green curves), and Terp3 (black curves) are seen to increase with a decrease in the overall hydrophobicity of the azo-content, as expected.

Furthermore, as reported in Table 5.2, solutions of Terp3 are seen to display, among the set of designed terpolymers, the largest difference in LCST under UV/Visible illumination. We observe that changing the azo content in the final polymer induces an effect on the magnitude of the LCST variation, leading us to the fact that phase separation in the copolymer depends on the amount of the chromophore species. These results are consistent with the previous findings of Irie [12].

Optimizing the terpolymer composition

With the above findings in hand, we have made a last attempt of varying the overall composition of the terpolymer system. The molar content of all the three monomers was varied minutely, keeping the azo contents close to 1% in the polymerization feed because we observed maximum LCST shift close to these azo percentages. By optimizing the incorporated amounts from terp6 to terp8 (figure 5.22(a)), the approach leads us to a terpolymer that exhibits LCST values of almost 37°C in its dark-adapted state (red curve).

In addition to this, the polymer solution exhibits a highly efficient photoswitching (figure 4.22(b)). A completely phase separated solution, under UV irradiation is seen to completely solubilize into a clear solution which can then be reversibly phase separated

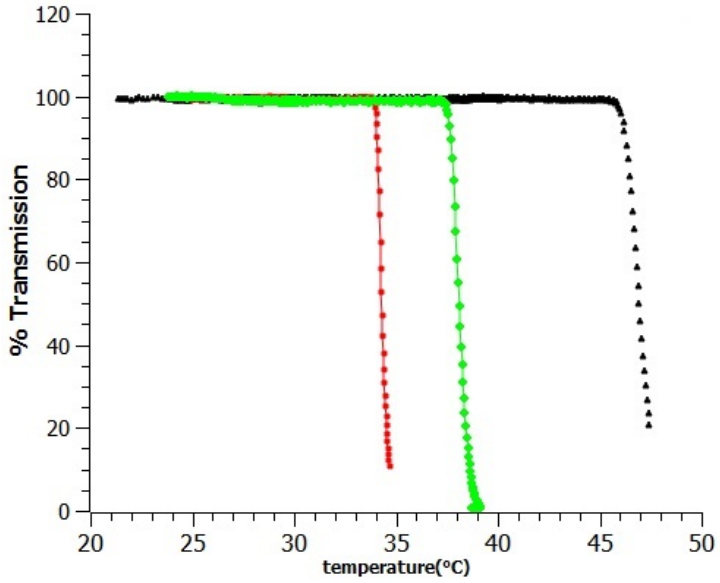

Figure 5.21: Turbidity measurements for different for different terpolymers terp1 (red curve), terp2 (green curves) and terp3 (black curves) having decreasing molar content of AZAAm.

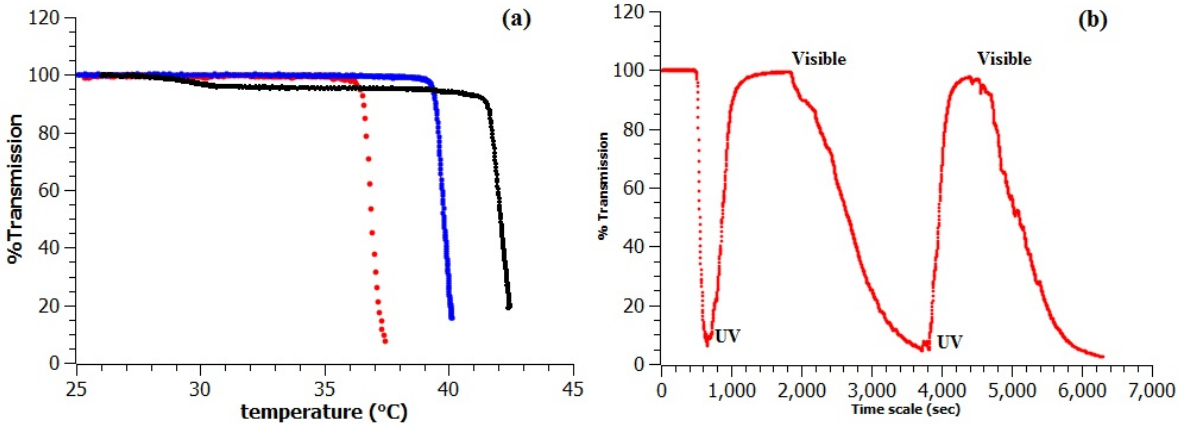

Figure 5.22: (a) variation of LCST for different polymeric compositions: 42°C for terp4 (black curve), 39.1°C for terp6 (blue curves) and 36.9°C for terp8 (red curves). (b) The isothermal photoswitching seen for the case of terp8 ($T = 37.5$°C).

under visible irradiation. These solubility changes take place spontaneously over repeated UV/Visible cycles showing an efficient isothermal photoswitching at 37°.

At this stage, we have obtained a terpolymer that has a sharp LCST at the desired temperature and tuneable properties under light irradiation. With successful attempts at synthesizing the terpolymer, we proceeded with monitoring the polymerization growth of the designed terpolymers.

Polymerization growth

We first checked the polymerization kinetics of a Terp6 polymer solution. A fixed aliquot of polymer solution, at regular intervals, was precipitated in a suitable solvent. From each precipitated mass of polymer, we calculated the monomer to polymer conversion percentage and monitored it along the polymerization duration, as shown in figure 5.23. We observe that a large percentage of monomers get polymerized within the first 15 minutes of the reaction, with marginal increase over longer times. This indicates that, although we have achieved, with this ARGET-ATRP protocol, a good control over the molar content of the polymers, our procedure still does not allows for proper "living" polymerization.

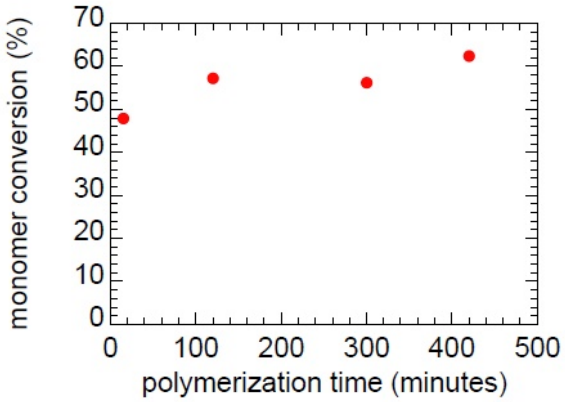

Figure 5.23: Monomer conversion as a function of polymerization time.

The poor living character seen under ARGET-ATRP of terp6 could possibly be explained by previous observations:

- The polymerization of several acrylamide based polymers including PNIPAM and DMA was studied by Matyjaszewski *et al.* [18] via the ATRP protocol. The low conversion was experimentally demonstrated to arise due to a competitive complexation of copper catalyst with polyacrylamides to form species with lower catalytic activity.

- Zhang *et al* [19] showed that the active Cu(I) complex, responsible for polymerization in ATRP, is highly unstable and undergoes disproportionation in polar solvents to generate reduced Cu(0) and Cu(II) species in the solution, which could induce in our case a rapid exhaustion of the active for of the copper catalyst.

These findings led us to synthesize the terpolymer using an altenative approach.

DMA-NIPAM-AZAAm terpolymer synthesis : an alternative approach

In an attempt to improve the control over polymerization kinetics, we have performed a terpolymer synthesis having the optimized composition of DMA:NIPAM:AZAAm (37:63:1.2).

The design strategy involved preparing separately, a catalyst solution and a solution containing the monomers. The catalyst solution was injected into the monomer solution via automated injections with a constant infusion rate of around $100\mu L$ per hour.

Although an extensive study regarding polymer synthesis and characterization was not performed, it is worth showing the interesting results that we obtain with the current synthetic procedure. Absorption studies performed on the terpolymer exhibited an efficient isomerization, and a molar contents around 1.29% that almost matched with the chromophore feed ratio.

As performed previously, the polymerization growth is monitored in terms of the monomer to polymer percentage over the course of the reaction. As shown in figure 5.24, the percentage of monomers getting polymerized increases steadily over time, thereby indicating a proper control of polymerization. These results, though at their early stage without any concrete characterization support, suggest a living/controlled polymerization under the present conditions.

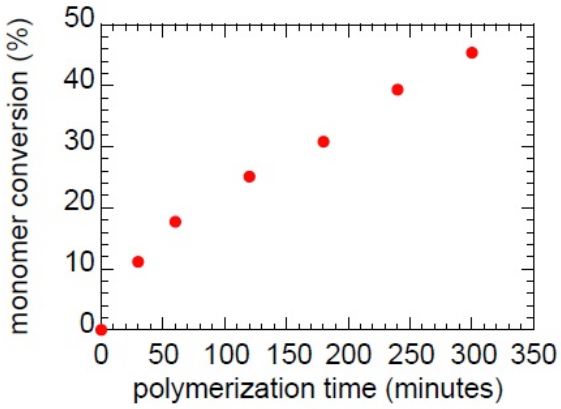

Figure 5.24: Schematic showing the rate of polymerization growth in terms of the conversion ratios over the course of time

Dually responsive properties

In order to verify the dually responsive nature of the terpolymer, we have studied the effect of light exposure on the LCST. The terpolymer solution (conc. 3g/L) is exposed to alternate UV and Visible irradiation. As shown in figure 5.25(a), it exhibits well separated LCST under light induced isomerization, having values in close agreement with those observed for terp8, which has the same monomer composition. In dark, the polymer phase separates at temperatures very close to 37°C. An LCST shift of around 4°C is recorded for a UV-irradiated solution, with the LCST switching back to its initial values under blue light irradiation. The solubility of the polymer solution is seen to be reversibly changed under the UV/blue exposure at $T = 37$°C (figure 5.25(b)). The above results show that the polymer, designed via an alternative strategy, still demonstrates tuneable properties close to physiological temperatures.

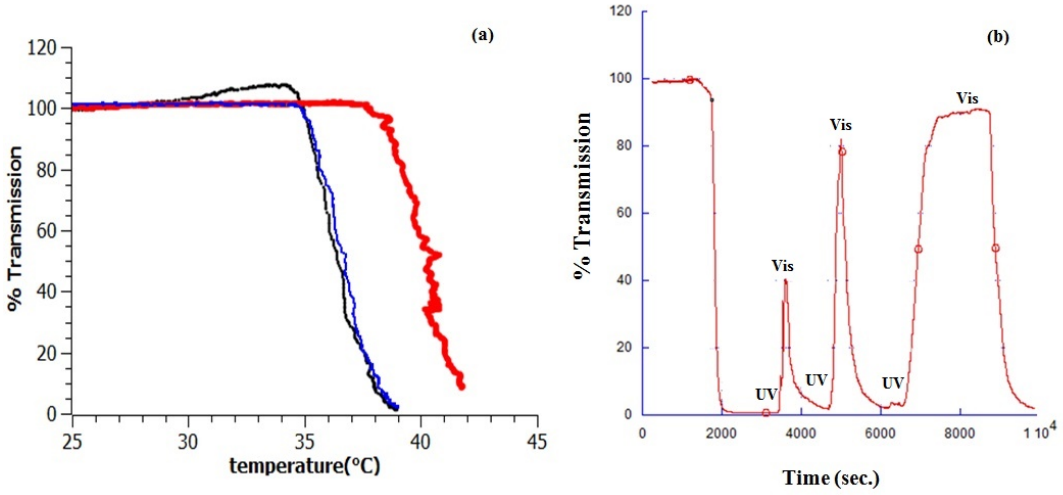

Figure 5.25: (a) the variation of LCST under different light irradiations: (black curve) dark-adapted, (red curve) UV irradiated, (blue curve) blue-irradiated. (b) the effect of photoswitching at constant temperature: three successive UV/Vis cycles have been done, with increasing UV exposure time.

Finally, we have investigated the effect of varying the polymer concentration on the phase behaviour of the terpolymer. It can be seen on figure 5.26(a) that the transitions in transmission curves are shifted to higher temperatures as the amount of polymer in the solution decreases. The LCST of the terpolymer solution therefore decreases at higher concentrations of polymer, as shown on figure 5.26(b). These results, obtained over a range of polymer mass fraction of 0.01-1 %, provide a first hint regarding the bulk phase diagram of this new terpolymer in water. As discussed in the previous chapter concerning PNIPAM, such a phase diagram, which remains to be completed, may be useful for understanding the conformation changes occurring in brushes of such a terpolymer.

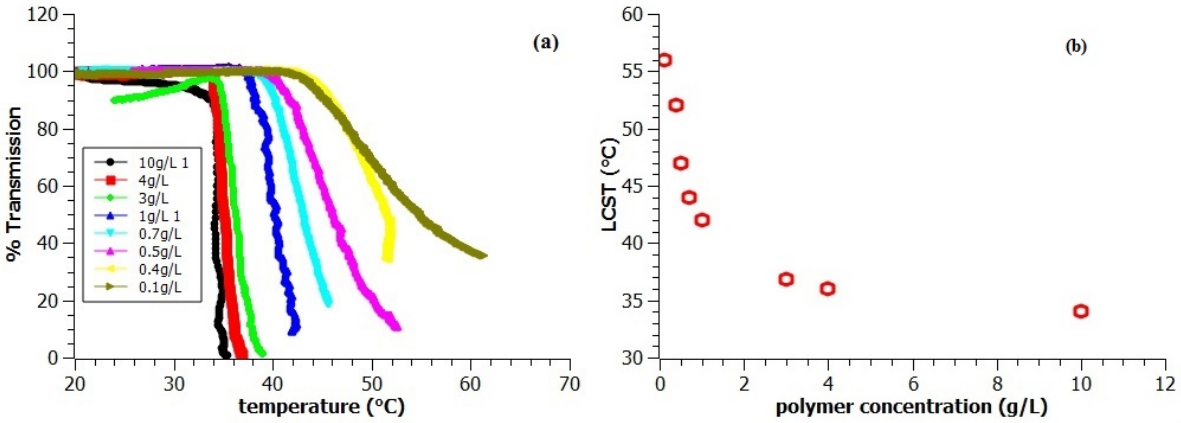

Figure 5.26: (a) transmission curves of terpolymer solutions of different concentrations. (b) decrease in the LCST upon increasing the polymer concentration.

In contrast to the monotonous decrease observed for the LCST as the polymer concentration is increased, we observe that the magnitude of the photo-induced shift of the LCST goes through a maximum in the range1-3 g/L. This is illustrated on figure 5.27.

While we do not have a clear explanation for such a non-trivial effect, we believe that it may result, as proposed by Liu *et al* [16] and briefly mentioned above, from a subtle interplay between intra- and inter-chain aggregation mediated by the AZAAm moieties. If such aggregation effects actually control the observed bell-shaped dependence of the LCST shift, this will require further characterization of the polymer solutions using *e.g.* dynamic light scattering in order to probe the size of such objects.

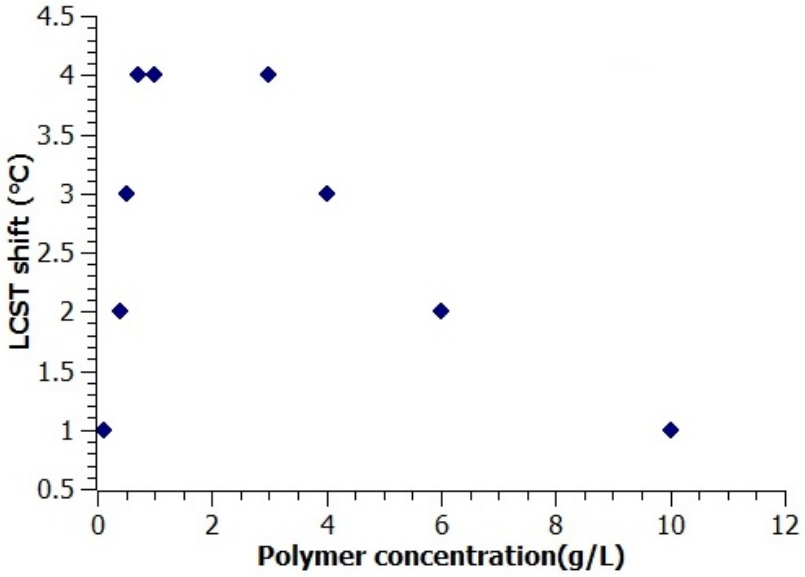

Figure 5.27: Variation with polymer concentration of the photo-induced shift of the LCST.

5.5 Conclusion

We have synthesized two different classes of azobenzene based dually responsive polymers, which were characterized by turbidimetry and UV/Vis spectroscopy.

DMA-co-AZAA copolymers were synthesized via free radical polymerization technique. Some of these copolymers exhibited a LCST that could reversibly be shifted under light irradiations. The UV/Visible spectral studies showed large discrepancies between estimated and theoretical azobenzene contents. The copolymers present non-conventional LCST variations as a function of the chromophore contents, broad phase transitions, and poor reproducibility of the photo-induced effects, which suggested poor control of the polymerization.

As an alternative to the above, we have reported the synthesis of a novel DMA-NIPAM-AZAAm based terpolymer via the ARGET-ATRP protocol. We have optimized the overall polymer composition to design a terpolymer that shows a sharp LCST close to 37°C and an efficient isothermal photoswitching, which is highly encouraging in the perspective of designing photoresponsive brushes for cell biology.

Using a modified polymerization route, we have improved the living character of the polymerization of these acrylamide based polymers by ATRP. We have reported preliminary results regarding the controlled synthesis of P(DMA-NIPAM-AZAA), and presented initial turbidimetry results in good agreement with those obtained with polymers elaborated via ARGET-ATRP protocol. An extensive study based on the current synthesis protocol is now required to better characterize the polymer properties.

Bibliography

[1] Martin A Cole, Nicolas H Voelcker, Helmut Thissen, and Hans J Griesser, "Stimuli-responsive interfaces and systems for the control of protein–surface and cell–surface interactions", *Biomaterials* **30**(9), pp. 1827–1850 (2009).

[2] Sheng Dai, Palaniswamy Ravi, and Kam Chiu Tam, "Thermo-and photo-responsive polymeric systems", *Soft Matter* **5**(13), pp. 2513–2533 (2009).

[3] Yue Zhao and Tomiki Ikeda, *Smart light-responsive materials: azobenzene-containing polymers and liquid crystals*, Wiley (2009).

[4] Olivier Boissiere, Dehui Han, Luc Tremblay, and Yue Zhao, "Flower micelles of poly (n-isopropylacrylamide) with azobenzene moieties regularly inserted into the main chain", *Soft Matter* **7**(19), pp. 9410–9415 (2011).

[5] Yue Zhao and Jie He, "Azobenzene-containing block copolymers: the interplay of light and morphology enables new functions", *Soft Matter* **5**(14), pp. 2686–2693 (2009).

[6] G Sudesh Kumar, *Azo Functional Polymers: Functional Group Approach in Macromolec*, CRC Press (1992).

[7] Happer D.A.R. and J. Vaughan, *The chemistry of hydroazo, azo and azoxy compounds*, J Wiley and sons (1975).

[8] H. Rau, *Photochromism*, Elsevier (1990).

[9] E Sawicki, "Physical properties of the aminoazobenzene dyes.", *The Journal of Organic Chemistry* **22**(8), pp. 915–919 (1957).

[10] Lloyd D Taylor and Leon D Cerankowski, "Preparation of films exhibiting a balanced temperature dependence to permeation by aqueous solutionsa study of lower consolute behavior", *Journal of Polymer Science: Polymer Chemistry Edition* **13**(11), pp. 2551–2570 (1975).

[11] Herman Feil, You Han Bae, Jan Feijen, and Sung Wan Kim, "Effect of comonomer hydrophilicity and ionization on the lower critical solution temperature of n-isopropylacrylamide copolymers", *Macromolecules* **26**(10), pp. 2496–2500 (1993).

[12] M. Irie and D. Kungwatchakun, "Stimuli-responsive polymers. photostimulated reversible phase separation of aqueous solutions of poly (n-isopropylacrylamide) with pendant azobenzene groups.", *Proceedings of the Japan Academy, Series B* **68**(8), pp. 127–132 (1992).

[13] Rainer Kröger, Henning Menzel, and Manfred L Hallensleben, "Light controlled solubility change of polymers: Copolymers of N,N-dimethylacrylamide and 4-phenylazophenyl acrylate", *Macromolecular Chemistry and Physics* **195**(7), pp. 2291–2298 (1994).

[14] Tsuyoshi Shimoboji, Edmund Larenas, Tim Fowler, Samarth Kulkarni, Allan S Hoffman, and Patrick S Stayton, "Photoresponsive polymer–enzyme switches", *Proceedings of the National Academy of Sciences* **99**(26), pp. 16592–16596 (2002).

[15] Smeet Deshmukh, Lev Bromberg, Kenneth A Smith, and T Alan Hatton, "Photoresponsive behavior of amphiphilic copolymers of azobenzene and n, n-dimethylacrylamide in aqueous solutions", *Langmuir* **25**(6), pp. 3459–3466 (2009).

[16] Yan-Jun Liu, Agnes Pallier, Jing Sun, Sergii Rudiuk, Damien Baigl, Matthieu Piel, Emmanuelle Marie, and Christophe Tribet, "Non-monotonous variation of the lcst of light-responsive, amphiphilic poly (nipam) derivatives", *Soft Matter* **8**(32), pp. 8446–8455 (2012).

[17] A. Halperin, M. Kröger, and F. M. Winnik, "Poly(N-isopropylacrylamide) phase diagrams: Fifty years of research", *Angew. Chem. Int. Ed.* **54**, pp. 15342–15367 (2015).

[18] Mircea Teodorescu and Krzysztof Matyjaszewski, "Atom transfer radical polymerization of (meth)acrylamides", *Macromolecules* **32**(15), pp. 4826–4831 (1999).

[19] Qiang Zhang, Paul Wilson, Zaidong Li, Ronan McHale, Jamie Godfrey, Athina Anastasaki, Christopher Waldron, and David M Haddleton, "Aqueous copper-mediated living polymerization: exploiting rapid disproportionation of CuBr with Me6TREN", *Journal of the American Chemical Society* **135**(19), pp. 7355–7363 (2013).

Chapter 6

Conclusion and perspectives

The work presented in this manuscript is the start of a long-term project, aiming at designing a new class of cell culture substrates, based on responsive polymer brushes. Such substrates are expected to allow for the manipulation of the adhesive environment of the cells, on-demand, via the application of a proper light stimulus. This highly multi-disciplinary project requires the combination of skills and tools from surface chemistry, polymer physics, optics, and calls for strong interactions with partners from cell biology.

In this context, we have addressed several important experimental aspects over the course of this PhD project:

- We have set up a surface functionalization protocol allowing to design well controlled responsive polymer brushes using the ARGET-ATRP.
- As a direct application of such functional surfaces in the biological context, we have designed a versatile brush patterning method that has been employed for protein and cell patterning at the surface of soft hydrogels. This patterning method is now used as a routine tool in the laboratory.
- We have developed an original optical setup based on RICM that we have used for the characterization of the conformation change in PNIPAM brushes.
- The above study has provided one of rare experimental proof for the vertical phase separation occurring in PNIPAM brushes upon crossing the LCST, and has allowed us to clarify the physical mechanism at the origin of the hysteretic behavior of PNIPAM brushes during temperature cycles.
- We have proposed an analysis of the RICM data that allows us to estimate most of the molecular parameters of polymer brushes obtained by the "grafting-from" technique.
- In a first attempt to design polymers having more advanced functionalities than PNIPAM, we have initiated the synthesis of dually-responsive (photo- and thermo-) polymers based on acrylamides. Our first results have shown that terpolymers incorporating a small fraction of azobenzene-bearing monomer can be reversibly switched, at physiological temperature, between a water soluble and insoluble state upon light irradiation.

At that stage of the project, several perspectives are open.

6.1 Synthesis and characterization of dually responsive terpolymer

At short term, an in-depth study of the designed terpolymers is required. The characterization of the terpolymer, synthesized via the alternative catalyst infusion approach proposed here, needs to be done at varying polymer compositions in order to validate our results and to better optimize the performance of the system. In particular, in order to fully validate the polymerization strategy, the molecular weights and size distributions of the terpolymers should be systematically investigated using size exclusion chromatography techniques that were missing in the laboratory during the course of the present work.

As mentioned at the end of the previous chapter, the full phase diagram of these new dually-responsive polymers should be built, and the subtle intra- and interchain interactions between the Azo moieties should be better characterized using, *e.g.* light scattering techniques.

6.2 Photo-responsive polymer brushes

A further goal of the project is to design brushes using the above terpolymers. Since our surface functionalization protocol and our bulk synthesis route are both based on ARGET-ATRP, we expect that growing terpolymers from surfaces should require only marginal adaptations of the protocol established for polymerization with free initiators.

We expect the dually-responsive brushes to collapse at 37°C. Light irradiation should then bring about a conformational change in the brushes such that a UV exposure would lead to brush swelling, and under blue light, the brushes would again collapse. As presented in chapter 3, a study using RICM would allow monitoring accurately the change in conformation taking place upon UV/blue irradiation, and to determine the lifetime of the photo-excited state once the light stimulus is removed.

If a proof of principle for a light-induced swelling/collapse of the brushes is obtained, an extension of the RICM microscope allowing for structured illumination of the surface should permit to create, at will, patterns of collapsed/swollen regions over the brush.

6.3 Dynamic cell adhesion

At longer term, we aim at exploiting such a reversible swelling/collapse mechanism to study the dynamics of cell adhesion (figure 6.1). As pointed out in the introduction chapter, cell adhesion on a surface grafted with a low density polymer brush depends on its swelling and collapse. Isothermal switching of the photoresponsive brushes could therefore be a new tool in order to study cell adhesion/detachment dynamics, as illustrated on figure 6.1.

Such a dynamics could moreover be probed by monitoring the cells' focal adhesions, *i.e.* the regions of integrin clusters where intimate cell/surface contact occurs. Such focal adhesions can readily be seen by RICM microscopy, as shown on figure 6.1. In this context, the RICM setup that has been developed thus appears as a versatile technique allowing for both *in situ* characterization of the brush conformation and cell imaging.

Finally, a far reaching application of photoresponsive brushes lies in the possibility they open for guiding cells on a surface. As illustrated on figure 6.2, manipulation of the

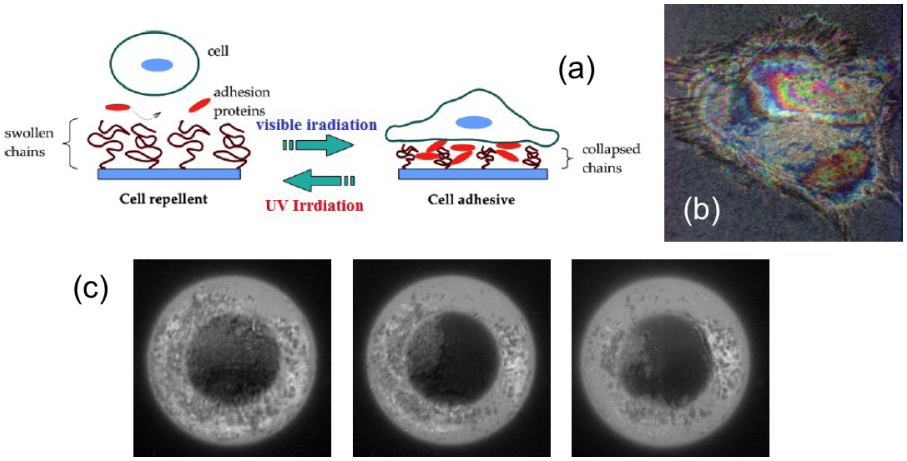

Figure 6.1: (a) Schematic showing the selective detachment of a cell under light irradiation at 37°C. (b) 3-wavelengths RICM image of a fibroblast adhered on a surface: the black elongated regions visible at the cell periphery correspond to focal adhesions, where intimate cell/surface contact takes place. (c) Single-wavelength RICM images of a fibroblast adhered over an annular pattern of a PNIPAM brush: as the temperature is decreased from 37 to 25°C (from left to right), the central brush-covered region swells under the cell and induces repulsive forces provoking cell detachment, which can be observed as the disappearance of focal adhesions in the annular bright region.

adhesive microenvironment of the cells under light irradiation should allow to "move" cells on the surface, change at will the geometrical constraint they experience, and dynamically build model assemblies by bringing multiple cells to contact.

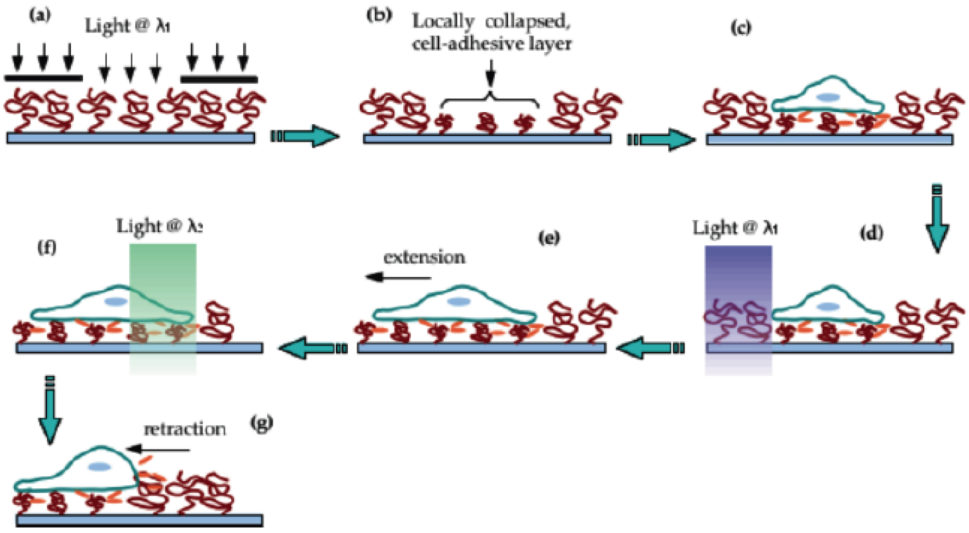

Figure 6.2: Principle of cell adhesion manipulation and guiding using photo-induced swelling/collapse.

Achieving such long-term goals however requires a systematic optimization of the polymer brushes, in terms of the molecular parameters permitting protein adsorption/release upon collapse/swelling, but also in terms of their photo-response, which has to take place at wavelengths which are not toxic to the cells. This will call for a constant shuttle between substrate design, polymer optimization and cell adhesion studies.

Chapter 7

Résumé étendu en français

Les cellules régulent leur organisation interne en fonction de l'évolution de leur environnement extérieur. Cela régit les fonctions biologiques essentielles et est d'une importance majeure pour un grand nombre d'applications. Un objectif fondamental de la biologie cellulaire est de comprendre comment ces comportements complexes sont engendrés par différents signaux environnementaux auxquels la cellule est exposée. Une façon de démêler certains des mécanismes en jeu peut s'effectuer par l'étude de l'adhérence des cellules sur des substrats. Le contrôle et la compréhension des interactions adhésives cellule-substrat est à la fois un défi fondamental et un défi technologique. Des progrès importants ont été réalisés dans la conception de substrats pour la culture cellulaire *in vitro* et l'étude des mécanismes adhésifs. Cependant, les questions relatives à la dynamique et la robustesse des interactions surfaces/cellules restent largement ouvertes.

Le chapitre 1 introduit les phénomènes d'adhésion cellulaire ainsi que les stratégies utilisées pour contrôler et étudier ces adhesions. Les interactions des cellules avec des substrats innovants apportent des réponses aux questions fondamentales concernant l'adhésion. Les substrats "actifs" sont introduits comme des outils potentiels dans ce contexte car ils permettent d'immobiliser des protéines et d'étudier des adsorptions spécifiques des cellules. Les méthodes de mise en forme cellulaire imposent des restrictions à la surface des cellules, créant ainsi un environnement bien défini sur lequel les cellules seront adhérentes. Ceci permet d'étudier la sensibilité et la réponse des cellules à des signaux externes. Les "matériaux intelligents" sont définis pour concevoir des substrats souples qui présentent des propriétés adhésives ajustables qui peuvent être modifiées de manière réversible sur demande. Différents types de matériaux allant des monocouches auto-assemblées (SAM) aux films polymères utilisés pour concevoir des substrats intelligents ont été longuement discutés. La vaste littérature relative à l'utilisation de ces candidats pour des études des bio-interfaces montre un énorme potentiel dans la conception de substrats fonctionnels intelligents pour comprendre les phénomènes associés à la dynamique de l'adhésion cellulaire. Les matériaux utilisés jusqu'à maintenant présentent des limitations en ce qui concerne la réversibilité et le contrôle spatial de l'adhésion cellulaire. Cela soulève une série de questions qui définissent le cadre de cette thèse, en mettant l'accent sur la conception de brosses de polymères permettant un contrôle spatial et temporel de l'attachement de surface pour les études de cellules individuelles.

Le contrôle de l'adhésion cellulaire nécessite une bonne conception de l'architectures des brosses. La conception des brosses de polymères se fait grâce à des protocoles de

synthèse bien contrôlés. Le chapitre 2 présente les brosses de polymères et discute des mécanismes efficaces et pratiques pour l'élaboration de brosses de polymères stimuli-sensibles. Nous discutons l'élaboration de brosses obtenues par polymérisation radicalaire par transfert d'atome initiée en surface, et l'une de ses variantes permettant la régénération in situ du catalyseur de polymérisation, en mettant l'accent sur le PNIPAM (Poly-N-isopropylacrylamide), un polymère therosensible. Des surfaces avec des patterns bien définis à base de PNIPAM sont fabriquées en utilisant une technique nouvelle et polyvalente d'ablation UV. Les substrats patternés de PNIPAM sont utilisés en particulier pour l'élaboration et le transfert de micro-motifs de protéines sur des hydrogels de polyacrylamide, dans la perspective d'études de l'adhésion cellulaire utilisant la microscopie à force de traction (TFM).

La conception de ces brosses stimuli-sensibles fait appel à une détermination précise de leurs propriétés de surface ainsi qu'à la quantification des changements conformationnels associés. Le chapitre 3 décrit un dispositif original implémentant une version spectroscopique de la microscopie en reflexion à contraste interferentiel (RICM). Le RICM est utilisé pour étudier la réponse thermique des brosses PNIPAM sur une gamme de densités de surface σ et de longueurs de chaînes N. Les aspects importants relatifs aux études RICM sont la validation d'outils pour caractériser l'effondrement et le gonflement des brosses de polymères lors d'un changement de qualité du solvant, permettant d'obtenir des informations quantitatives sur les changements des propriétés physiques des brosses de PNIPAM en fonction de la température. L'étude expérimentale s'intéresse à l'influence de paramètres tels que la densité de greffage, et la longueur de la chaîne sur les propriétés de la brosse. Les résultats présentent l'une des très rares preuves expérimentales du phénomène de séparation de phase verticale des brosses PNIPAM. Ils confirment la prédiction théorique de l'existence d'un mécanisme de séparation de phase locale régissant les changements qui ont lieu le long de l'épaisseur de la brosse en fonction de la température. L'étude de la réponse en température de brosses des PNIPAM sur le cycle de chauffage / refroidissement clarifie l'origine physique de leur comportement hystérétique.

Les polymères sensibles à des stimuli sont utilisés en tant que commutateurs moléculaires conçus pour contrôler les interactions entre les objets auxquels ils sont liés. Ces polymères possèdent des propriétés ajustables et présentent un intérêt particulier pour les études des dynamiques d'adhérence cellulaire. Ces études exigent que les polymères soient sensibles à des stimuli qui ne perturbent pas fortement les conditions physiologiques. Dans ce contexte, le chapitre 4 traite de la synthèse en masse et la caractérisation de polymères photo-thermo-réactif par polymérisation radicalaire et ATRP. La composition des entités monomères est modifiée afin de concevoir des polymères qui assurent l'efficacité de commutation conformationnelle à 37 °C, proche de l'environnement physiologique des cellules. Les polymères synthétisés sont caractérisés par turbidimétrie en termes de leur changement de solubilité dans l'eau en fonction de la température et de l'histoire d'irradiation lumineuse à laquelle ils sont exposés. Ils présentent des propriétés accordables proches de la température physiologique de 37 °C, ce qui en font de bons candidats pour une utilisation future dans les applications liées au contrôle spatial et temporel de l'adhésion cellulaire.